The Pennsylvania State University

The Graduate School

Department of Mechanical Engineering

AN ENERGY HARVESTING DEVICE FOR POWERING ROTOR LOAD MONITORING SENSORS

A Thesis in

Mechanical Engineering

by

David Santarelli

Submitted in Partial Fulfillment
of the Requirements
for the Degree of

Master of Science

May 2010

The thesis of David Santarelli was reviewed and approved* by the following:

Christopher D. Rahn
Professor of Mechanical Engineering
Thesis Co-Advisor

Edward C. Smith
Professor of Aerospace Engineering
Thesis Co-Advisor

Stephen C. Conlon
Assistant Professor of Aerospace Engineering
Thesis Co-Advisor

H. Joseph Sommer III
Professor of Mechanical Engineering
Professor-In-Charge of MNE Graduate Programs

Karen A. Thole
Professor of Mechanical Engineering
Head of the Department of Mechanical Engineering

*Signatures are on file in the Graduate School

ABSTRACT

Health and Usage Monitoring Systems (HUMS) on helicopters help to determine when dynamic, flight critical components are replaced. These systems work on the principle of condition based maintenance and attempt to determine the usage of each component through regime recognition. The next step to improving HUMS is to directly monitor the components with on-board sensors that wirelessly communicate with the HUMS. This method would improve accuracy over regime recognition and help reduce maintenance costs and increase safety. Low power electronics, along with the desire to avoid battery replacement, make an energy harvesting solution an attractive option to power any wireless network sensor.

This thesis presents the design of an electromagnetic energy harvester based on Faraday's Law of Magnetic Induction. The design space for the harvester is the hollow rod end of a pitch link on a UH-60 Blackhawk helicopter. All of the relevant design equations relating to electromagnetic energy harvesting are presented and each variable is looked at individually. Three designs for an electromagnetic energy harvester that utilize the rigid motion of the pitch link are analyzed. For each design, an analytical model was made to determine the feasibility of implementing the design. One prototype was fabricated and tested to determine system parameters such as mass, stiffness, damping, and performance parameters such as voltage generated and power delivered to a load.

There is relevant circuit design presented that would be necessary to implement in the final system. The final device is a pendulum system that uses a torsion spring and centrifugal force to realize an effective spring and tune the device to generate power. This design was shown to produce a maximum of 2 mW of power to a resistive load of 1000 ohms at 19 Hz excitation and a base acceleration level of 20 m/s^2.

TABLE OF CONTENTS

LIST OF FIGURES vi

LIST OF TABLES x

NOMENCLATURE xi

ACKNOWLEDGEMENTS xii

Chapter 1 Introduction 1

1.1 Background and Motivation 1
1.2 Vibration Based Energy Harvesting 4
1.2.1 Electromagnetic Implementation 8
1.2.2 Piezoelectric Implementation 12
1.2.3 Electrostatic Implementation 14
1.3 Review of Existing Devices 15
1.4 Objectives and Goals 18

Chapter 2 Design of a New Energy Harvesting Device 21

2.1 Pitch Link Rod End Dynamic Environment 21
2.1.1 Influence of Centrifugal Forces 25
2.1.2 Geometric Constraints 28
2.2 Available Power 28
2.2.1 Effect of Mass on Available Power 29
2.2.2 Effect of Frequency on Available Power 30
2.2.3 Effect of Damping on Available Power 32
2.2.4 Effect of Quality Factor on Available Power 34
2.3 Linear Harvester Design 35
2.4 Centrifugal Pendulum Harvester Design 39
2.5 Reverse Centrifugal Pendulum Harvester Design 44
2.6 Magnet and Coil Design 51

Chapter 3 Experimental Testing of Energy Harvesting Device 55

3.1 Experimental Procedure 55
3.2 Experimental Setup 57
3.3 Fabrication of Harvester Device 61
3.3.1 Torsion Spring 67
3.4 Device Circuitry 71
3.5 Testing of Device 74
3.5.1 Natural Frequency Prediction and Validation 74
3.5.2 Mechanical and Electrical Damping 78
3.5.3 Mass Motion Prediction and Validation 81
3.5.4 Voltage Prediction and Validation 84
3.6 Energy Harvesting Performance 88

Chapter 4 Conclusion....92

4.1 Conclusions on Energy Harvester....92
4.2 Future Work....96

References....97

Appendix A Test Procedure....100

Appendix B Application of Energy Harvester....102

A.1 Rainflow Counting....102
A.2 Fatigue Damage Accumulation....104

LIST OF FIGURES

Figure **1-1**: Predictive versus Condition Based Maintenance. 2

Figure **1-2**: Projected Retirement Time for Condition Based Maintenance 3

Figure **1-3**: Mass-Spring-Damper Representation of Energy Harvester. 5

Figure **1-4**: Change in Magnetic Flux due to a Moving Magnet 9

Figure **1-5**: Electromagnetic Energy Harvester Model. 9

Figure **1-6**: Piezoelectric Material Operating Modes 13

Figure **1-7**: Circuit Representation of a Piezoelectric Element 13

Figure **1-8**: Amirtharajah and Chandrakasan's Linear Electromagnetic Harvester. 16

Figure **1-9**: Beeby et al's Cantilever Beam Configuration 17

Figure **1-10**: MicroStrain's © Piezoelectric Pitch Link Energy Harvester System 18

Figure **1-11**: S-92 Pitch Link Rod End 19

Figure **2-1**: Diagram of Pitch Link and Swash Plate with Vectors. 22

Figure **2-2**: Time History of Vertical Motion of Pitch Link for One Flight Condition 22

Figure **2-3**: Pitch Link Amplitude vs. Cyclic Pitch. 23

Figure **2-4**: Pitch Link Acceleration vs. Cyclic Pitch. 24

Figure **2-5**: Angular Movement of Pitch Link. 24

Figure **2-6**: Pitch Link Location on HUB. 25

Figure **2-7**: Mass versus Centrifugal Force. 26

Figure **2-8**: Centrifugal Forces when Pitch Link is at an Angle. 26

Figure **2-9**: Maximum and Minimum Vertical Centrifugal Forces 27

Figure **2-10**: S-92 Pitch Link Rod End Inside Dimensions 28

Figure **2-11**: Effect of Mass on Available Power. 30

Figure **2-12**: Effect of Frequency on Power.....31

Figure **2-13**: Frequency Ratio versus Available Power. 31

Figure **2-14**: Effect of Damping Ratio on Available Power. 32

Figure **2-15**: Power versus Mechanical and Electrical Damping Ratios.....34

Figure **2-16**: Quality Factor and Frequency Ratio versus Power.....35

Figure **2-17**: Linear Harvester Design. 36

Figure **2-18**: Proof Mass Motion for Linear Harvester.....37

Figure **2-19**: Proof Mass Motion for Linear Harvester for 10^{o} Cyclic Input. 38

Figure **2-20**: Available Power for Linear Harvester. 39

Figure **2-20**: Free Body Diagram of a Centrifugal Pendulum Harvester.....40

Figure **2-21**: Simulink Model for Centrifugal Pendulum Harvester. 41

Figure **2-22**: Proof Mass Motion for Centrifugal Pendulum Harvester. 42

Figure **2-23**: Available Power for Centrifugal Pendulum Harvester. 43

Figure **2-24**: Free Body Diagram of Reverse Centrifugal Pendulum. 43

Figure **2-25**: Natural Frequency of System based on Choice of Torsion Spring. 45

Figure **2-26**: Proof Mass Response When Driven at 1/rev. 47

Figure **2-27**: Proof Mass Response When Driven at 3/rev. 48

Figure **2-28**: Power vs. Torsion Spring Constant.....49

Figure **2-29**: Available Power for Reverse Pendulum at 1/rev. 50

Figure **2-30**: Available Power for Reverse Pendulum at 3/rev. 50

Figure **2-31**: Geometric Representation of Circular Cross section Coil. 51

Figure **3-1**: Flowchart of Experimental Procedure. 56

Figure **3-2**: Shaker and Lever System Test Setup.....57

Figure **3-3**: Tri-axial Accelerometer to Monitor Base Motion System.....58

Figure **3-4**: Oscilloscope Output Monitoring Base Motion System.....59

Figure **3-5**: Overall Test Stand Schematic. 60

Figure **3-6**: Mass-Pulley System to Simulate the Centrifugal Force 60

Figure **3-7**: Hanging Mass Representing Centrifugal Force. 61

Figure **3-8**: CAD Drawing of Reverse Pendulum Harvester. 62

Figure **3-9**: Reverse Pendulum Harvester. 62

Figure **3-10**: CAD Drawing of Linear Reverse Pendulum Harvester. 63

Figure **3-11**: Linear Reverse Pendulum Harvester. 64

Figure **3-12**: Linear Reverse Pendulum Harvester Free Body Diagram. 65

Figure **3-13**: Rotation and Translation of Harvester Devices 66

Figure **3-14**: Torsion Rod Under Loading. 68

Figure **3-15**: Symmetrical Torsion Rod Under Loading. 69

Figure **3-16**: Top View of Harvester Device with Torsion Rod. 70

Figure **3-17**: Bridge Rectifier Schematic. 72

Figure **3-18**: Circuit Schematic used for Design. 72

Figure **3-19**: Effect of Circuit on Generated Voltage. 73

Figure **3-20**: Voltage after passing through a Capacitor. 73

Figure **3-21**: Set-up for Measuring the Motion of the Device. 75

Figure **3-22**: Exponential Decay from Initial Displacement Test. 76

Figure **3-23**: Natural Frequency vs. Centrifugal Force. 77

Figure **3-24**: Simulated Centrifugal Force on Proof Mass. 78

Figure **3-25**: Electrical Damping vs. Load Resistance. 80

Figure **3-26**: Absolute Velocity of Proof Mass Experiment vs. Predicted with No Force 82

Figure **3-27**: Relative Velocity of Proof Mass Experiment vs. Predicted with No Force. 82

Figure **3-28**: Absolute Velocity of Proof Mass Experiment vs. Predicted for 0.47 N of Force. 83

Figure **3-29**: Relative Velocity of Proof Mass Experiment vs. Predicted for 0.47 N of Force. 84

Figure **3-30**: Coil used in Experiment.....85

Figure **3-31**: Magnet Next to Coil vs. Magnet in a Coil. 86

Figure **3-32**: Voltage Generated at 19 Hz. 86

Figure **3-33**: Voltage Generated at 4.3 Hz with no Centrifugal Force.....87

Figure **3-34**: Voltage vs. Frequency Ratio.....88

Figure **3-35**: Power vs. Load Resistance at 20 Hz Excitation.....89

Figure **3-36**: Power vs. Flight Condition at 19 Hz.....90

Figure **4-1**: Voltage Tripler Circuit.....94

Figure **4-2**: Results of Voltage Multiplier Circuit Simulations.....95

Figure **A-1**: Strain Data from Lead-Lag Damper and the Extracted Maxima and Minima. 103

Figure **A-2**: Three Dimensional Histogram of Rainflow Counted Strain Data. 103

Figure **A-3**: Two Dimensional Histogram of Rainflow Counted Strain Data.....104

Figure **A-4**: Individual and Accumulated Damage Hybrid Theory Fatigue Algorithm.....107

Figure **A-5**: Remaining Life from Hybrid Theory Fatigue Algorithm.....107

LIST OF TABLES

Table **2-1**: Forces acting on Centrifugal Pendulum Harvester Proof Mass.....41

Table **2-2**: Forces acting on Reverse Centrifugal Pendulum Harvester Proof Mass.....45

Table **2-3**: Comparison of Magnetic Materials. 52

Table **3-1**: Vertical to Lateral Acceleration dB Ratios.....59

Table **3-2**: Forces Acting on Proof Mass. 65

Table **3-3**: Natural Frequency of Linear Reverse Harvester for Different Values of K.....67

Table **3-4**: Natural Frequency of Reverse Pendulum Harvester for Different Values of K.....68

Table **3-5**: Required Diameter of Wire to achieve Spring Constant for Linear Device.....71

Table **3-6**: Required Diameter of Wire to achieve Spring Constant for Reverse Pendulum. ..71

Table **3-7**: Mechanical Damping Values. 79

Table **3-8**: : Load Resistance as a Function of Centrifugal Force.....80

NOMENCLATURE

A	Acceleration
B	Flux Density, Magnetic Field
c	Damping Coefficient
C	Capacitance
e	Distance from Rotor Shaft to Pitch Link
E	Energy
F	Force
i	Current
k	Spring Stiffness
l	Coil Length
L	Inductance
m	Mass
N	Number of Coil Turns
P	Power
Q	Quality Factor
r	Distance from Rotor Shaft to Harvester Proof Mass
R	Resistance
t	Time
v	Voltage
V	Velocity
x, X	Displacement, Absolute Amplitude of Proof Mass
y, Y	Displacement, Amplitude of Base
z, Z	Displacement, Amplitude of Proof Mass Relative to Base
τ	Period
ω	Frequency
ζ	Damping Ratio

ACKNOWLEDGEMENTS

I would first like to thank Dr. Ed Smith for his enthusiasm and support throughout the duration of this project. Without his help and vision this thesis would have never been realized. I would also like to thank my other advisor in the aerospace department Dr. Steve Conlon for his expertise and help throughout the project and Dr. Chris Rahn for being my advisor in the mechanical engineering department.

I also need to thank Dr. Jacob Loverich and Dr. Jeremy Frank at KCF Technologies for providing me with funding, insight and other forms of help for the past two years. Thank you to Zach Fuhrer and LORD Corporation for providing me with photographs and dimensions of pitch links and Jonas Corl for allowing me to use his computer code written for his thesis and helping me run it. Thank you to Mark Catalano for his help with circuit design and power measurements and thank you to Mike Quintangeli for his help building the base motion stand and the harvesters, along with the staff at the Learning Factory for all of their help with fabrication.

Thank you to my awesome girlfriend, Brianne, for being so patient with me while I finished my work away from her. Finally, I would like to thank my parents for all of their love and support. Without you I would not be the man I am today.

Chapter 1

Introduction

1.1 Background and Motivation

Critical rotorcraft components such as the lead-lag damper, the pitch link, and the rod ends all suffer from fatigue due to constant cycling during flight. Health and Usage Monitoring Systems (HUMS) developed by Goodrich Corporation, Honeywell, and other manufacturers attempt to determine when to retire these components before catastrophic failure occurs. Preventative maintenance philosophy used in the past required components to be removed based on manufacturers testing and static projections. Components were often discarded well before they became unusable or in some cases not until after they failed [1].

A shift to HUMS systems allows for a condition based philosophy where components are monitored and failure is projected based on usage rather than prediction [1]. Regime recognition says that during each flight regime the component accrues a certain amount of damage. Accurate recognition of each regime during flight is essential to determining the total damage seen by the component. Sometimes a pilot is asked to record the details of a flight and then regime recognition is used to determine maintenance [2]. However, automated recording of flight maneuvers alleviates this burden on the pilot and is more accurate. The stated goal of HUMS is to lower maintenance cost while improving operational readiness and safety [2]. The usage monitoring system is applied to those parts which are deemed life limited. The flowchart of Figure 1 below shows the difference between the preventative maintenance philosophy which is solely based on predictions and the condition based philosophy based on monitoring pre-determined failure criteria [1].

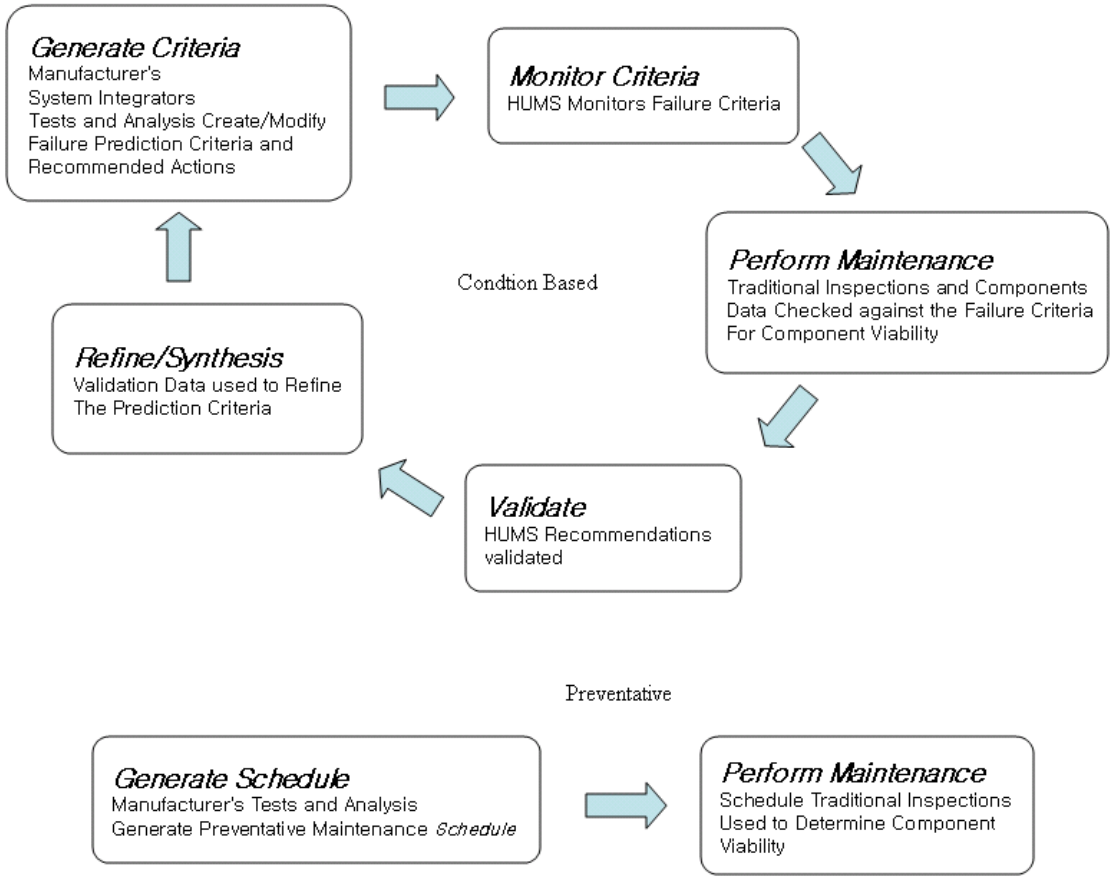

Figure **1-1**: Preventative versus Condition Based Maintenance [1].

Current HUMS systems do a good job of reaching the goal for which they were put in place but there is still room for improvement. The next logical step in improving HUMS is to use direct monitoring by use of a sensor embedded in the component. This would allow the actual usage of the component to be used when determining retirement time instead of regime recognition thus improving the accuracy of such a system. A system like this could constantly produce an updated retirement time. Figure 1-2 on the following page shows how the system might work [3]. The predicted usage sets the design life of the component and the HUMS system, using data from the sensor would be able to change the retirement time if the usage is more or less severe. In order to achieve this goal, sensors put on rotorcraft components would

need to be wireless, light weight, reliable, and powered for the entire life of the component without adding any additional maintenance time.

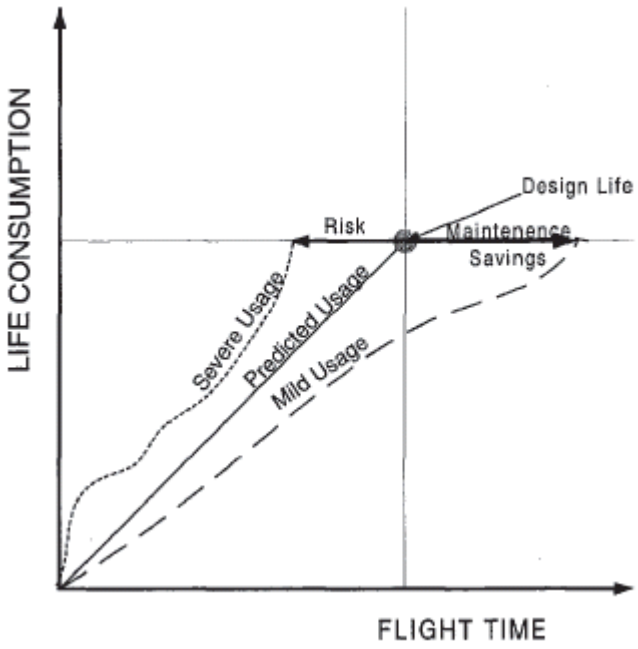

Figure **1-2**: Projected Retirement Time for Condition Based Maintenance [3]. Direct monitoring would allow the design life retirement time to be extended or shortened based on actual usage.

Wireless sensors are already available for monitoring machinery, bridges, and other fatigue limited structures [4]. There are also some sensors already on rotorcraft that monitor the gearbox and other airframe components. However, the source of power for these wireless sensors is often a battery and weight is often not a design issue due to the structures they are used on. Batteries have a finite life and need to be replaced, making them insufficient for use in sensors on rotary wing aircraft because they add unwanted maintenance time. A lightweight device that harvests its own energy would never need to be replaced and can be put in locations where battery powered devices can not.

Energy harvesting has been a major source of research in both the academic world and in commercial industry due to its widespread potential for wireless sensor systems. Advances in

low power consumption wireless technology have increased the demand for autonomous, wireless sensing capabilities. Batteries, for the reasons stated above, are often not desired as the main source of power. Energy harvesting is rapidly becoming the most viable source to obtain the power needed. There are three main ways of converting ambient mechanical energy found in the environment into useful electrical energy. These are [5]:

1) Electromagnetic – power conversion results from the relative motion of an electrical conductor in a magnetic field

2) Piezoelectric – use of piezoelectric materials which produce an electrical charge when mechanically deformed

3) Electrostatic – two conductors separated by a dielectric (i.e. a capacitor). When the conductors move, the energy stored in the capacitor changes, providing the mechanism for conversion.

The equations governing these conversion mechanisms are discussed in detail in the next section.

1.2 Vibration Based Energy Harvesting

Vibration based energy harvesters can be modeled as a mass-spring-damper system like the one shown in Fig 1-3. The system consists of a seismic mass, *m*, a spring with stiffness *k*, and a damper *c*. The extracted energy is represented by a damper whose force is proportional to velocity. The operating principle is that the inertia of the mass causes it to move relative to the frame when the frame experiences acceleration [5,7]. The displacement of the mass is then used to generate energy by causing work to be done against a damping force *f*.

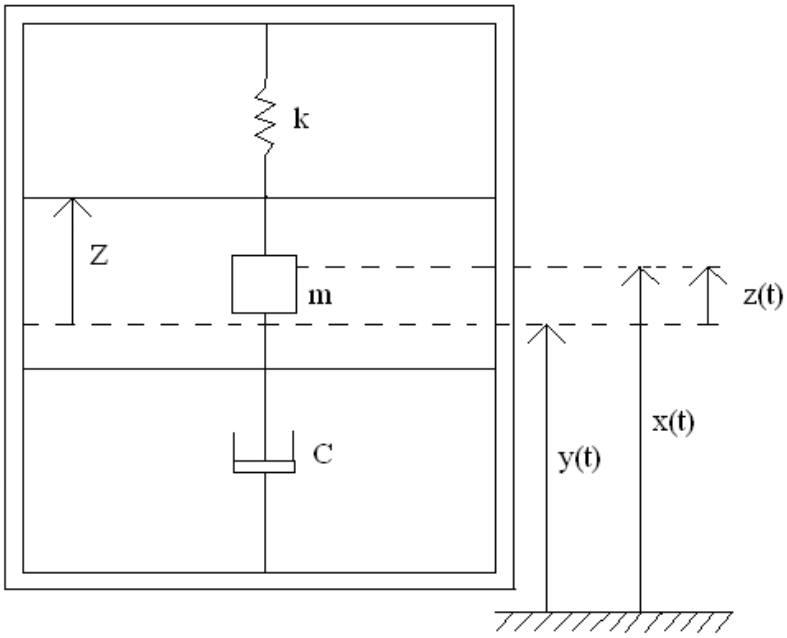

Figure **1-3**: Mass-Spring Damper Representation of Energy Harvester.

In this model, the absolute motion of the frame is given as y(t). This is the input motion to the system and is assumed to be harmonic as $y(t) = Y_0 \cos \omega t$, where Y_0 is the source motion amplitude and ω is the source motion frequency. The displacement of the mass relative to the frame is given as z(t). The absolute motion of the mass is therefore given as $x(t) = y(t) + z(t)$. Z_l is the amplitude of mass-to-frame displacement and will be a limiting factor in generating energy because unconstrained motion of the proof mass is almost never achievable. Z_l/Y_0 is the ratio of proof mass relative amplitude to source motion amplitude and is known as the quality factor, Q.

The differential equation of motion for the proof mass is written as [6]:

$$m\ddot{z}(t) + c\dot{z}(t) + kz(t) = -m\ddot{y}(t). \tag{1.1}$$

To get the transfer function from the frame motion, y(t), to the mass-to-frame motion, z(t), use the Laplace transform to get into the s-domain and rearrange:

$$\frac{Z(s)}{Y(s)} = \frac{-ms^2}{ms^2 + cs + k}. \tag{1.2}$$

Dividing through by the mass, *m*, and substituting in the natural frequency, $\omega_n = \sqrt{k/m}$, and damping, c = $2m\zeta\omega_n$:

$$\frac{Z(s)}{Y(s)} = \frac{-s^2}{s^2 + 2\xi\omega_n s + \omega_n^2}. \tag{1.3}$$

Divide through by ω_n^2 and replace s with jω. Then take the magnitude to get:

$$\frac{Z_0}{Y_0} = \frac{(\omega/\omega_n)^2}{\sqrt{\left(1-\left(\frac{\omega}{\omega_n}\right)^2\right)^2 + \left(2\xi\frac{\omega}{\omega_n}\right)^2}}. \tag{1.4}$$

The energy lost per cycle is the distance integral of the damping force over a full cycle. The force displacement curve encloses an area known as the hysteresis loop that is proportional to the energy lost per cycle [8]. The damping force is proportional to the velocity of the proof mass, so $F_d = c\dot{z}$. Therefore, the energy harvested per cycle is:

$$E_{cycle} = c\int_{-Z_0}^{Z_0} \dot{z}dz. \tag{1.5}$$

The integral of (1.5) becomes:

$$E_{cycle} = c\int_0^{\tau} \dot{z}^2 dt. \tag{1.6}$$

Assuming $z = Z_0 \sin\omega t$, and the period τ = 2π/ω, (1.6) becomes:

$$E_{cycle} = c\omega^2 Z^2 \int_0^{\frac{2\pi}{\omega}} \cos^2(\omega t)\, dt. \tag{1.7}$$

Carrying out the integral of (1.7), $E_{cycle} = \pi c\omega Z^2$. The average power flow is defined is $P_{avg} = E_{cycle}/\tau$ where τ = 2π/ω. This gives $P_{avg} = \omega^2 Z^2 c/2$. The ratio of source frequency, ω, to the natural frequency of the resonant device, ω_n, will be referred to as ω_r. Solving equation 1.4

for Z_0 and substituting it in the expression for P_{avg} gives the expression for the average power dissipated in the damping element.

$$P_{avg} = \frac{Y_0^2 m\omega^3 \xi \omega_r^3}{\left(1-\omega_r^2\right)^2 + \left(2\xi\omega_r\right)^2}. \tag{1.8}$$

If the device can be driven at resonance than $\omega_r = 1$ and the dissipated power becomes:

$$P = \frac{mY^2\omega_n^3}{4\varsigma}. \tag{1.9}$$

As stated earlier the amount of power that can be harvested will be limited by the amplitude the proof mass is allowed to travel. Equations 1.8 and 1.9 assume unconstrained proof mass motion with no limit on Z.

Following the analysis presented by Mitcheson et al. [6], to find the maximum obtainable power it is first necessary to find the optimal required damping factor. This is given by finding the stationary point on dP/dξ:

$$\xi_{opt} = \frac{1}{2\omega_r}\left|\omega_r^2 - 1\right| \tag{1.10}$$

Substituting 1.10 into 1.8 gives the expression for the maximum power that can be converted from mechanical energy into electrical energy:

$$P_{\max} = \frac{\omega_r^2 Y_0^2 \omega^3 m}{4\left|\omega_c^2 - 1\right|}. \tag{1.11}$$

The optimal value for ζ could violate the displacement constraint. Rearranging equation 1.4 for ξ gives the optimal damping factor for the displacement constraint condition:

$$\xi_{opt^{DC}} = \frac{1}{2\omega_r}\sqrt{\omega_r^4\left(\frac{Y_0}{Z_0}\right)^2 - \left(1-\omega_r^2\right)^2}. \tag{1.12}$$

Substituting 1.12 into 1.8 gives the power generated when observing the displacement constraint condition:

$$P_{\max DC} = \frac{Y_0^2 \omega^3 m}{2\omega_r^2}\left(\frac{Z_0}{Y_0}\right)^2 \sqrt{\omega_r^4\left(\frac{Y_0}{Z_0}\right)^2 - \left(1-\omega_r^2\right)^2}\,. \qquad (1.13)$$

The power, then, that can be generated at resonance ($\omega_r = 1$) is:

$$P_{\max DC} = \frac{Y_0^2 \omega^3 m}{2}\frac{Z_0}{Y_0} \qquad (1.14)$$

These equations do not take into account the method by which energy will be extracted from the system. The following sections describe how the three main mechanisms of extraction work starting with electromagnetic implementation.

1.2.1 Electromagnetic Implementation

The damping mechanism used to extract power in an electromagnetic energy harvester will be an interaction between a moving magnet and stationary coil [5]. When the magnet is not moving, its magnetic field creates a flux through the loop. This flux, however, is not changing and therefore no current is induced as shown below in Fig. 1-2a. When the magnet moves into the loop, the flux is increased. An upwards secondary magnetic field is created that opposes the downward magnetic field as shown below in Fig 1-2b. The current in the loop must flow counter-clockwise in order to create the secondary magnetic field.

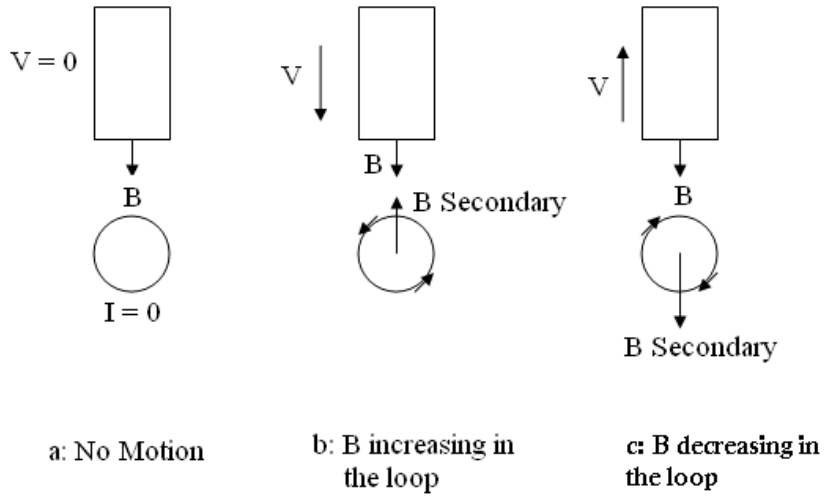

Figure **1-4**: Change in Magnetic Flux due to a Moving Magnet in a Coil.

When the velocity of the magnet is reversed, the secondary magnetic field changes direction to once again oppose the motion of the magnet. This is shown in Fig 1-4c.

A model of an electromagnetic generator, where the damping mechanism for energy extraction is an interaction between the magnet and coil is shown below in figure 1-5 [6].

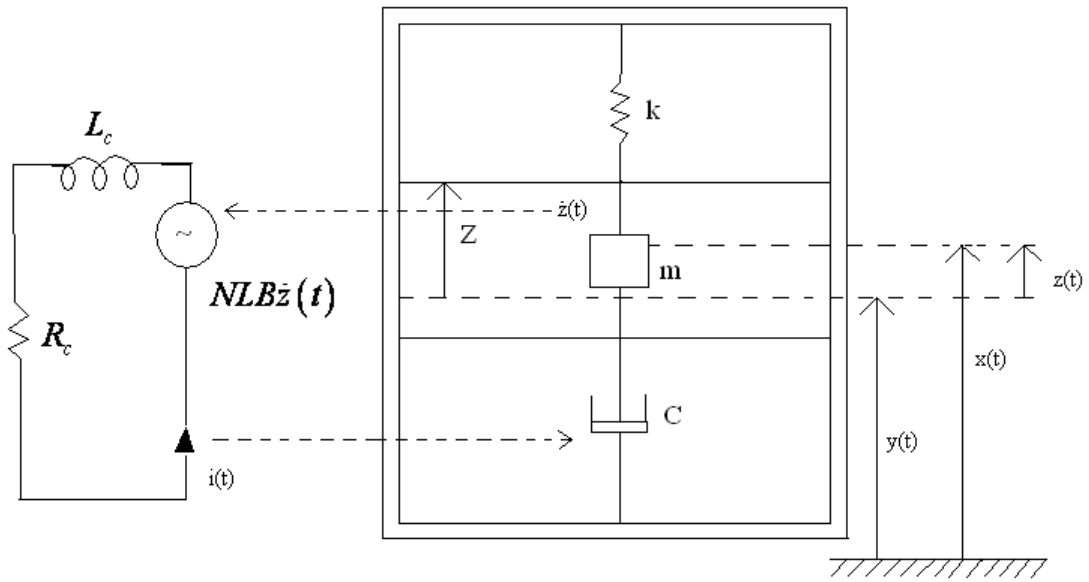

Figure **1-5**: Electromagnetic Energy Harvester Model [6].

The coil-magnet interaction described above is dependant on the properties of the magnet and coil. The moving magnet has a magnetic flux B and the stationary coil has a resistance R_c and inductance L_c. The coil also must be wrapped giving it two more properties; the number of turns N, and the average length of the turn, L. The voltage generated in the coil by a moving magnet with velocity $\dot{z}$ (t) is $v(t) = NLB\dot{z}(t)$. Assuming that the magnet moves sinusoidally with frequency ω and is connected to a resistive load R_L, the current will be $i = v/(R_L + R_C + j\omega L_C)$. The effective damping in Equation 1.1 is then:

$$c = \frac{(NLB)^2}{R_L + R_C + j\omega L_C}. \tag{1.15}$$

The damping ratio is defined as $\varsigma = c/(2m\omega_n)$. This is then the electrical damping portion of the total system damping. The remaining portion is the mechanical damping. Together, $\varsigma_e + \varsigma_m = \varsigma_{total}$. Total system damping will have an effect on the bandwidth of the system. Increasing the damping will reduce the peak power that can be harvested but increases the frequency bandwidth over which power can be harvested. The equation for voltage generated in a coil by a moving magnet assumes that the magnet is moving in the center of the coil. However, if the magnet is not moving in the center of the coil, an efficiency term can be added so that $v(t) = eNLB\dot{z}(t)$, where *e* is a number less than 1 that indicates an efficiency of less than 100%. The *e* term will be looked at more closely in Section 3.5.4.

The damping coefficient, c, from equation 1.15 above can now be used in the harvester equation of motion. Again following the analysis of Mitcheson et al. [6], substituting *c* into Equation 1.1 and taking the Laplace transform gives the transfer function from base motion to proof mass motion:

$$\frac{Z(s)}{Y(s)} = \frac{-s^2 m}{s^2 m + \dfrac{s(NLB)^2}{R_c + R_L + sL} + k}. \tag{1.16}$$

From here on the resistance from the coil and load will be combined into one term, R. Substitute s = jω into equation 1.16 and collect the real and imaginary terms:

$$\frac{Z}{Y} = \frac{m\omega^2 (R + j\omega L)}{\left[mR(\omega_n^2 - \omega^2)\right] + j\omega\left[mL(\omega_n^2 - \omega^2) + (NLB)^2\right]}. \tag{1.17}$$

Taking the magnitude of equation (1.17):

$$\frac{Z_0}{Y_0} = \frac{m\omega^2\sqrt{R^2 + \omega^2 L^2}}{\sqrt{m^2 R^2(\omega_n^2 - \omega^2) + \omega^2\left((NLB)^2 + mL(\omega_n^2 - \omega^2)\right)^2}}. \tag{1.18}$$

The previous quantity is the magnitude and therefore dimensionless. The maximum velocity of the proof mass, z(t), can be found by solving for Z in equation 1.18 and multiplying by the frequency:

$$V_0 = \frac{Ym\omega^3\sqrt{R^2 + \omega^2 L^2}}{\sqrt{m^2 R^2(\omega_n^2 - \omega^2) + \omega^2\left((NLB)^2 + mL(\omega_n^2 - \omega^2)\right)^2}}. \tag{1.19}$$

There can now be an expression for the average power dissipated in R. It is known that the voltage generated is $v = (NLB)\dot{z}(t)$, where $\dot{z}(t)$ is now given by V_0 in equation 1.19. The average power generated is (voltage)^2/(2R) or:

$$P = \frac{\dfrac{m^2\omega^6 Y_0^2 (NLB)^2 R}{2\omega_n^4}}{R^2(1-\omega_r^2)^2 m^2 + \omega^2\left(\left(\dfrac{NLB}{\omega_n}\right)^2 + (1-\omega_r^2)mL\right)^2}. \tag{1.20}$$

The equations described in this section can now be used to design an electromagnetic energy harvester, though more detail is still needed on the coil described in Figure 1-4 and any other

necessary electronics. The second method of mechanical to electrical energy conversion is through the use of a piezoelectric material and is described in the next section

1.2.2 Piezoelectric Implementation

The conversion of mechanical energy to electrical energy can also be done through the use of piezoelectric materials. Piezoelectric materials produce an electrical charge when they are physically deformed, or conversely, physically deform in the presence of an electric field. The two constitutive equations for piezoelectric materials are given by Roundy et al. [5]:

$$\delta = \frac{\sigma}{Y} + dE \tag{1.21}$$

$$D = \varepsilon E + d\sigma \tag{1.22}$$

Where, δ is mechanical strain, σ is mechanical stress, Y is the modulus of elasticity, d is the piezoelectric strain coefficient, E is the electric field, D is the electrical displacement, and ε is the dielectric constant of the piezoelectric material. The most common piezoelectric material currently is polycrystalline ceramic [5].

Piezoelectric materials generally act in two different modes depending on the direction they are stressed. These modes are shown in Figure 1-6. The x, y, z axes are labeled 1, 2, 3 and the two typical modes are the 33 mode and 31 mode. Operating in the 33 mode means that the voltage and stress both act in the 3 direction. The 31 mode means that the voltage acts in the 3 direction but the stress is acting in the 1 direction. The advantages to operating in the 31 mode are that it is much more compliant, meaning larger strains are produced with smaller input forces, and the resonance frequency is lower. The 33 mode, though, has a higher electrical/mechanical coupling.

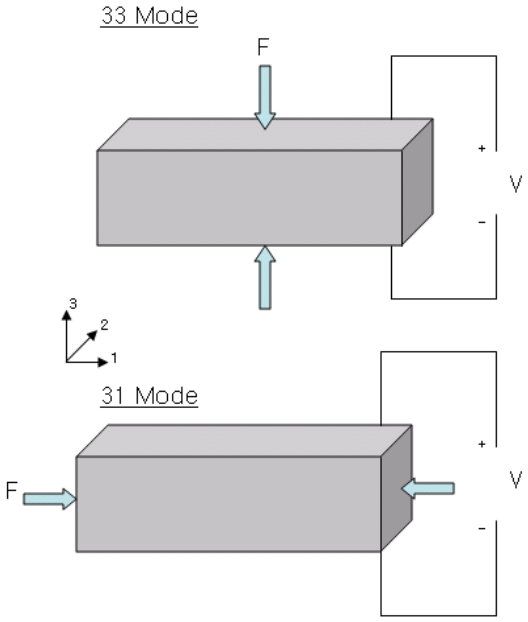

Figure **1-6**: Piezoelectric Material Operating Modes.

Figure 1-7 shows a circuit representation of a piezoelectric element with the source voltage simply defined as the open circuit voltage in equation 1.23. With *t* being the thickness of the material, the expression for the open circuit voltage is:

$$V_{OC} = \frac{-dt}{\varepsilon}\sigma \tag{1.23}$$

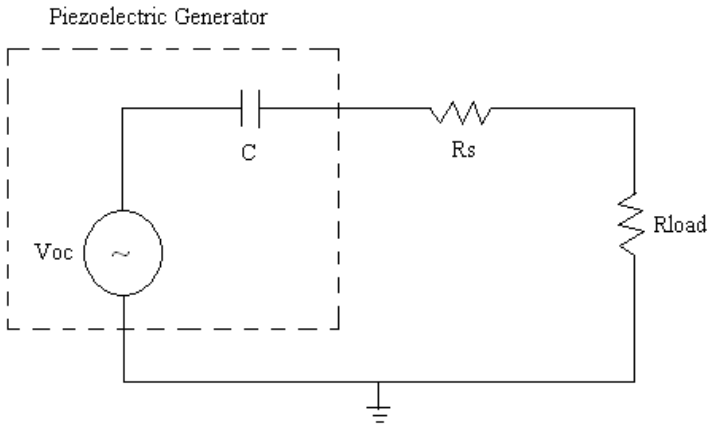

Figure **1-7**: Circuit Representation of a Piezoelectric Element [5].

When the piezoelectric material undergoes a periodic, sinusoidal stress due to source vibrations, an AC voltage will appear across the load. The average power delivered to the load is then simply $P = V_{load}^2 / 2R_{load}$. One of the advantages of a piezoelectric device is the ability to design it to the voltage and current that is appropriate based on the particular electrical load circuit used. A second advantage is that no separate voltage source is needed for the initiation of the conversion process and normally no mechanical stops are needed. This means that the mechanical damping can be minimized.

One disadvantage of piezoelectric devices so far is its ability to be implemented on the micro-scale level. The piezoelectric coupling gets greatly reduced at this level and has trouble being integrated with microelectronics.

1.2.3 Electrostatic Implementation

The third and final energy conversion method is that of electrostatic conversion. This conversion method consists of two conductors separated by a dielectric (i.e. a capacitor), which move relative to one another. As the conductors move, the energy stored in the capacitor changes, providing the mechanism for mechanical to electrical energy conversion. Roundy states that the voltage across the capacitor is [5]:

$$V = \frac{Qd}{\varepsilon_0 lw}. \tag{1.24}$$

This equation assumes a rectangular parallel plate capacitor with length *l* and width *w*. Q is the charge on the capacitor, *d* is the distance between plates and ε_0 is the dielectric constant of free space. Equation 1.24 is the same as V = Q/C, where the capacitance C is given by $C = \varepsilon_0 lw/d$. To increase the voltage then, the capacitance should be decreased assuming the charge is held constant. This can be accomplished by reducing *l* or *w* or increasing *d*. If the voltage is held

constant, then the charge can be increased by reducing *d*, or increasing *l* and *w*. Both methods increase the energy stored on the capacitor. The conversion device is then a capacitive structure which changes its capacitance when driven by vibrations:

$$E = \frac{1}{2}QV = \frac{1}{2}CV^2 = \frac{Q^2}{2C} \tag{1.25}$$

Two advantages of electrostatic converters is their ability to be integrated with microelectronics and their ability to directly generate appropriate voltages. Two disadvantages of electrostatic converter devices is that they require a separate voltage source to initiate energy conversion because of the capacitor, and mechanical stops are needed to ensure that the capacitor electrodes do not come into contact and short the circuit. This also increases the mechanical damping in the device.

1.3 Review of Existing Devices

The objective of this thesis is to develop an electromagnetic energy harvester design that will be used to power a sensor monitoring a dynamic component on a helicopter. Therefore, the review of existing devices has been limited to macro-scale electromagnetic harvesters and those that have been used on rotorcraft.

One of the earliest attempts at creating an electromagnetic harvester was by Amirtharajah and Chandrakasan (1998) [10]. Their generator consisted of a cylindrical housing with a cylindrical mass attached to a fixed spring at one end. A permanent magnet was attached to the bottom of the housing. The mass had a coil attached to it and was free to move vertically within the housing as seen in Figure 1-8. The moving coil cuts the magnetic flux and in this way voltage is generated. The proof mass was 0.5 grams and was attached to a spring with a constant of 174 N/m. It was subjected to a frequency of 94 Hz and produced a peak output voltage of 180 mV.

They predicted that an average of 400μW could be generated from 2 cm of movement at 2 Hz in human powered applications.

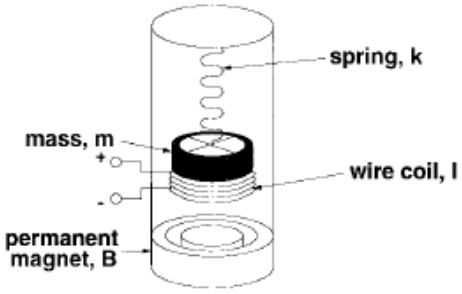

Figure **1-8**: Amirtharajah and Chandrakasan's Linear Electromagnetic Harvester [10].

El-Hami et al. published a paper in 2000 in which they describe a cantilever beam spring based electromagnetic generator [11]. The cantilever beam was clamped at one end and utilized NdFeB magnets at the free end. The coil was fixed in position between the poles of the magnets and consisted of 27 turns of 0.2 mm diameter enameled wire. The total volume of the device was 240 mm^3. It was subjected to a frequency of 322 Hz and amplitude of 25 μm. The reported power generated was 0.53 mW.

Another cantilever beam based prototype was developed by Glynne-Jones et al (2004) [12]. It was also a four magnet, fixed coil arrangement. The total volume of the device was 3.15 cm^3. It was subjected to a frequency of 106 Hz and an acceleration level of 2.6 m/s^2. It produced an output voltage of 1 V. It was then mounted on a car engine and driven for 1.24 Km. The peak power produced was 4 mW, but the average power produced was 157 μW.

Beeby et al. developed their own cantilever beam prototype in 2007 shown in Figure 1-9. The total device volume was 150 mm^3. It was subjected to an acceleration level of 0.59 m/s^2 and had a natural frequency of 52 Hz. It generated 428 mV and 46 μW of power.

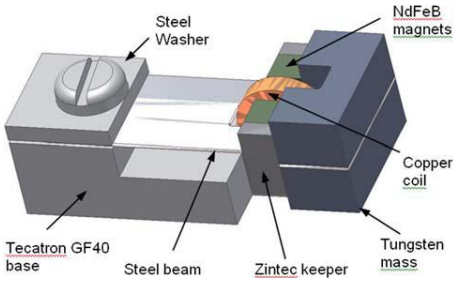

Figure **1-9**: Beeby et al's Cantilever Beam Configuration [12].

Yuan et al (2007) designed a harvester that consisted of an electroplated copper spring released from a substrate onto which an NdFeB magnet is attached with a mass of 192 mg. The spring mass assembly was located within a conventionally wound coil. It experienced and acceleration level of 4.63 m/s^2 and generated 120 μW [17].

Hadas et al developed a harvester as part of a European project concerned with wireless aircraft monitoring. The volume of their device was 45 cm^3 and had a natural frequency of 34.5 Hz. The acceleration level was 3.1 m/s^2 and the reported power generated was 3.5 mW [18].

A human powered generator was developed by von Buren and Troster (2007) [19]. Their design consisted of a tubular translator containing a number of cylindrical magnets separated by spacers. The translator moves vertically within a series of stator coils with the vertical motion being controlled by a parallel spring stage consisting of two parallel beams. The stator and translator designs were realized with six magnets and five coils and had a total volume of 30.4 cm^3. The reported average power output was 35 μW. A good table of existing commercial devices can be found in Priya and Inman's "Energy Harvesting Technologies" [9].

One attempt at harvesting energy from a helicopter pitch link came from MicroStrain's © piezoelectric based harvester [20], [21], [22], [23]. They attempted to place piezoelectric elements along the outside of the pitch link which is subjected to $\pm$ 35 microstrain at 5 Hz. The total weight of the system was about 116 grams. MicroStrain© successfully demonstrated their

system during a flight test of a Bell M412 helicopter where they reported a range of generated power based on the load the pitch link experienced. At around 180 lbs the system generated 220 microwatts. At close to 400 lbs, the system generated about 390 microwatts.

Figure **1-10**: MicroStrain's © Piezoelectric Pitch Link Energy Harvester System Used to Monitor Pitch Link Loads.

1.4 Objectives and Goals

The primary goal of this research is to investigate the feasibility of implementing an electromagnetic energy harvester into the rod end of the pitch link on a helicopter. A Blackhawk UH-60 helicopter was used for the design because the motion of the pitch link was well known. The rod end dimensions were given by LORD Corporation [24]. A picture of an S-92 rod end with dimensions is seen in Figure 1-11. The S-92 and UH-60 helicopters are very similar and share many common components including the rod end. The main goals of the thesis are:

1. Design an electromagnetic resonant energy harvester into a pitch link rod end for the purpose of powering a wireless sensor.
2. Build and a test a device to verify design predictions and energy harvester equations.

Figure **1-11**: S-92 Pitch Link Rod End [24]. The inner cavity of the threaded end is hollow and will serve as the design space.

The objectives required to achieve the primary goal are as follows:

1. Understand the basic design equations and limitations for an electromagnetic energy harvester.
2. Define the design space the harvester will be placed into, including characterizing the base motion it will be subjected to.
3. Design and formulate analytical models for different potential harvester design solutions.
4. Build and test a scale model of a prototype.

The approach used to complete these goals included a comprehensive literature search of previous research on energy harvesting, specifically electromagnetic harvesters and those used on rotorcraft. This allowed all the basic design equations to be established. The design space was chosen through technical discussions with engineers at KCF Technologies who are working on a

similar problem and have talked to experts in the helicopter industry. The pitch link rod end motion was characterized through computer simulations performed at Penn State's Rotorcraft Center.

This thesis outlines the design process for designing an electromagnetic energy harvester into a pitch link rod end with the goal of powering a sensor. A design was chosen and then tested on a system that mimics the motion of the pitch link during different flight conditions. Two different harvesters were tested to characterize performance parameters and to correlate with the analytical models used for design simulations and performance assessments. The two harvesters were based on the same design concept.

Chapter 2

Design of a New Energy Harvesting Device

Designs for an electromagnetic energy harvester in the rod end of a pitch link were explored. The forces acting on the proof mass in the harvester were first examined. The effects of four main parameters related to the available power were then looked at in detail, namely mass, frequency, damping, and quality factor. Three different designs were explored and considered for testing. For all designs, an analytical model was developed to look at the dynamics of the design, and theoretical available power is discussed. Finally, the magnet and electromagnetic coil design and interaction were detailed and discussed.

2.1 Pitch Link Rod End Dynamic Environment

The first step in designing an energy harvester is to accurately characterize the environment it will be expected to operate in. A MATLAB script computer code written at Penn State's Rotorcraft Center was used to describe the motion of the pitch link at a variety of flight conditions [25]. The script calculates the time history of the pitch link during one revolution based on user input of collective and cyclic pitch. Collective and cyclic pitches are two controls that pilots use to control the flight path of the helicopter. The cyclic pitch control changes the pitch of the rotor blades depending on their position as they rotate around the hub so that all blades change their angle by the same amount in the same point in the cycle. The collective pitch changes the pitch angle of all the main rotor blades at the same time independent of their position. A diagram of the pitch link and swash plate is shown below in Figure 2-1. In the diagram C_{PL} is the length of the pitch link, r_p is the vector to the base of the pitch link, r_h is the vector from the

root of the blade along the pitch horn to the pitch link, and r_b is the vector from the center of the swash plate to the root of the blade.

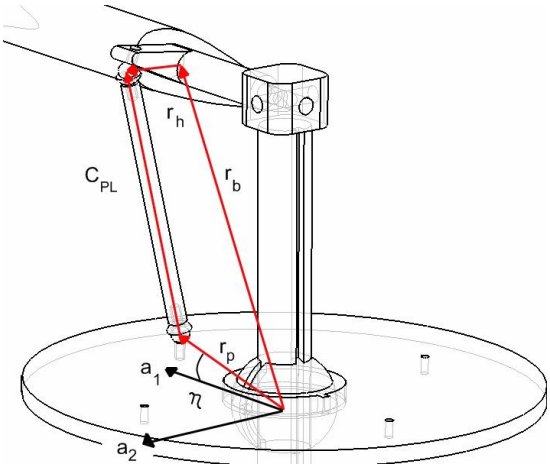

Figure **2-1**: Diagram of Pitch Link and Swash Plate with Vectors [25].

An example output of the analysis is shown below for 5° cyclic and 18° collective. This is the vertical motion of the pitch link in meters for this particular flight condition. The frequency of the motion of the pitch link is 4.3 Hz corresponding to the main rotor rotational speed. This is constant for the duration of the flight.

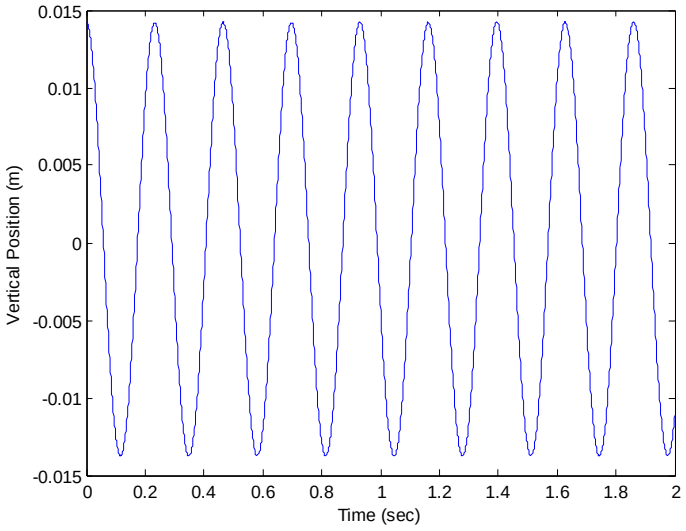

Figure **2-2**: Time History of Vertical Motion of Pitch Link for 5 degree cyclic input.

During any combination of cyclic and collective pitch, the dynamic amplitude of the pitch link motion will largely depend on the value of cyclic pitch rather than collective pitch. A plot of pitch link amplitude versus cyclic pitch at all values of collective pitch illustrates this point.

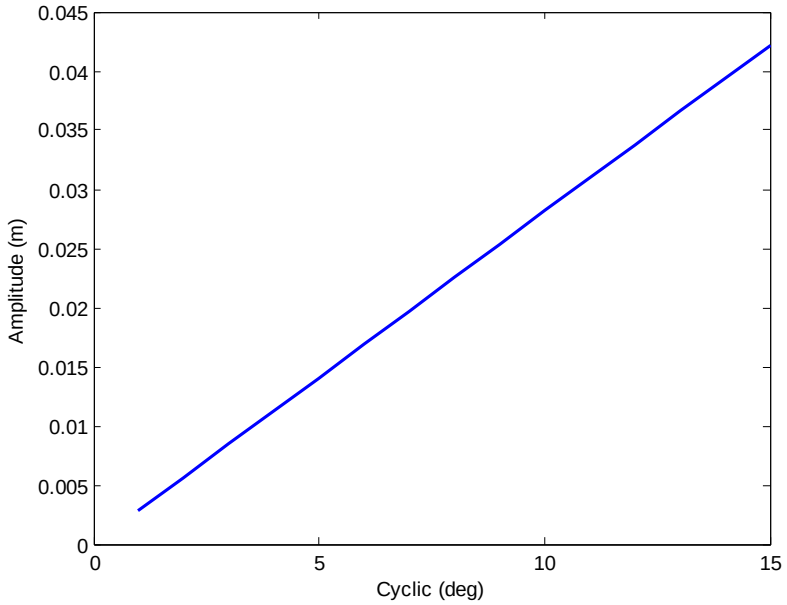

Figure **2-3**: Pitch Link Amplitude vs. Cyclic Pitch. This will be used to design the base motion system to test the harvester

Knowing the pitch link amplitude and frequency is the first step in designing an energy harvester for this application. The results of Figure 2-3 will allow a base motion system to be built that simulates the amplitude and frequency of the pitch link for testing of any device.

The acceleration the pitch link undergoes is now known. This is given by $A = Y\omega^2$. A plot of acceleration versus cyclic pitch at all values of collective pitch is given below. It should be noted that once again, the acceleration the pitch link experiences depends mainly on cyclic pitch rather than collective pitch. The pitch link acceleration values will be useful because the base motion system will be monitored by an accelerometer.

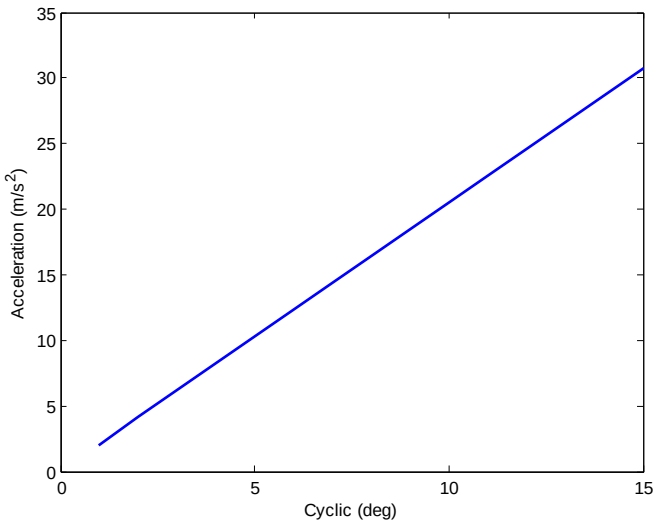

Figure **2-4**: Pitch Link Acceleration vs. Cyclic Pitch. This is another way of looking at the base motion and will be useful when monitoring with an accelerometer

The pitch link, however, does not have purely vertical motion. During one revolution, it also has a small angular component that can be seen from Figure 2-1. This is also dependent on the values of cyclic and collective pitch. Seen below in Figure 2-5 is the angular movement of the pitch link at 5^o cyclic and 18^o collective.

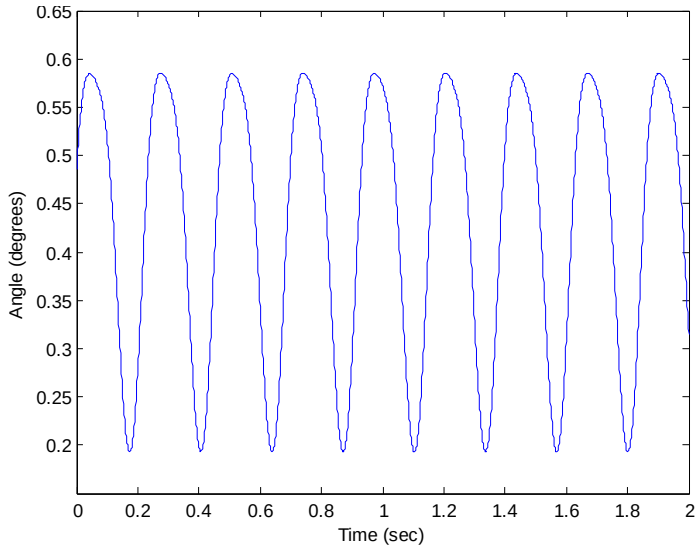

Figure **2-5**: Angular Movement of Pitch Link.

Given a certain device, the angular movement of the pitch link can have an affect on the magnitude and direction of the centrifugal force. This will be looked at in Section 2.1.1. The motion of the pitch link at all values of cyclic and collective pitch are now known and understood. When designing the harvester, it will be very important to know the forces acting on the proof mass in order to design an optimized resonant system.

2.1.1 Influence of Centrifugal Forces

The pitch link is located away from the center of rotation of the shaft that spins the blades as seen in Figure 2-6. Therefore, any mass placed inside the pitch link will experience centrifugal forces proportional to its mass. The centrifugal force is $F = m\omega^2 r$, where m is the mass, ω is the rotational speed, and r is the distance from the center of rotation. The value of r is given as 0.41 meters for a UH-60 helicopter and ω is known to be 27.02 rad/s. A graph of the centrifugal force versus mass is given in Figure 2-7 for masses from 2 grams to 20 grams.

Figure **2-6**: Pitch Link Location on the HUB. r is the distance from the main rotor shaft to the pitch link.

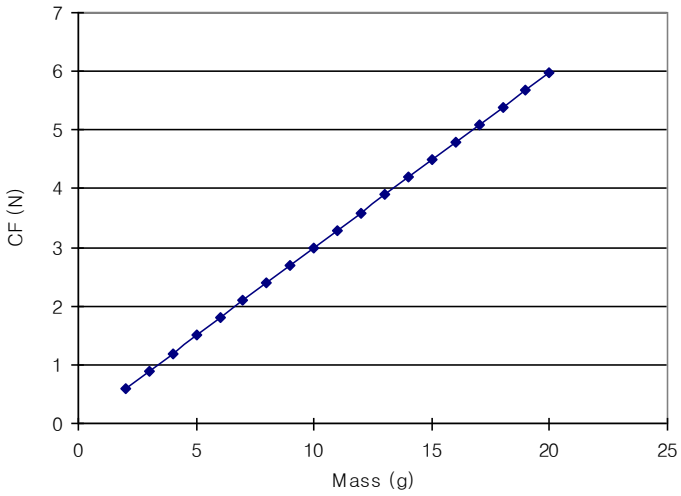

Figure **2-7**: Mass versus Centrifugal Force Showing how CF will Increase with Proof Mass.

If the mass is allowed to stay in-line with the pitch link during the duration of its travel, then it will experience a centrifugal force in both the horizontal and vertical directions when the pitch link is tilted at the angle described in Section 2-1. A diagram of the centrifugal forces in this situation is shown below.

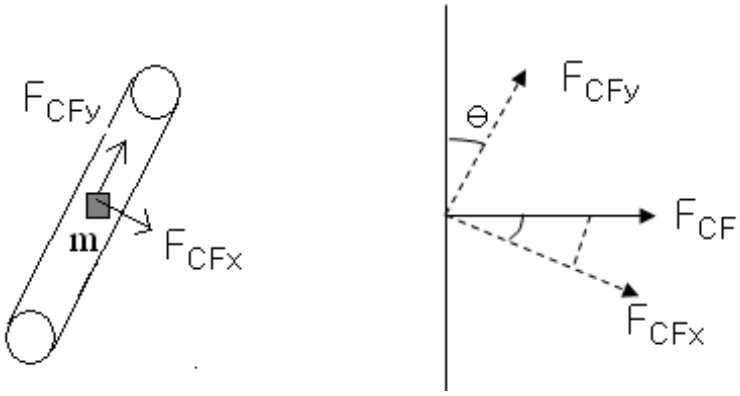

Figure **2-8**: Centrifugal Forces when Pitch Link is at an Angle.

In this situation the force in the vertical direction will be $F_{CFy} = m\omega^2 r \sin\theta$, and the force in the horizontal direction will be $F_{CFx} = m\omega^2 r \cos\theta$. The following graph shows how the vertical centrifugal force will act at 20^o collective and 0^o – 15^o cyclic. As expected, the more extreme flight conditions cause the pitch link to move at greater angles, thus providing greater forces in the vertical direction.

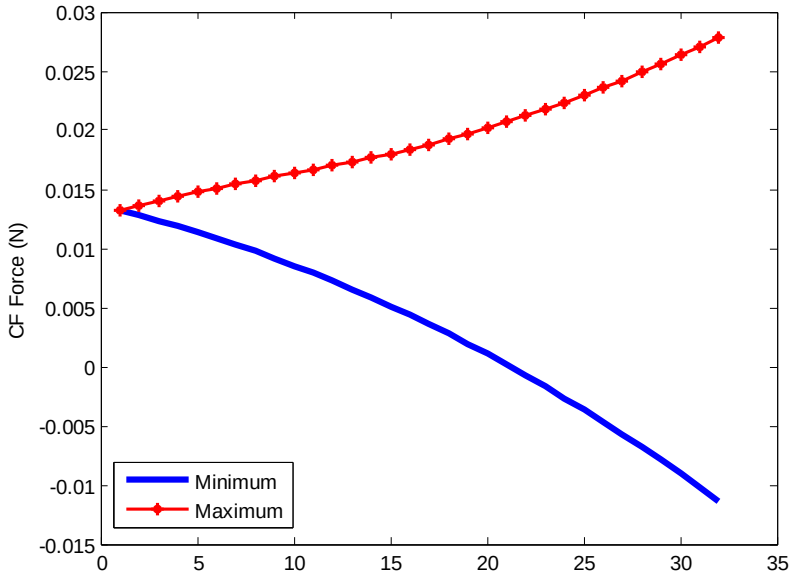

Figure **2-9**: Maximum and Minimum Vertical Centrifugal Forces.

From the graph it can be seen that during a particular flight condition, the vertical centrifugal force has a maximum and a minimum that increases in magnitude for increasing cyclic pitch. This could potentially have an effect on the dynamics of a mass-spring-damper system if a large mass were chosen.

2.1.2 Geometric Constraints

The harvester will be placed in the rod end of the pitch link as stated in Chapter 1. This design space provides the geometric constraints of the device that will limit mass size and motion and coil size. The effects that these will have on the available power will be discussed in the upcoming sections. The rod end that the device will be designed to fit into can be seen in Figure 1-11 of Section 1.4. The inner diameter of the rod end in 0.75 inches (19.05 mm) and its length is 4 inches (101.6 mm) [25]. These dimensions can be seen below in Figure 2-10.

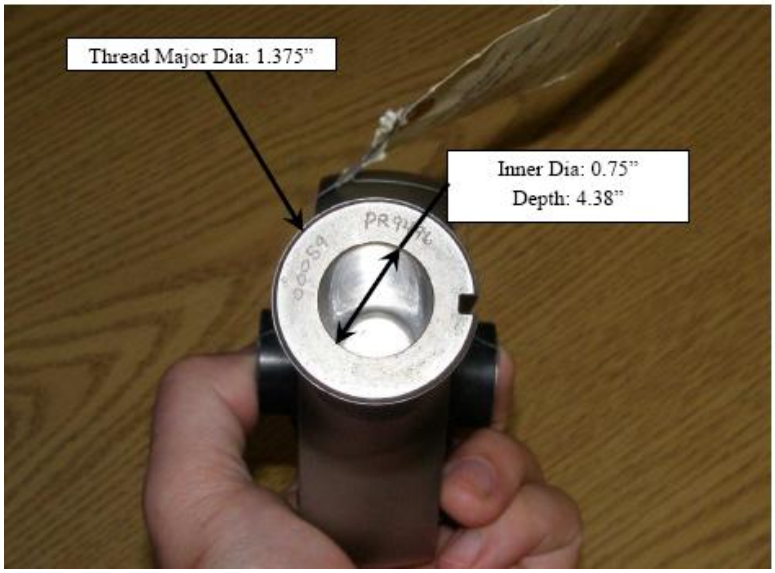

Figure **2-10**: S-92 Pitch Link Rod End Inside Dimensions [25]. The harvester will go inside the cavity shown in the picture.

2.2 Available Power

The equations derived in Chapter 1 can be used to predict the amount of available power the system has. This available power is dependent on four main parameters; mass of the system, frequency of the source, system damping, and quality factor, which refers to the ratio of source

motion amplitude to system motion amplitude. Three of these parameters, mass, damping, and quality factor, can be controlled by the designer within the design space, whereas the third parameter, frequency of the source, cannot be controlled by the designer. The following four sections attempt to better understand the effect these four system parameters will have on the available power for harvesting.

2.2.1 Effect of Mass on Available Power

The available power equation (equation 1.8) from Chapter 1 is restated here and will be referred to as the *average power equation* from here on:

$$P_{avg} = \frac{Y_0^2 m\omega^3 \xi\omega_r^3}{\left(1-\omega_r^2\right)^2 + \left(2\xi\omega_r\right)^2} \tag{1.8}$$

Also from Chapter 1 (equation 1.9), the average power dissipated when the natural frequency of the device matches the natural frequency of the source is the *matched average power*::

$$P = \frac{mY^2\omega^3}{4\varsigma} \tag{1.9}$$

It is obvious here that power will be directly proportional to mass and that the greater mass the system has the more power that will be available. This simple relationship is shown graphically below for different values of mass. It is assumed here that the device natural frequency matches the driving natural frequency so $\omega_r = 1$. The frequency is again taken as 27.02 rad/s. Y_0 will be taken as 0.0141 meters which is a nominal flight condition corresponding to 5^o cyclic, and ζ will be 0.05. The figure illustrates the point that if the frequency can be matched then the amount of energy there is to harvest will increase linearly with increasing mass.

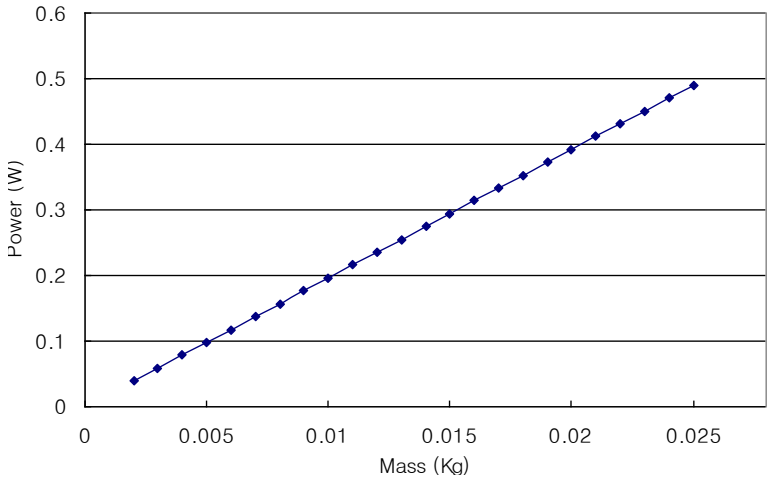

Figure **2-11**: Effect of Mass on Available Power. There is a linear relationship between mass and available power.

The size of the mass will be limited by the design space. Knowing that a neodymium magnet has a density of 7.5 g/cm3, a cylindrical magnet with a diameter of 0.25 inches (mm), and a length of 0.5 inches (mm) will have a mass of 3 grams. For simplicity, a mass of 5 grams will be used in the remaining analysis.

2.2.2 Effect of Frequency on Available Power

The frequency of the source vibrations will be a limiting factor on the amount of available power there is to harvest. The ratio of source vibration frequency to the natural frequency of the harvester is also a factor in the power that can be harvested. Source frequency will be looked at first. If it is assumed that the device operates at the natural frequency of the source, then the matched average power equation says that power is proportional to the cube of the natural frequency as illustrated in Figure 2-12. The mass will be 5 grams, and the input amplitude, Y_0, will be 0.0141 meters. The damping ratio will once again be 0.05.

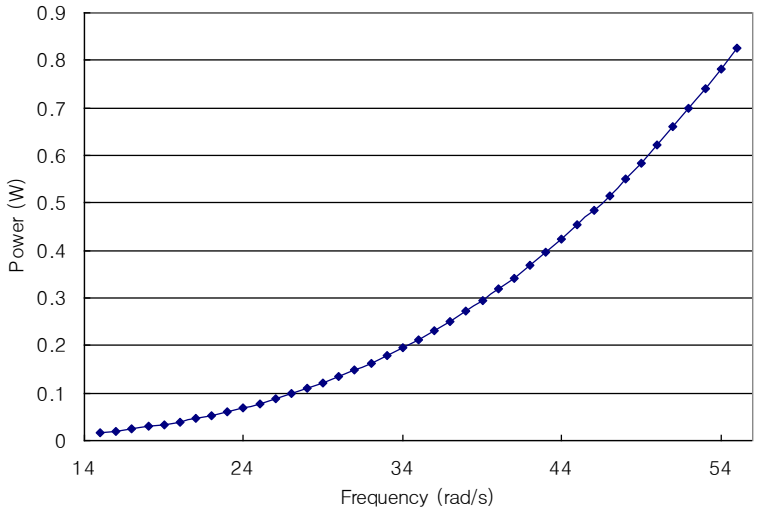

Figure **2-12**: Effect of Frequency on Power Showing the Cubic Relationship.

Often, the harvester cannot be operated at the natural frequency of the source. Even though the device is not operating under ideal conditions, it may still be counted on to harvest power. Using the average power equation that includes the frequency ratio, ω_r, the affect of source frequency to natural frequency of the harvester can be seen.

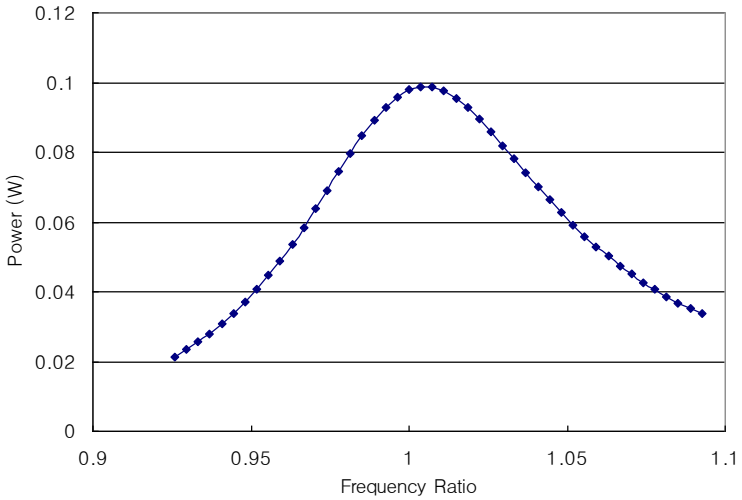

Figure **2-13**: Frequency Ratio versus Available Power. Peak Power occurs when the frequency ratio is equal to 1.

As expected, the peak power is generated when the driving frequency matches the natural frequency of the harvester. At this point, a resonating harvester has the most available kinetic energy to harvest. In the next section, the affect that damping has on the curve of Figure 2-13 will be examined.

2.2.3 Effect of Damping on Available Power

In Chapter 1, the total system damping was defined as $\varsigma_T = \varsigma_m + \varsigma_e$. The mechanical damping will come from pure mechanical losses in the system and the electrical damping will come from the interaction between the magnet and coil and will have an effect on the efficiency of the device to convert mechanical energy into electrical energy. The coil and magnet design will be discussed in detail in section 2.6. The affect that the system damping ratio has on the available power is illustrated in Figure 2-14.

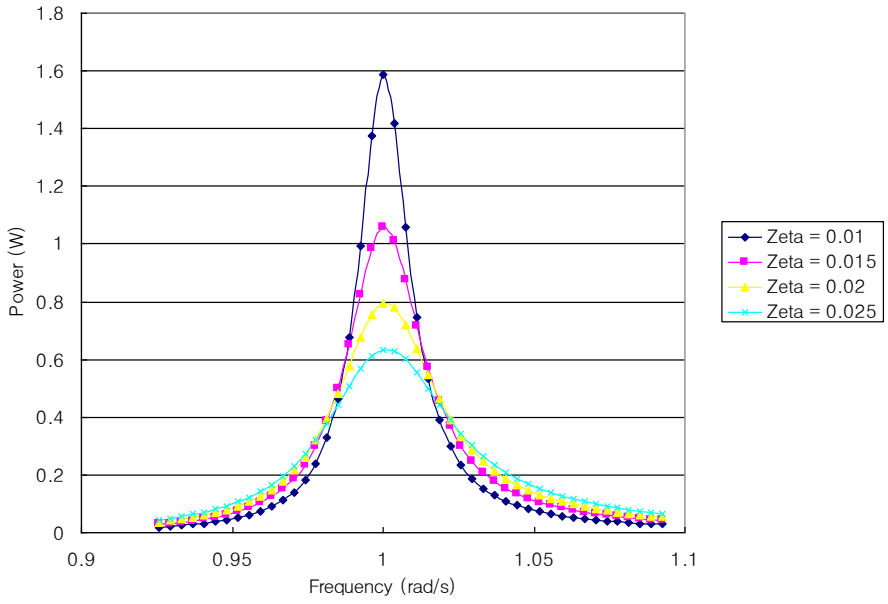

Figure **2-14**: Effect of Damping Ratio on Available Power Shows that Less System Damping Increases the Bandwidth of the Device.

The results of Figure 2-14 assume that the mechanical damping equals the electrical damping. It clearly shows that the damping ratio will have a great effect on the power that is harvested. For less damping, there is more power available but a greater price is paid if the frequency ratio does not equal 1. Conversely, the more damping the system has, the less overall power there is to harvest, but the bandwidth of the system is greater and thus less of a penalty is paid when the frequency ratio is not equal to one. The type of damping however, will also affect how much power is harvested.

Figure 2-15 is a surface plot of power versus mechanical and electrical damping ratios where all values have been plotted as logarithms. The values for mass, amplitude, and frequency used to generate the graph are the same values as in previous graphs. The color bar on the right hand side of the figure symbolizes the total system damping at each point. This graph illustrates the point that the power is maximized when the mechanical damping ratio equals the electrical damping ratio. It also shows that there is a large penalty for when the mechanical damping is much greater than the electrical damping, but only a small penalty for when the electrical damping is greater then the mechanical damping. It can be concluded then, that a lightly damped system will be slightly better then highly damped system, providing the majority of the damping is coming from the electrical portion.

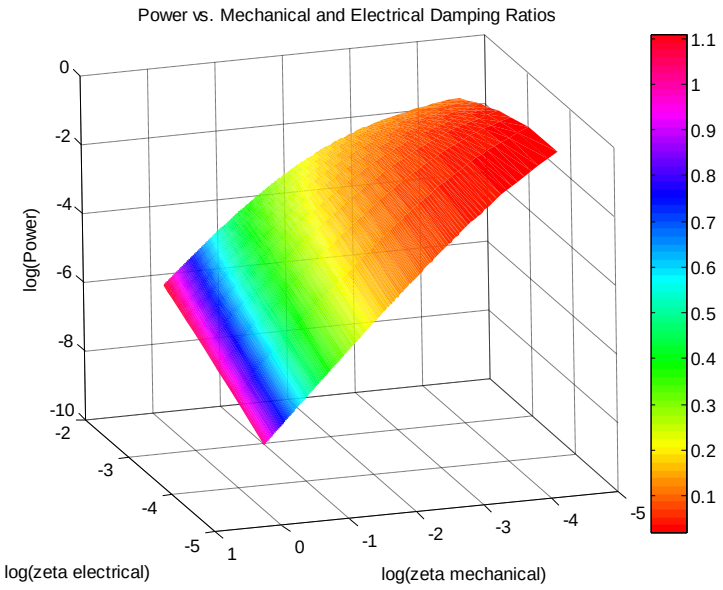

Figure **2-15**: Power versus Mechanical and Electrical Damping Ratios Showing that a High Mechanically Damped System is Less Desirable than a Matched Damped System.

2.2.4 Effect of Quality Factor on Available Power

The ratio of proof mass output motion amplitude, Z_o, to base input motion, Y_o, is known as the quality factor, and is denoted as Q. As stated previously, the device can be displacement constrained, meaning the motion of the proof mass will be limited by the size and dimensions of the overall harvester. From Chapter 1, equation 1.13, the power at the displacement constrained condition is the *constrained power equation*:

$$P_{\max^{DC}} = \frac{Y_0^2 \omega^3 m}{2\omega_r^2}\left(\frac{Z_0}{Y_0}\right)^2 \sqrt{\omega_r^4\left(\frac{Y_0}{Z_0}\right)^2 - \left(1-\omega_r^2\right)^2}\,. \tag{1.13}$$

The optimal damping at the displacement constrained condition is:

$$\xi_{opt^{DC}} = \frac{1}{2\omega_r}\sqrt{\omega_r^4\left(\frac{Y_0}{Z_0}\right)^2 - \left(1-\omega_r^2\right)^2}\,. \tag{1.14}$$

Figure 2-16 is a surface plot of quality factor, (Z_l/Y_0) and frequency ratio versus power. The color bar on the right represents the total system damping at each point.

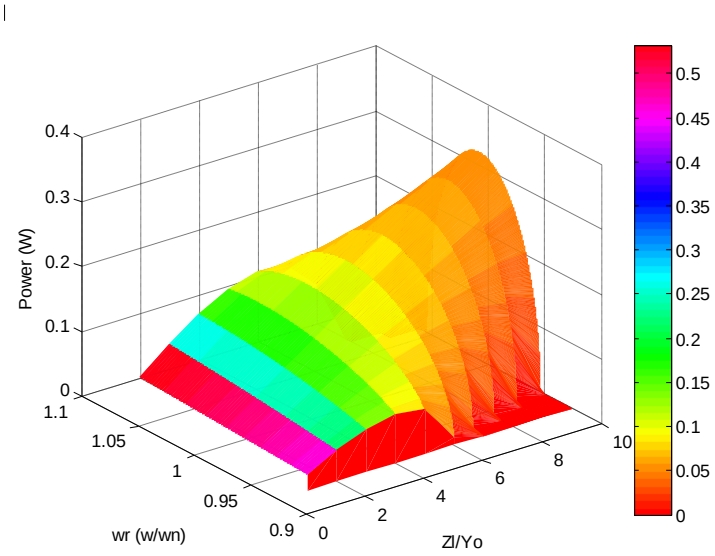

Figure **2-16**: Quality Factor and Frequency Ratio versus Power. This shows that a high quality factor and frequency matching will have the most available power.

As expected, the most power is generated when the frequency ratio is equal to one and the quality factor is at its highest. A quality factor of 10 to 1 may be very difficult to achieve however. Also, the damping has been re-optimized at each point on the graph. This is very difficult to do mechanically, but can be more easily done by adjusting the load electronics [5].

2.3 Linear Harvester Design

The first design is that of a linear harvester. In this design, the magnet acts as the proof mass and is connected to a linear spring. In order to resist the lateral centrifugal force, the mass is on a low friction bearing that will still allow motion in the vertical direction. In this configuration, the coil would have to be placed near the magnet instead of around it. Also, in this design the vertical centrifugal forces will come into play, as the magnet will always be in line

with the pitch link which moves angularly, as well as vertically, as described in Sections 2.1 and 2.11. The biggest challenge in implementing this design, as it will be in all of the designs, is to control the amplitude of the proof mass at all of the different flight conditions and still harvest the required power. Figure 2-17 below offers a very simple schematic of what the device might look like.

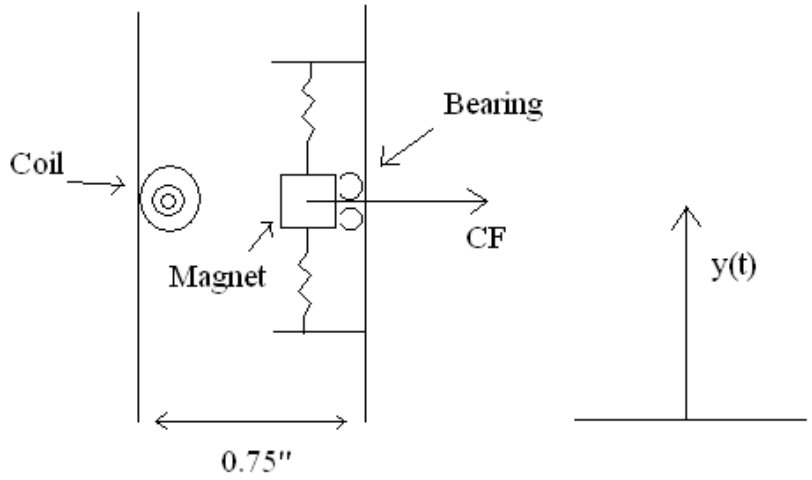

Figure **2-17**: Linear Harvester Design. In this design a magnet is attached to a linear spring vibrating next to a stationary coil.

The equations of motion for this system are the same as for the harvester described in Section 1.2 and for Figure 1-1. The base motion consists of the vertical acceleration from the pitch link and also the time varying vertical centrifugal forces that will accelerate the proof mass. A MATLAB script and a Simulink model have been implemented to simulate the motion of a device like this at all the different flight conditions that it will experience. A plot of the motion of the proof mass when the helicopter is flying at 20^{o} collective and 4^{o} cyclic is seen below in Figure 2-18. The system takes on a dramatically different response with the added effect of the centrifugal forces.

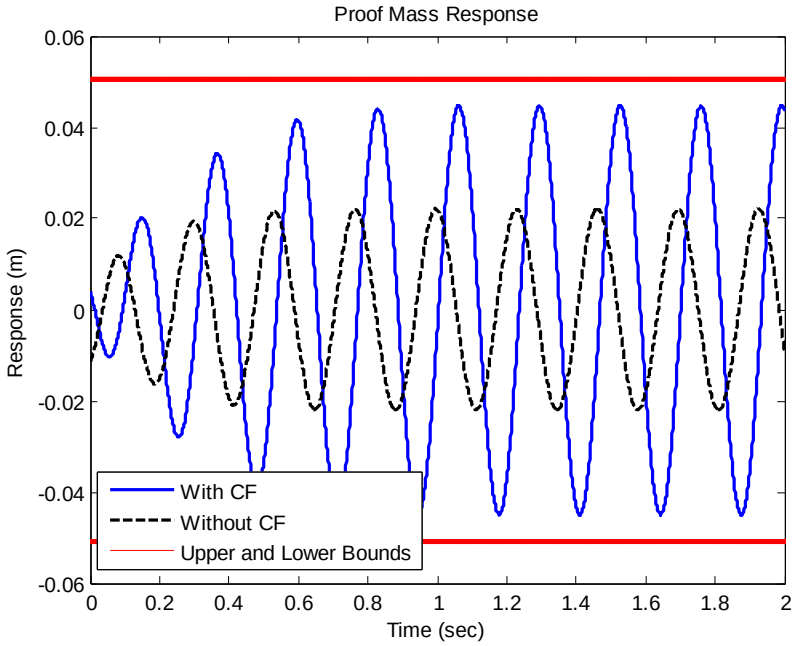

Figure **2-18**: Proof Mass Motion for Linear Harvester for 4^{o} cyclic pitch. The added effect of the centrifugal force causes the system response to change.

Once again the design space is the hollow rod end of the pitch link that measures 3/4 inches (19.05 mm) in diameter by 4 inches (101.6 mm) long. The straight lines on the graph indicate the upper and lower bounds for the proof mass amplitude. In this case the upper and lower bounds have been set at 2 inches (50.8 mm). Realistically, though, the bounds would be smaller to allow for spring compression and electronics. The size of the magnet and coil will also be limited by the design space. A detailed discussion of the magnet and coil design is at the end of this chapter, however, for this analysis a 5 gram mass and a system damping ratio of 0.05 has been chosen to illustrate the relevant points. Figure 2-19 demonstrates that for certain flight conditions, the motion of the proof mass will violate the bounds of the design space and make the analysis incorrect. This is for a 10^{o} cyclic input.

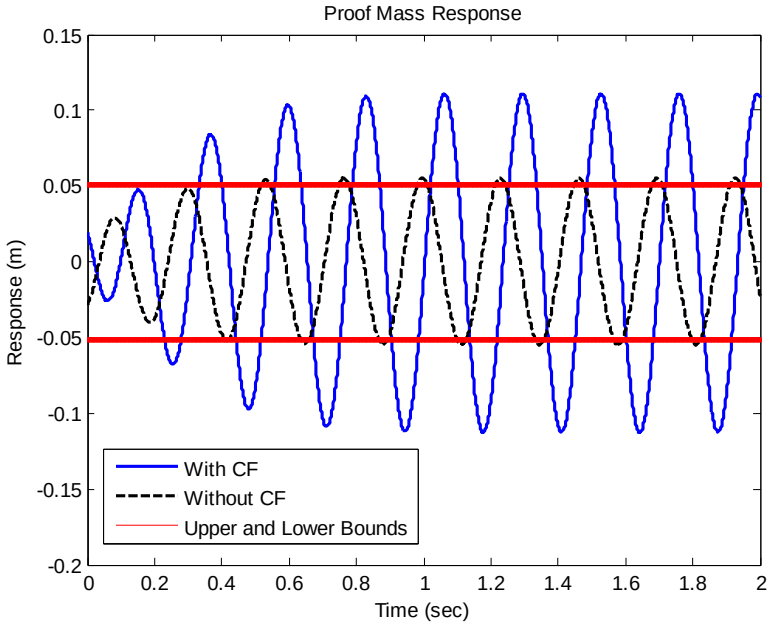

Figure **2-19**: Proof Mass Motion for Linear Harvester for 10^{o} Cyclic Input. The Device will violate the displacement boundaries at this flight condition.

One way to help alleviate the problem of a constrained proof mass motion is to add rubber stops to the system. However, this would require additional space, possibly reducing the quality factor, and change the dynamics of the system. If the amplitude of the proof mass is not contained to the limits on the graph, it is possible to predict the power available. As expected, the available power goes up with flight condition. The available power at all flight conditions is seen in Figure 2-20. This design has 50 mW of available power at a nominal flight condition, which would be more than enough to power a wireless system if it were able to be harvested. However, because of the displacement constraint condition, unconstrained motion of the proof mass is not achievable. Therefore, the amount of available power there is to harvest will be considerably less what is seen in Figure 2-20.

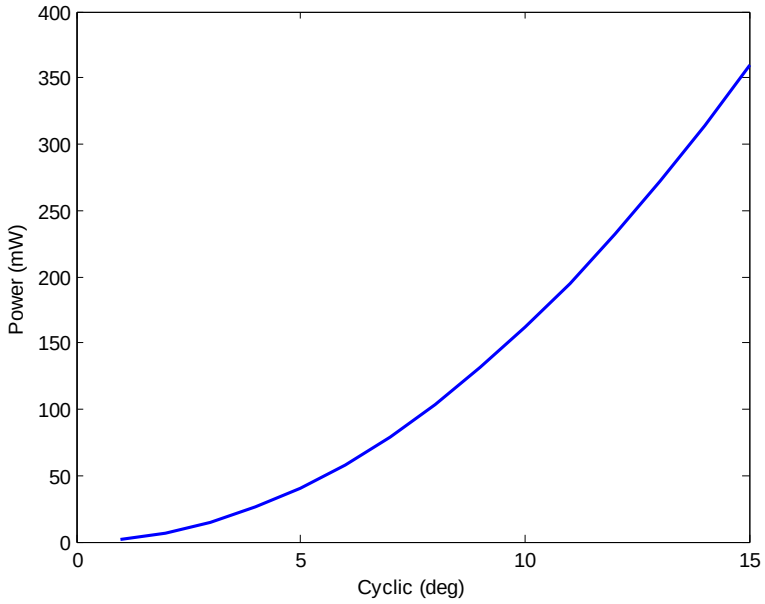

Figure **2-20**: Available Power Curve for Linear Harvester. This design has enough energy to meet the required minimum.

In order for the linear harvester design to work properly and have a natural frequency close to the driving frequency of 4.3 Hz, a spring constant of 3.65 N/m would have to be achieved. This is a very low spring constant that is difficult to achieve. This is especially true when the spring needs to act in both compression and tension and be small enough to fit into the design space. Another way of realizing a linear spring is to use a magnetic field, where the opposing forces from magnets act as effective spring constants. However, this is not possible in this case because of the centrifugal forces that will be acting on the proof mass. For these reasons a different design will have to be used.

2.4 Centrifugal Pendulum Harvester Design

Some of the problems with the linear harvester were controlling the amplitude, realizing the necessary spring constant, and dealing with the centrifugal forces. One way to deal with some

of these problems is to use the centrifugal force as the effective spring instead of relying on a mechanical spring. This can be achieved by a centrifugal pendulum in which the proof mass is hinged on the inside wall of the rod end and the mass is placed in line with the centrifugal force. The hinge would alleviate the need to deal with the angular movement of the pitch link. A free body diagram of a system like this is in Figure 2-21.

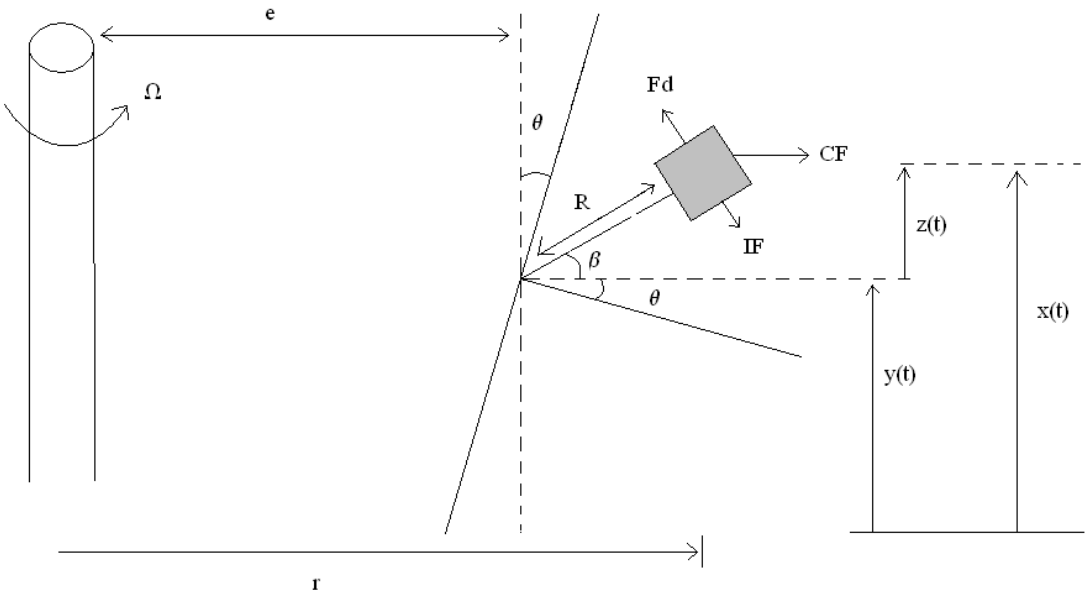

Figure **2-21**: Free Body Diagram of a Centrifugal Pendulum Harvester that uses the Centrifugal Force as an Effective Spring.

The dynamics of this system are similar to that of the linear harvester if we assume small amplitudes and linear motion of the proof mass. The distance *e* is the distance from the rotating shaft to the pitch link and *r* is the distance from the rotating shaft to proof mass. Using the small angle assumption, $z = (r-e)\beta$ and $z(t) = x(t) - y(t)$. The following table summarizes the forces acting on the proof mass and each of their arms. CF stands for centrifugal force, IF stands for inertial force, and F_d is the damping force.

Table **2-1**: Forces acting on Centrifugal Pendulum Harvester Proof Mass.

	Force	Arm
CF:	$m\Omega^2 r$	z
IF:	$m\ddot{x} = m(\ddot{z} + \ddot{y})$	$r - e$
F_d:	$D\dot{z}$	$r - e$

Summing forces on the mass about the hinge, the differential equation of motion for the device is:

$$\sum M_{hinge} = m(r-e)\ddot{x} + D(r-e)\dot{z} + m\Omega^2 rz = 0 \ . \tag{2.1}$$

Substituting in the expression for x(t):

$$m(r-e)\ddot{z} + D(r-e)\dot{z} + m\Omega^2 rz = -m(r-e)\ddot{y} \, . \tag{2.2}$$

Dividing through by m(r-e) we get the differential equation of motion for the centrifugal pendulum where the constant in front of the z term represents the stiffness of the system due to the centrifugal force.

$$\ddot{z} + \frac{D}{m}\dot{z} + \frac{\Omega^2 r}{(r-e)} z = -\ddot{y} \ . \tag{2.3}$$

Taking the Laplace transform and re-arranging gives the transfer function in the s-domain from base input motion Y, to proof mass output motion Z, with the centrifugal force providing the system stiffness.

$$\frac{Z(s)}{Y(s)} = \frac{-s^2}{s^2 + \frac{D}{m}s + \frac{\Omega^2 r}{(r-e)}} . \tag{2.4}$$

It is known that $D = 2m\varsigma\omega_n$ where m is the proof mass, ω_n is the natural frequency of the system, and ζ is total system damping, both mechanical and electrical. Substituting into the

above transfer function and also naming the stiffness term, *k*, we again get the transfer function from input motion to output motion:

$$\frac{Z(s)}{Y(s)} = \frac{-s^2}{s^2 + 2\varsigma\omega_n s + k}. \tag{2.5}$$

If *e* were much less than *r*, than the stiffness term *k* would go closer to Ω^2 and the natural frequency of the system would be proportional to the rotational speed of the rotor. If this were true than the system would always be tuned close to 1/rev. However, *e* is not much less than *r* and the systems natural frequency is not tuned to the rotational speed of the rotor. This transfer function was once again implemented in Simulink and the parameters of it were defined in a MATLAB script. The diagram of the Simulink model is in Figure 2-22 where the base motion from the pitch link is fed into the transfer function.

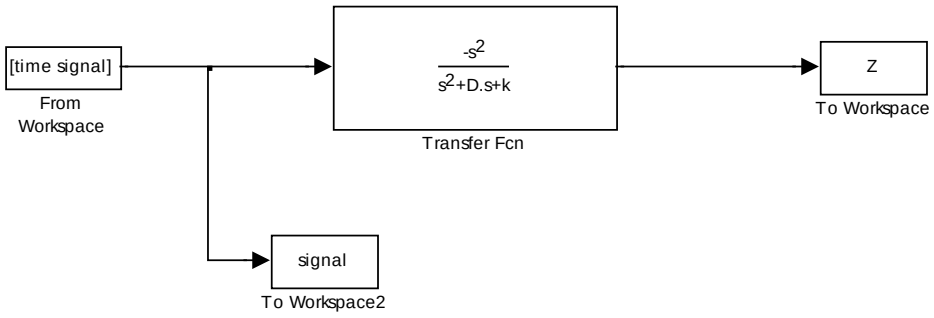

Figure **2-22**: Simulink Model for Centrifugal Pendulum Harvester.

The motion of the proof mass at 20° collective and 10° cyclic is used as an example in Figure 2-23. At this flight condition the pitch link experiences an acceleration of 20.59 m/s^2. The values used in the simulation were a 5 gram mass, a driving frequency of 27 rad/s, a total system damping ratio of 0.05, *r* equal to 0.42m, and *e* equal to 0.41m.

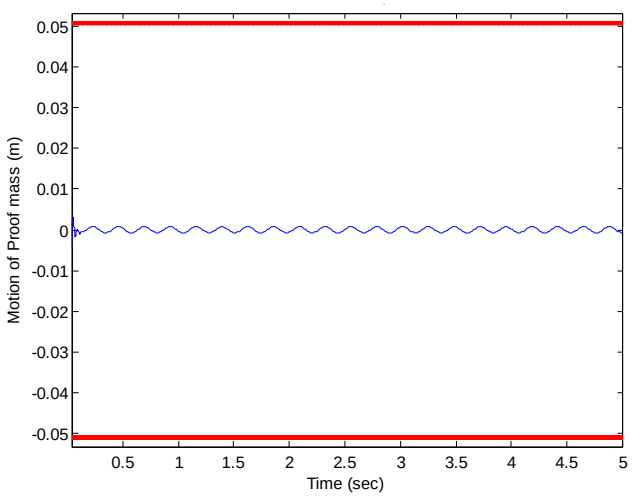

Figure **2-23**: Proof Mass Motion for Centrifugal Pendulum Harvester Shows that the System is Very Stiff.

The stiffening of the system in this configuration is very high and allows little relative motion of the proof mass and quality factor much less than 1. This, in turn, provides very little available power to be harvested because the frequency is very low. The natural frequency of the harvester is 168 rad/s making the frequency ratio 6.2. The available power for all flight conditions for this design are in Figure 2-24.

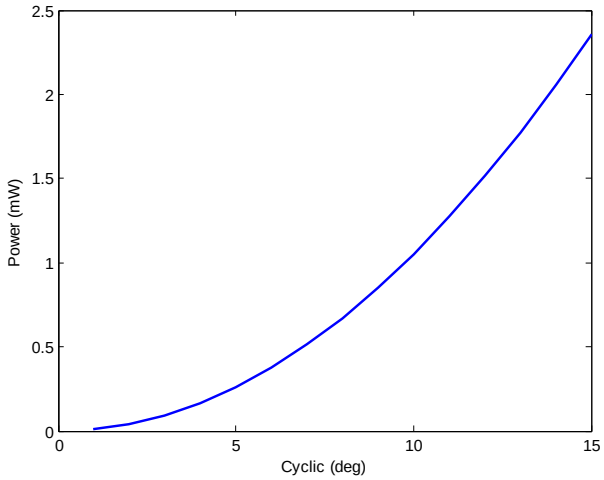

Figure **2-24**: Available Power for Centrifugal Pendulum Harvester. There is not enough available power for this design.

From the figure it is obvious that there is not enough available power at most flight conditions to power a wireless sensor. This would be expected due to the low quality factor and off resonance frequency. Therefore, the major drawback of this configuration is that it is too stiff to allow the needed amplitude and quality factor necessary to meet the power requirements. It also has a natural frequency much higher than the driving frequency. It does however, offer very little mechanical damping and uses the centrifugal force to its advantage instead of having mechanical losses in a bearing system. The next design which is very similar in nature, addresses these issues to allow better response from the system.

2.5 Reverse Centrifugal Pendulum Harvester Design

The issues of the previous design can be overcome by mounting the hinge of the pendulum on the reverse side of the rod end, still keeping the proof mass in line with the centrifugal forces. This design will have a torsional spring at the hinge that will allow the system to be tuned based on the choice of m and k. How this will be accomplished will be shown later. A free body diagram of this system is shown in Figure 2-25.

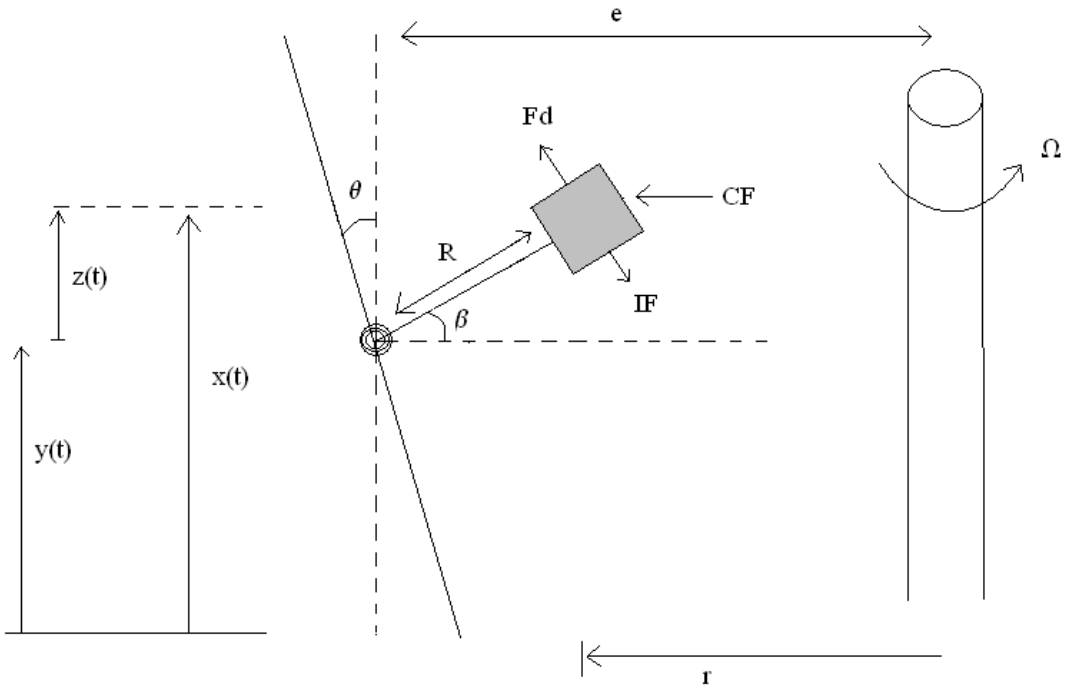

Figure **2-25**: Free Body Diagram of Reverse Centrifugal Pendulum to Derive the Equation of Motion.

In this diagram *e* is once again the distance from the rotating shaft to the hinge, *r* is the distance to the proof mass, CF represents the centrifugal force, IF represents the inertial force, F_d represents the damping force, and SF is the spring force from the torsional spring at the base. The small angle assumption is once again z = (e-r)β.

Table **2-2**: Forces acting on Reverse Centrifugal Pendulum Harvester Proof Mass.

Force	Arm
CF: $m\Omega^2 r$	z
IF: $m\ddot{x} = m(\ddot{z} + \ddot{y})$	$e-r$
F_d: $D\dot{z}$	$e-r$
SF: $K\beta = K\frac{Z}{e-r}$	

To get the differential equation of motion for the system, first sum moments about the hinge:

$$\sum M_{hinge} = m(e-r)\ddot{x} + D(e-r)\dot{z} + K_{tor}\left(\frac{z}{e-r}\right) - m\Omega^2 rz = 0. \tag{2.6}$$

Substitute in x = z + y to get the equation in terms of input and output motions.

$$m(e-r)\ddot{z} + D(e-r)\dot{z} + K_{tor}\left(\frac{z}{e-r}\right) - m\Omega^2 rz = -m(e-r)\ddot{y}. \tag{2.7}$$

Dividing through by m(e-r) gives the equation of motion for the reverse centrifugal pendulum:

$$\ddot{z} + \frac{D}{m}\dot{z} + \left[\frac{K_{tor}}{m(e-r)^2} - \frac{\Omega^2 r}{e-r}\right]z = -\ddot{y}. \tag{2.8}$$

To get the transfer function from input motion to output motion, take the Laplace transform of the above differential equation and rearrange:

$$\frac{Z(s)}{Y(s)} = \frac{-s^2}{s^2 + \frac{D}{m}s + \left[\frac{K_{tor}}{m(e-r)^2} - \frac{\Omega^2 r}{e-r}\right]}. \tag{2.9}$$

Once again knowing that $D = 2m\varsigma\omega_n$ and the stiffness term, *k*, is once again the constant in front of the z term in the differential equation above, the transfer function can be written:

$$\frac{Z(s)}{Y(s)} = \frac{-s^2}{s^2 + 2\varsigma\omega_n s + k}. \tag{2.10}$$

This is the same transfer function as for the centrifugal pendulum harvester described in Section 2.4 with the key difference being the stiffness term *k*. Comparing the stiffness terms, it can be seen that the centrifugal pendulum gets its stiffness entirely from the centrifugal force and choice of mass. The reverse centrifugal pendulum system is actually softened by the centrifugal force term. It, therefore, can be tuned based on the choice for the torsional spring constant.

Figure 2-26 displays the natural frequency of the system based on the choice for K_{tor}. The mass used in the graph is 5 grams, e is now equal to 0.43 m, and r is now equal to 0.42m.

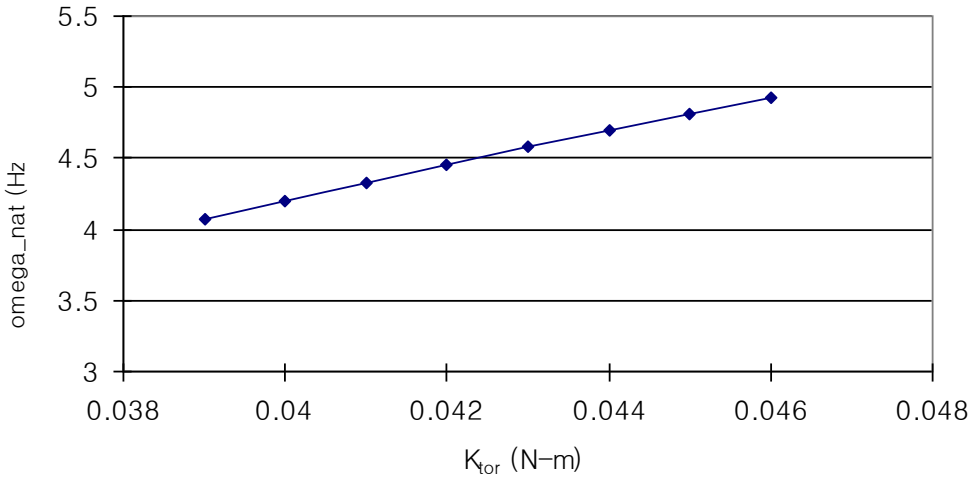

Figure **2-26**: Effect on Natural Frequency of the Harvester based on Choice of Torsion Spring.

The above graph shows that small changes in the torsional spring can mean a large difference in the natural frequency of the system

The Simulink diagram for this system is the same as that for the previous system and can be seen in Figure 2-22 in Section 2.4. The proof mass response for this system at 1/rev is shown for 20^o collective and 3^o cyclic as an example.

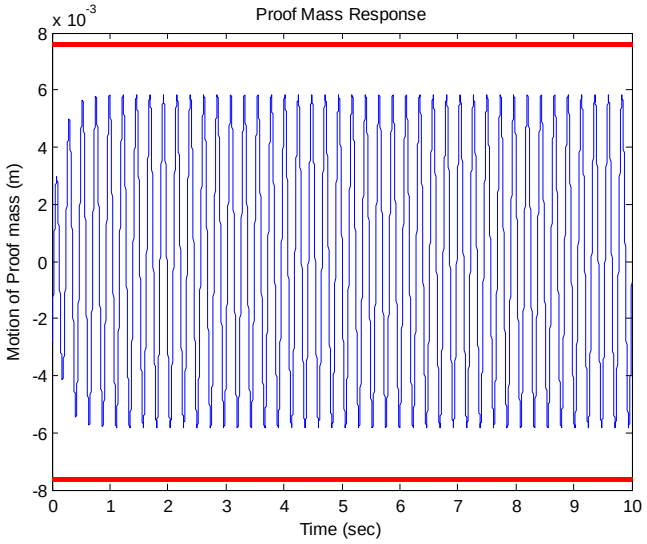

Figure **2-27**: Example of Proof Mass Response When Driven at 1/rev. The base motion amplitude is 8.4 mm.

Choosing a torsional spring constant for the system that allows a 1/rev response may not be the ideal case as it will violate the displacement constraint condition. The response at the same flight condition in Figure 2-27 for a system with a torsional spring constant of 0.0259 N-m is seen in Figure 2-28. This system has a natural frequency of 81 Hz or 3/rev. The amplitude of the response of the proof mass when its natural frequency does not match the driving frequency is much lower. This will have an affect on the available power there is to harvest.

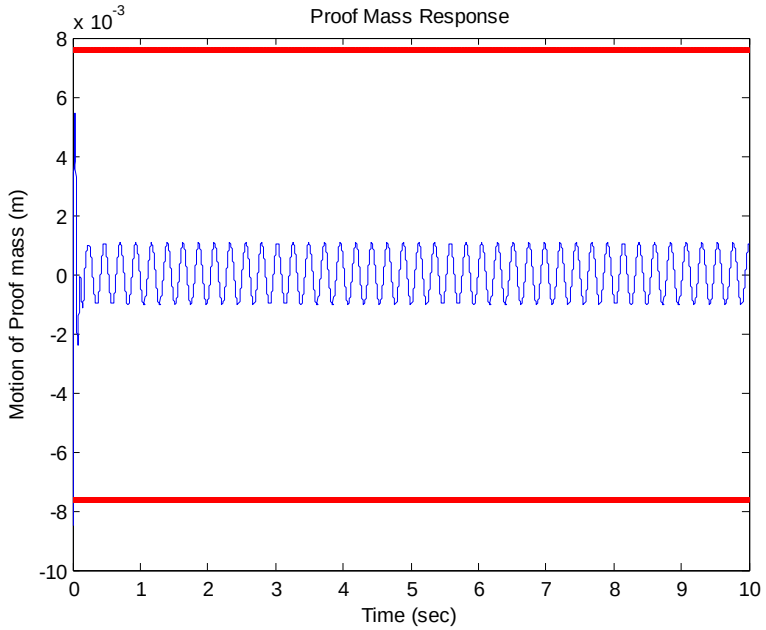

Figure **2-28**: Proof Mass Response When Driven at 3/rev.

To choose the spring term it is also important to remember that a robust design is needed. If the spring constant is off from what it is expected to be, the available power there is to harvest could be vastly different from what was predicted. Figure 2-29 shows the available power versus the choice of K_{tor}. Notice that the available power is highest when the device natural frequency is very close to the driving natural frequency but falls off greatly after that. If the device were allowed to operate on the flatter part of the curve, less power would be available but a more robust system could be realized where the material constants could have some degree of flexibility.

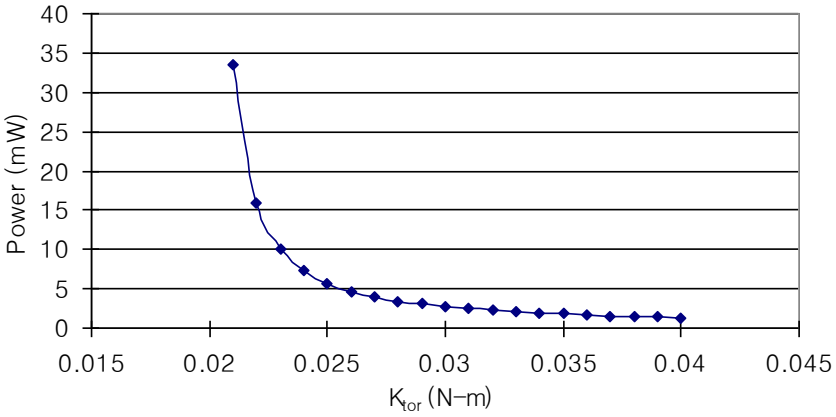

Figure **2-29**: Power vs. Torsion Spring Constant. More power is available when the harvester natural frequency matches the driving natural frequency.

If allowed to be driven at 1/rev, the reverse centrifugal harvester design has the following available power curve for all flight conditions. Notice that the available power, just like pitch link amplitude and acceleration, depends only on the value of cyclic pitch and that the greater acceleration the pitch link experiences, the more power there is to harvest.

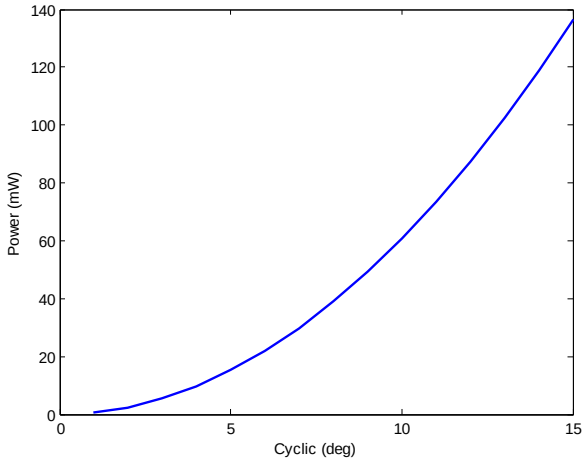

Figure **2-30**: Available Power for Reverse Pendulum at 1/rev. The available power is enough to power a wireless sensor

For comparison, if the natural frequency of the harvester is three times the driving frequency, it will have the power curve of Figure 2-31. There is a significant drop-off in the

available power there is to harvest compared to Figure 2-30 and illustrates the importance of constructing a system that operates as close to the natural frequency of the source vibration as possible.

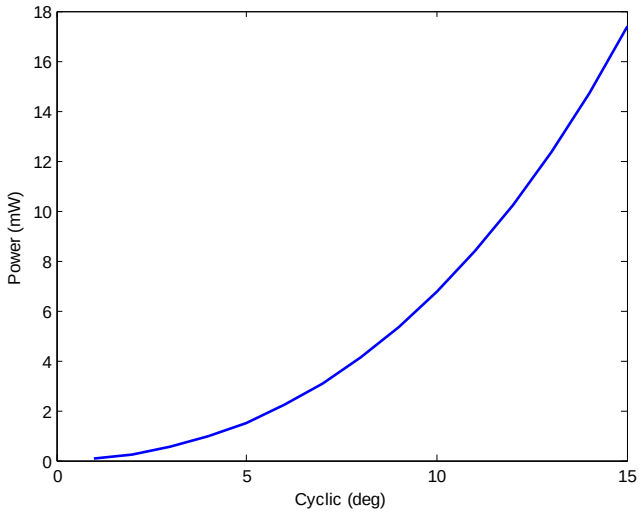

Figure **2-31**: Available Power for Reverse Pendulum at 3/rev. There is much less available power when the natural frequency of the harvester does not match the driving vibration frequency.

2.6 Magnet and Coil Design

The above design work focuses on the mass-spring system. The other important part of designing an energy harvester relates to the magnet and coil. The magnet will act as the proof mass for the system and the interaction described in Chapter 1 between the coil and magnet will give the system electrical damping. There are four types of magnets considered for the design. Properties of all four are in Table 2-3 [9]. BH_{MAX} refers to the maximum energy product of the magnet and Curie temperature is the maximum operating temperature the material can withstand before the magnet becomes demagnetized.

Table **2-3**: Comparison of Magnetic Materials [9].

Material	BH_{MAX} (kJ/m^3)	Flux density (mT)	Curie Temp (^oC)	Density (kg/m^3)
Ceramic	26	100	460	4980
Alnico	42	130	860	7200
SmCo	208	350	750	8400
NdFeB	306	450	320	7470

Ceramic magnets are hard and brittle and are available in a wide range of compositions. They are classified as either soft or hard depending on their coercivity. Alnico magnets are alloys of aluminum, nickel, cobalt, copper, iron, and titanium. They are stable with temperature and can be used in high temperature applications. Samarium cobalt is a rare earth magnet that has a higher magnetic field than the alnico or ceramic magnets. They have good thermal stability and corrosion resistance. NdFeB magnets are also rare earth magnets made from neodymium, iron, and boron. They have the highest maximum energy product but a low working temperature and poor corrosion resistance [9].

NdFeB magnets, also known as neodymium magnets, have been chosen for this application because of their high maximum energy product, flux density and material density. The fact that they have a low Curie temperature and poor corrosion resistance did not play a part in the decision based on the environment in which they will be working.

The design of the coil will also have a great effect on the voltages that can be produced. The expected voltages over time will be $v(t) = NLB\dot{z}(t)$, where N is the number of turns in the coil, L is the average length of turn, B is the magnetic flux density and $\dot{z}(t)$ is velocity the magnet moves through the coil. The number of turns is governed by the geometry of the coil, the diameter of the wire it is wound from, and the density with which the coil wire has been wound. Insulated wire will not fill the coil volume entirely with conductive material. The percentage of copper within a coil is given by its fill factor, *f*. The fill factor helps relate the area of wire to the

overall cross sectional area of the coil. The copper fill factor depends on the tightness of winding, variation in insulation thickness, and winding shape. The formula relating the areas is $A_{wire} = fA_{coil} / N$, where N is the number of turns in the coil [9].

A simple geometric drawing of a coil with a circular cross section is shown below in Figure 2-32 [9]. Assuming the circular cross section, formulas can be derived to obtain some of the coil's important properties.

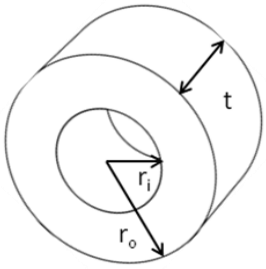

Figure **2-32**: Geometric Representation of Circular Cross section Coil [9].

The symbols used in the above Figure and the following equations are given here:

r_i: coil inner radius

r_o: coil outer radius

t: coil thickness

w_d: wire diameter

A_w: area of wire (conductor only)

A_{coil}: area of coil

L_{mt}: length of mean turn

ρ: resistivity of coil material

The formula for the entire volume of the coil is:

$$V_T = \pi\left(r_o^2 - r_i^2\right)t. \tag{2.11}$$

The formula for length of wire needed to wind a coil for a specific volume is:

$$L_w = \frac{4 f V_T}{\pi w_d^2}. \tag{2.12}$$

The coil resistance formula is then:

$$R_c = \rho \frac{L_w}{A_w} = \rho \frac{N L_{mt}}{A_w} = \rho \frac{N^2 \pi \left(r_o + r_i \right)}{f \left(r_o - r_i \right) t}. \tag{2.13}$$

Finally, the number of turns in the coil can be found by the following formula:

$$N = \frac{L_w}{r_i + \frac{\left(r_o - r_i \right)}{2}}. \tag{2.14}$$

Using all of these formulas it is possible to determine the voltage that a coil and magnet will produce based on the velocity of the proof mass, which in this case will be the magnet. As already discussed , however, the voltage generated will differ from what is predicted by the equation due to the differences in magnet and coil placement.

Chapter 2 has discussed the base motion and centrifugal forces an electromagnetic harvester with a proof mass will experience. Different design ideas were discussed and analyzed to see if they would be practical to implement and also if they could meet the power requirements. The quality factor and frequency ratio of each design has led to the further development of the reverse centrifugal pendulum design, which analytically performed well in both categories. The next chapter will discuss the implementation of the reverse centrifugal pendulum harvester design and the experimental procedure used to test it.

Chapter 3

Experimental Testing of Energy Harvesting Device

This chapter details the fabrication of the harvesting device, the electronics associated with it, and the experimental set up and procedure used to test the device. Predictions on mass motion, voltage generated, and power generated are given and compared with their experimental values. Two different harvesters are built, however only one is tested due to time constraints. The goal of the chapter is to build an energy harvester based on the reverse pendulum design and to experimentally evaluate the device and compare the results to analytical predictions.

3.1 Experimental Procedure

The experimental procedure used to test the device is designed to gain a full understanding of the dynamics of each system and obtain estimates of system properties. A base motion system was constructed to match the frequency and amplitude of the pitch link for different pilot inputs. This enabled the harvester to be subjected to the whole range of flight conditions it would see in flight. The centrifugal force was simulated with a mass and pulley system that will be described later. For operational procedures of the base motion system, refer to Appendix A.

First, system parameters k, m, and ζ_m were experimentally measured. These values were used to update the analytical model to predict mass motion and voltage. The mass motion was then obtained experimentally at all flight conditions from 1^o cyclic to 15^o cyclic. The coil then allowed AC voltages to be measured. At this point it can be determined if the voltage needs to be stepped up and if there is a way to accomplish that. Finally, a representative load is placed to

draw current and measure the power output of the device. This procedure is outlined in the following flowchart.

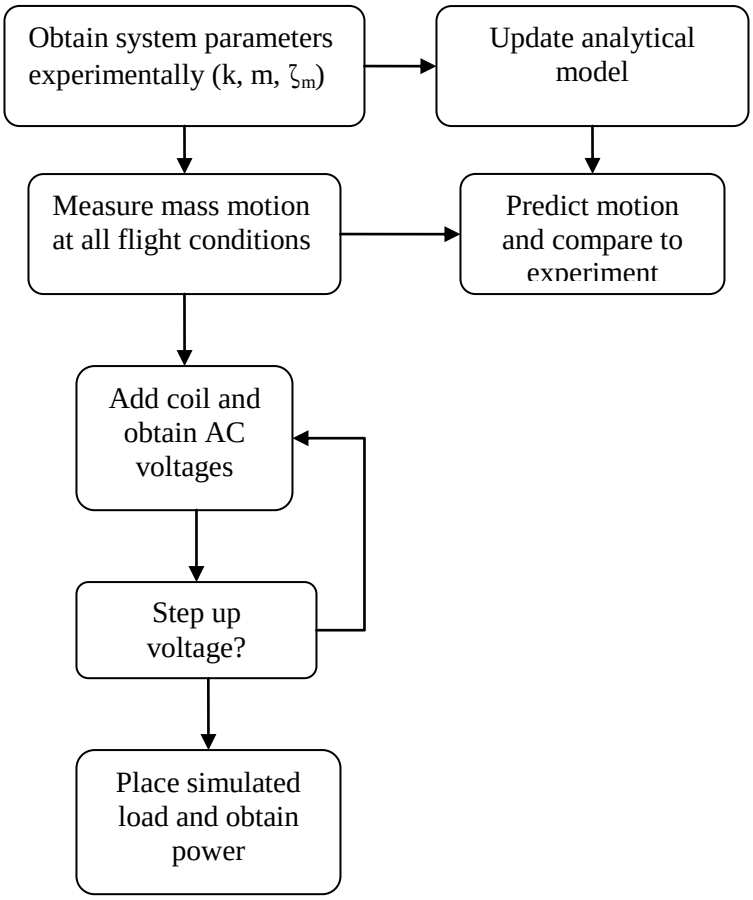

Figure **3-1**: Flowchart of Experimental Procedure for Testing of Harvester. This is the procedure that should be used to obtain useful power.

At all stages of experimentation, results are compared to predictions made using the analytical model in MATLAB and Simulink. The experiment is first done without any centrifugal force to obtain baseline parameters. Increasing increments of force are then placed on the device to study trends and verify predictions. The next section describes the setup built to carry out the experiment.

3.2 Experimental Setup

The experimental setup included a base motion system that could mimic the motion of a pitch link in flight. This was achieved through the use of a large electromechanical shaker driving a lever system that amplified the motion. The purpose of the amplification lever was to ensure that the required amplitude (2.8 mm to 42 mm) could be achieved. The entire length of the lever is 36 inches and it is hinged at 9 inches. This makes the ratio of input to output 9:27 or 1:3, meaning that the output at the rod end will be three times the amplitude of the input at the shaker. The shaker and lever system are shown below in Figure 3-2.

Figure 3-**2**: Shaker and Lever System Test Setup used to Test the Harvester Device showing the shaker, amplification lever, and rod end.

The motion of the lever system needs to be restricted to vertical motion and have its greatest accelerations in that direction. This was monitored by a tri-axial accelerometer placed at the end of the lever, on the base, where the system is simulating the motion of the pitch link. The accelerometer is pictured in Figure 3-3.

Figure **3-3**: Tri-axial Accelerometer to Monitor Base Motion System. The accelerometer measures vibrations in three directions ensuring that the base motion system produces accelerations that mimic a pitch link in flight

The decibel ratio of vertical acceleration (y) to lateral acceleration (x) was calculated in order to ensure that the system met the goal of predominantly vertical acceleration. This was calculated by the dB ratio formula:

$$dB_{ratio} = 20\log\left(\frac{Y_{accel}}{X_{accel}}\right). \tag{3.1}$$

Table 3.1 shows that for flight conditions ranging from 1^{o} collective to 12^{o} collective the average dB ratio was 18.5. This is an acceptable value to say that the system has greater acceleration in the vertical direction (y) than in the lateral direction (x) and is acceptable for testing. This was necessary to ensure the harvester was not being vibrated in any other direction that could greatly affect the results of any test.

Table **3-1**: Vertical to Lateral Acceleration dB Ratios.

Acceleration (m/s^2)	Accel Decibel Ratio
2.04	19.53
4.09	16.27
6.13	19.01
8.25	21.35
10.29	22.35
12.34	17.91
14.38	18.02
16.43	17.24
18.54	16.58
20.59	17.49
22.63	17.38
24.68	15.63

The shaker is driven by an amplifier that is controlled by a signal generator. The output of the signal generator and the output of the tri-axial accelerometer were monitored by an oscilloscope to ensure that the correct inputs to the shaker were being made for the different flight conditions. Figure 3-4 below gives an example oscilloscope reading. The top (yellow) line indicates the output from the amplifier driving the shaker and the bottom (blue) line indicates the output from the accelerometer at the base of the system.

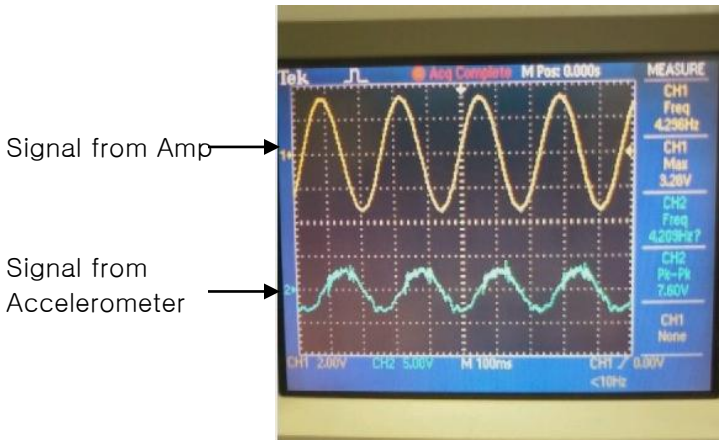

Figure **3-4**: Oscilloscope Output Monitoring Base Motion System. The top waveform indicates the signal being sent to amplifier and the bottom wave indicates the signal from the accelerometer monitoring the base motion system

An overall schematic of the test rig is in Figure 3-5. This drawing shows the shaker, amplifier level, rod end, tri-axial accelerometer for monitoring the base motion, the signal generator and amplifier that drive the shaker, and the oscilloscope that monitors the system

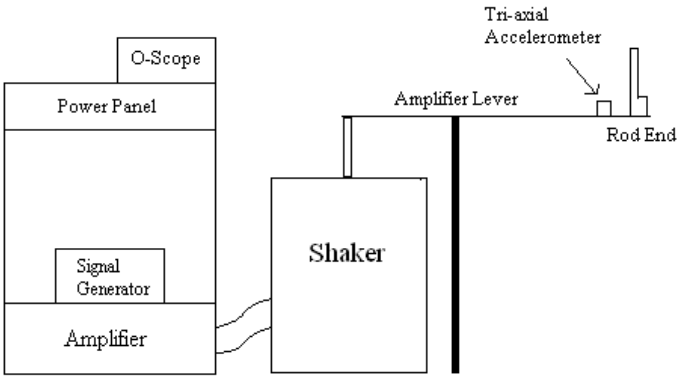

Figure **3-5**: Overall Test Stand Schematic. The test rig includes the signal generator, amplifier, shaker, and amplification lever as the base motion system and the accelerometer and oscilloscope used to monitor it.

Both harvesters were designed to operate under high centrifugal forces. In order to simulate this force a mass and pulley system was constructed. The goal of the mass-pulley system is to put a constant force on the proof mass equal to the centrifugal force it would see in the pitch link under rotation. A schematic and picture of the system is shown below in Figure 3-6.

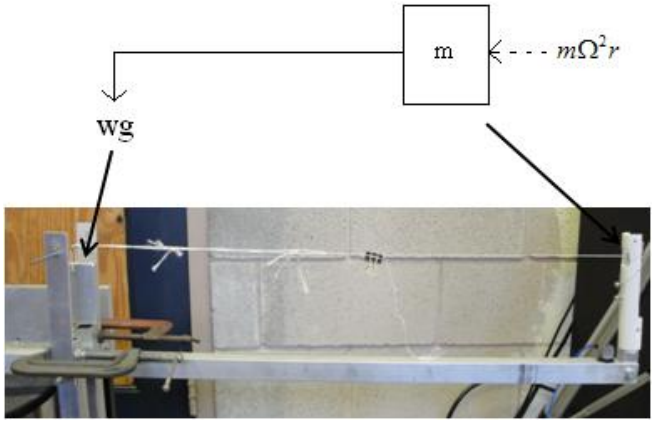

Figure **3-6**: Mass-Pulley System to Simulate the Centrifugal Force.

The centrifugal force will be proportional to the mass of the system, $m\omega^2 r$, where omega is equal to 27.02 rad/s and r is equal to 0.41 meters. For the reverse centrifugal harvester with a mass of 5 grams, this force is equal to 1.496 N. To simulate this force with $F = wg$, w must be approximately 152 grams with g equal to 9.81 m/s^2. For the linear reverse centrifugal harvester with a system mass of 8 grams, the simulated centrifugal force will be 2.394 N which requires a mass of 244 grams to simulate. A picture of a 122 gram mass hanging from the pulley is below in Figure 3-7.

Figure **3-7**: Hanging Mass Representing Centrifugal Force. Different masses indicate different values of centrifugal force.

The next section describes how each harvester was manufactured to fit inside the design space including the magnet (proof mass), brackets, and torsion spring.

3.3 Fabrication of Harvester Device

Two harvesters were constructed based on the reverse pendulum idea outlined in the previous chapter. The first harvester was constructed from 1/8 inch (3.175 mm) thick aluminum in two pieces, which clamped down onto music wire, where the wire acted as the torsion spring.

The wire was 0.012 inches (0.305 mm) in diameter and provided a torsion spring constant of .0187 N-m. Clamping onto the wire proved to be a challenge and many different ways of accomplishing it were evaluated. The final solution was to use a screw that tightened the two halves together. A CAD drawing of the device can be seen in Figure 3-8. The screw is shown in the photo of the device in Figure 3-9.

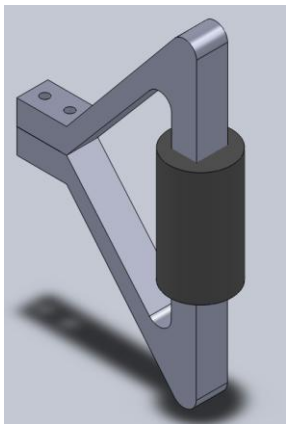

Figure **3-8**: CAD Drawing of Reverse Pendulum Harvester. The harvester was cut from a water jet machine in two pieces. The two aluminum pieces were clamped with a screw onto a magnet and a piece of music wire that acted as a spring

Figure **3-9**: Photo of the Reverse Pendulum Harvester showing how the device looks after completion.

The magnet used in the device was a neodymium magnet with a flux density of 0.7172 Teslas and a mass of 3 grams. The total device volume and mass were 3.84 cm^3 and 5 grams. The maximum vertical mass motion of the center of gravity of this device is limited to 0.5 inches (12.7 mm). This design does not allow the magnet to pass through the center of a cylindrical coil. The coil was placed next to the moving magnet in the experiment. This arrangement still allowed voltage to be generated. The difference in voltage generated for a magnet in the center of a coil versus a magnet next to a coil will be discussed in Section 3.5.4.

The second device built was also based on the reverse pendulum design with the exception that the magnet was restricted to mostly vertical motion. This allowed the coil to be placed around the magnet, in theory generating more voltage than placing the coil near the magnet. This device also had a torsion spring but included three hinges as seen in the CAD drawing below.

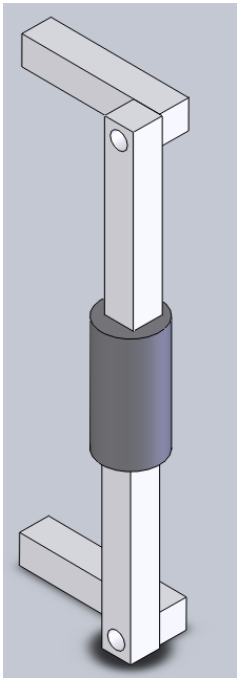

Figure **3-10**: CAD Drawing of Linear Reverse Pendulum Harvester. This device also utilized music wire to act as a spring but required three hinges which increased mechanical damping.

Figure **3-11**: Photo of Linear Reverse Pendulum Harvester. The magnet was attached with spring pins. The top back hinge is a Teflon rod and the other two hinges are shoulder bolts. Plastic spacers were used to keep the device in line

The magnet used in the linear reverse pendulum harvester was also a neodymium magnet with a flux density of 0.7172 Teslas and having a mass of 3.02 grams. The total device volume is 12.29 cm^3 and has a total mass of 8 grams. This design allows a maximum mass motion of 0.5 inches (12.7 mm) vertically from its equilibrium position. A free body diagram of this device is shown below. The following analysis shows that this configuration produces the same differential equation of motion and therefore will dynamically act the same as the reverse pendulum harvester.

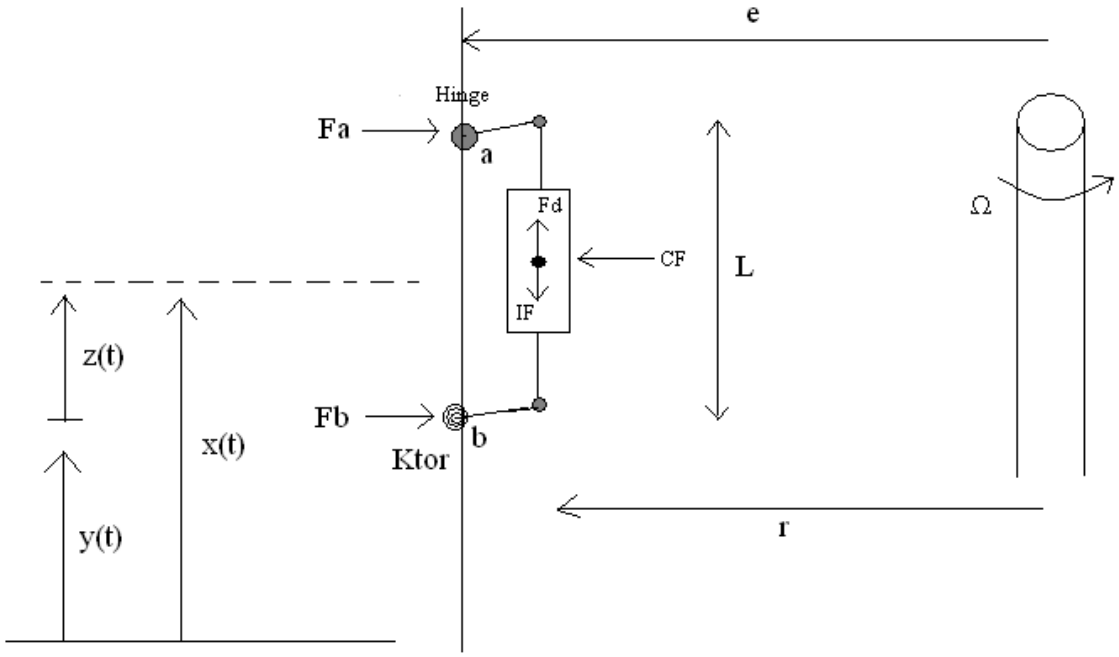

Figure **3-12**: Linear Reverse Pendulum Harvester Free Body Diagram shows that it is the same dynamic system as the Reverse Pendulum Harvester Design.

Summing the forces in the x direction, it can be seen that $F_a + F_b = CF$ and that $F_a = F_b$ because of symmetry. Therefore $F_a = 1/2*CF$. This will be important when summing moments about point b which contains the torsional spring. Table 3-2 below summarizes the forces acting on the mass with the small angle assumption.

Table **3-2**: Forces Acting on Proof Mass.

Force		Arm
CF:	$m\Omega^2 r$	$z + L/2$
IF:	$m\ddot{x} = m(\ddot{z} + \ddot{y})$	$e - r$
F_d:	$D\dot{z}$	$e - r$
SF:	$K\beta = K\frac{Z}{e-r}$	

Summing moments about point b:

$$\sum M_B = m(e-r)(\ddot{z}+\ddot{y}) + D(e-r)\dot{z} + K_{tor}\left(\frac{z}{e-r}\right) - m\Omega^2 r(z+L/2) + F_A L = 0. \qquad (3.2)$$

Substituting in the expression for F_a and rearranging gives:

$$m(e-r)\ddot{z} + D(e-r)\dot{z} + \left[\frac{K_{tor}}{e-r} - m\Omega^2 r\right] z - \frac{m\Omega^2 r}{2} L + \frac{m\Omega^2 r}{2} L = -m(e-r)\ddot{y}. \qquad (3.3)$$

Dividing by *m(e-r)* and reducing gives the equation of motion for the system:

$$\ddot{z} + \frac{D}{m}\dot{z} + \left[\frac{K_{tor}}{m(e-r)^2} - \frac{\Omega^2 r}{(e-r)}\right] z = -\ddot{y}. \qquad (3.4)$$

This equation exactly matches the equation of motion derived in section 2.5.

The device was constructed from aluminum to minimize the mass and shoulder bolts were used for two of the hinges. A Teflon rod was used for the top hinge that connected the device to the inner wall of the design space. The bottom of the device was connected to a torsion spring that was again music wire. This design allowed less angular rotation and more vertical motion. Figure 3-13 illustrates the point.

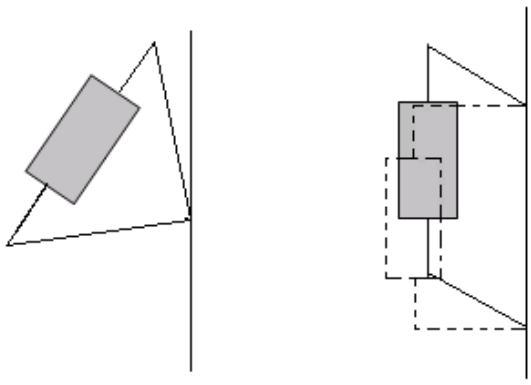

Figure **3-13**: Rotation and Translation of Harvester Devices. The pendulum configuration on the left allows for a large angular rotation. The linear configuration on the right allows for translation of the proof mass. The linear device was designed so that the magnet could go inside the coil instead of beside it.

3.3.1 Torsion Spring

The torsion spring will be the mechanical component responsible for tuning the device to the correct frequency. The design of the spring will depend on the mass of the system which includes the magnet and brackets. Since both devices have the same equation of motion, the spring term will be the same for both. From previous derivations the spring term is:

$$K = \frac{K_{tor}}{m(e-r)^2} - \frac{\Omega^2 r}{e-r}\,. \tag{3.5}$$

The frequency, omega, will be constant at 4.3 Hz from Section 2.1. The distance from the rotating shaft to the inside of the pitch link where the device is hinged is *e* and the distance from the rotating shaft to the proof mass is *r*. These values are 0.43 meters and 0.42 meters respectively. The following table shows different values of $K_{torsion}$ and the frequency of the device under rotation for the linear reverse pendulum harvester which has a mass of 8 grams.

Table **3-3**: Natural Frequency of Linear Reverse Harvester for Different Values of K Under Rotation.

K_{tor} (N-m)	K	ω_n (rad/s)	ω_n (Hz)
0.0335	843	29.0	4.62
0.034	1200	34.6	5.51
0.0345	1550	39.4	6.27
0.035	1900	43.6	6.94
0.0355	2260	47.5	7.56

The above table suggests that a small change in the torsion spring constant will have a big effect on the natural frequency of the device. The other device, a reverse pendulum harvester, has a mass of 5 grams, changing the spring constant to about half of what is needed for the 8 gram device. The table below shows how the natural frequency changes with spring constant for the reverse pendulum harvester.

Table **3-4**: Natural Frequency of Reverse Pendulum Harvester for Different Values of K Under Rotation.

K_{tor} (N-m)	K	ω_n (rad/s)	ω_n (Hz)
0.0143	0.0614	27.88	4.44
0.0153	0.1247	39.73	6.32
0.0163	0.1880	48.78	7.76
0.0173	0.2513	56.40	8.98
0.0183	0.3146	63.10	10.04
0.0193	0.3779	69.16	11.01

In order to achieve the above spring constants, a mechanical rod under torsion is examined. The mechanical rod will give a longer fatigue life and more consistent values than a mechanical torsion spring. The following figure shows a free body diagram of the torsion rod under a load.

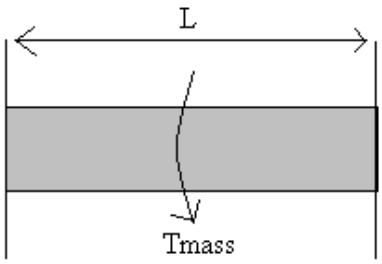

Figure **3-14**: Free Body Diagram of Torsion Rod Under Loading used to Determine the Length and Diameter to Achieve the Required Spring Constant.

Assuming the load is symmetrical and that the rod is clamped on both ends, the free body diagram can be cut in half for simplicity. This is seen in Figure 3-15.

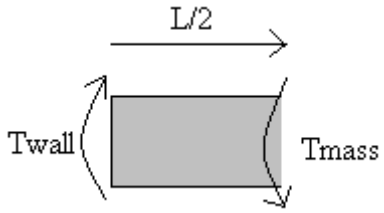

Figure **3-15**: Symmetrical Torsion Rod Under Loading.

The torque-twist relationship for the symmetrically loaded beam is:

$$\theta = \frac{T/2 * L/2}{GJ}. \tag{3.6}$$

The spring constant, K_{tor}, is found by $K_{tor} = T/\Theta$, which reduces to:

$$K_{tor} = \frac{T}{\theta} = \frac{4GJ}{L}. \tag{3.7}$$

Where J is equal to the following for a solid rod:

$$J = \frac{\pi R^4}{2}. \tag{3.8}$$

Reducing the expression for the spring constant it becomes:

$$K_{tor} = \frac{2G\pi R^4}{L}. \tag{3.9}$$

This equation can now be used to determine the required length, diameter, and shear modulus of the material to obtain the spring constants found in Tables 3-3 and 3-4.

Figure 3-16 shows a top view of the device with the torsion rod in place. The overall length of the rod will be limited by the design space and the width of the device.

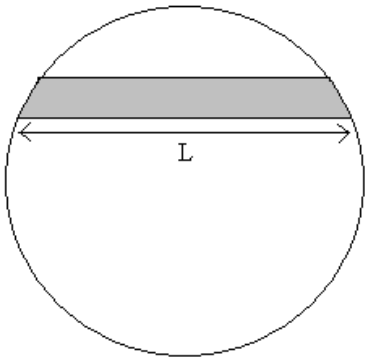

Figure **3-16**: Top View of Harvester Device with Torsion Rod shows how the length of the rod will impact dimensions for the rest of the device.

Due to the aforementioned constraints, the maximum length of the rod was found to be 0.4 inches (10.16 mm). Initially, different polymers were researched with standard stock diameters of 1/16 inch (1.59 mm) to 1/4 inch (6.35 mm). Given the shear moduli of the polymers like PEEK©, the required length of the rod to achieve the necessary spring constant is greater than the maximum of 0.4 inches (10.16 mm) allowed by the design constraints. The only other property of the rod that could be changed was the diameter. Steel music spring wire has a shear modulus of 80 GPa which is much greater than that of plastics, but it can be manufactured with diameters as low as 0.004". Using steel music wire with a shear modulus of 80 GPa and a length of 0.4 inches (10.16 mm), the following table shows the required diameter to achieve the spring constant desired. Table 3-5 is for the linear reverse pendulum harvester design with a mass of 8 grams and the second table is for the reverse pendulum harvester design with a mass of 5 grams.

Table **3-5**: Required Diameter of Wire to achieve Spring Constant for Linear Device.

K_{tor} (N-m)	Length (m)	Radius (m)	Diameter (in)
0.0335	0.01016	0.0001918	0.0151
0.034	0.01016	0.0001925	0.0152
0.0345	0.01016	0.0001932	0.0152
0.035	0.01016	0.0001939	0.0153
0.0355	0.01016	0.0001946	0.0153
0.036	0.01016	0.0001953	0.0154
0.0365	0.01016	0.000196	0.0154

Table **3-6**: Required Diameter of Wire to achieve Spring Constant for Reverse Pendulum.

K_{tor} (N-m)	Length (m)	Radius (m)	Diameter (in)
0.0167	0.01016	0.0001612	0.0127
0.0168	0.01016	0.0001614	0.0127
0.0169	0.01016	0.0001617	0.0127
0.017	0.01016	0.0001619	0.0127
0.0171	0.01016	0.0001621	0.0128
0.0172	0.01016	0.0001624	0.0128
0.0173	0.01016	0.0001626	0.0128

Steel music wire with diameters of 0.012 inches (0.305 mm) and 0.015 inches (0.381 mm) were used. The spring constant will change based on the tolerance of the wire diameter, the ability to clamp the length to 0.4 inches (10.16 mm) and the shear modulus of the steel. Based on these variables, the natural frequency of the system will change. It was therefore necessary to measure some of these properties and take into account the tolerance of the wire when predicting what spring constant the wire will actually provide.

3.4 Device Circuitry

The final goal of powering a sensor has to be achieved with some circuitry that converts the AC voltage into useful DC voltage. The first step is to take the AC voltage that is produced

by the harvester and pass it through a bridge rectifier that converts it to DC voltage. A bridge rectifier is made from four diodes that only allow the positive current to flow one direction and the negative current to flow in the other direction, thus producing direct current. A schematic of a full bridge rectifier is shown below.

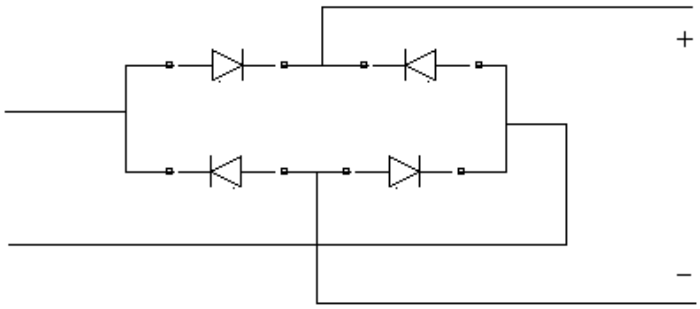

Figure **3-17**: Bridge Rectifier Schematic. Four diodes can be used to construct a bridge rectifier that converts AC voltage to DC voltage.

To illustrate the circuit design process a model was created in Simulink and MATLAB. The model included an AC voltage source that represented the energy harvester and was set to 1 volt. One volt was chosen after some preliminary experiments. This was connected to a step up transformer and then into the bridge rectifier to produce the necessary DC voltage. The circuit was completed with a resistive load. The schematic below shows the entire circuit.

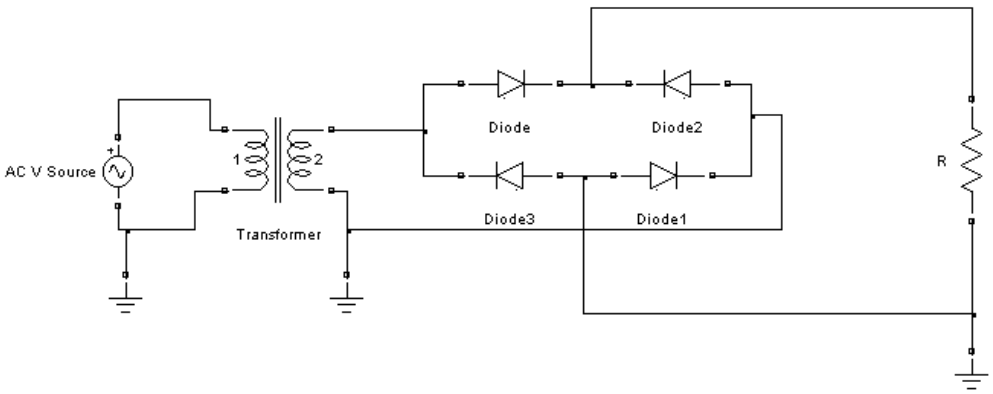

Figure **3-18**: Circuit Schematic used for Design. Circuit needed to produce useful DC voltages from the AC voltages produced by the harvester

The figure below shows the simulated AC voltage produced by the harvester in red circles. The voltage produced by the step up transformer is shown in solid blue and the DC voltage after passing through the bridge rectifier is shown as a black dotted line.

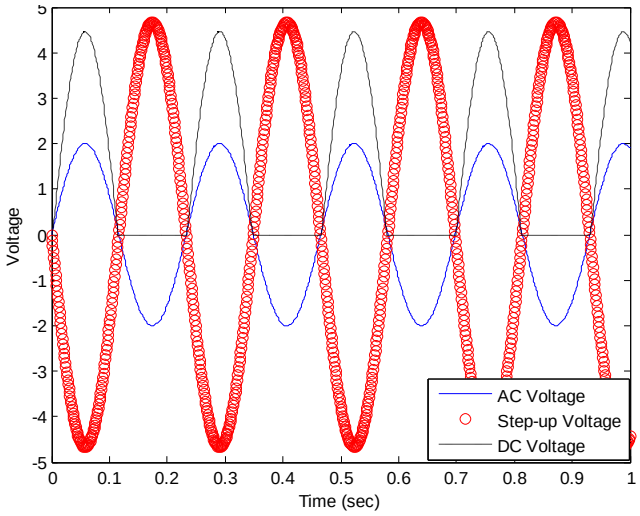

Figure **3-19**: Effect of Circuit on Generated Voltage. The original AC voltage was stepped up by the transformer which was converted into DC voltage by the bridge rectifier.

After passing through the bridge rectifier, the signal can be smoothed out by a capacitor. The smoothed out voltage signal is below in Figure 3-20.

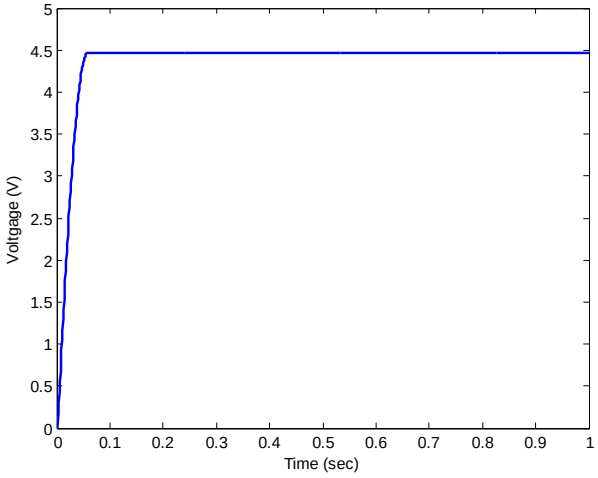

Figure **3-20**: Voltage after passing through a Capacitor. Smoothed voltage is easier to work with.

This voltage can now be used to power any sensor or a voltage regulator can be used to keep the voltage supply steady. The final design of the circuit may not include a transformer but may include a DC to DC converter that helps to step up the voltage. It will depend on the voltages produced by the harvester as to whether or not a voltage boost is needed. Silicon diodes have a voltage drop of 700 mV across them. If the voltage produced by the harvester is too low, then a bridge rectifier will kill the signal. In this case, a transformer could be used to boost the voltage before it is rectified. If the voltage produced by the harvester is an acceptable level (large enough not to kill the signal with a 1.4 volt drop), than the DC-DC converter can be used.

3.5 Testing of Device

Two different mechanical devices based on the reverse pendulum design were built but only one was tested. The mechanical differences have already been discussed. In this section the first reverse pendulum device will be tested to see if predictions made during the design process can be validated. First, the natural frequency of the device will be tested with and without the effect of the centrifugal force. Then the mechanical damping of the device will be measured to estimate system losses. Finally, predictions on mass motion, voltage generated and power generated will be tested for validation.

3.5.1 Natural Frequency Prediction and Validation

The reverse pendulum device was built to operate at approximately 1/rev which is about 4.3 Hz. This was achieved through the use of a thin music wire as the torsion spring with a diameter of 0.012 inches (0.305 mm). In order to obtain the natural frequency of the device, a laser vibrometer was used to measure the decay from an initial displacement test. Then, when the

decay was captured, the log decrement method was used to determine the mechanical damping, damped natural frequency, and ultimately the natural frequency of the device. This was done for the device with no centrifugal force and then for increasing increments of centrifugal force to see experimentally if the system's natural frequency was dropping like it was designed to do. The set-up for measuring the motion of the device is seen in Figure 3-21.

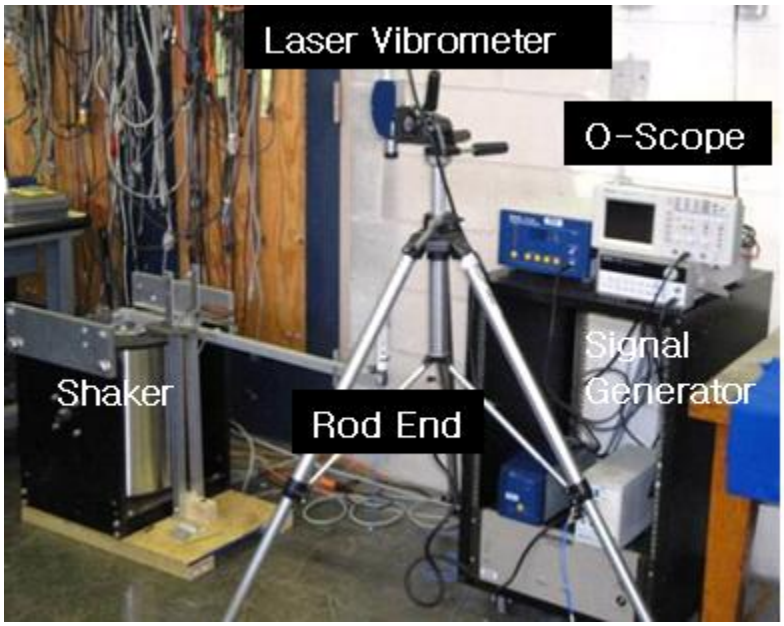

Figure **3-21**: Set-up for Measuring the Motion of the Device. The laser vibrometer was placed above the device and looked down on it to capture the motion in the vertical direction. A laptop and data acquisition system (not pictured) monitored and stored the data.

An example of the decay of the device from an initial displacement test is in Figure 3-22. This is for no centrifugal force acting on it. The units on the decay are time versus voltage. The laser vibrometer produces a voltage signal that can be converted to velocity with its sensitivity.

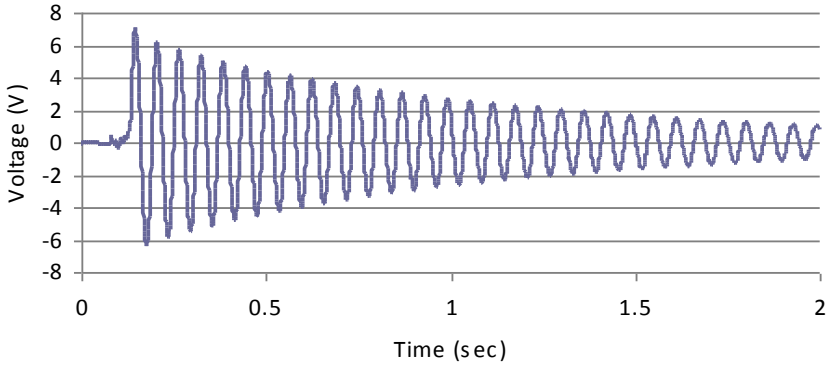

Figure **3-22**: Exponential Decay from Initial Displacement Test. This is one example that was used to calculate mechanical damping and natural frequency.

From the above data it is possible to determine the damped natural frequency, the mechanical damping, and the natural frequency of the device using the log decrement method. The log decrement method says that the logarithmic decrement of the amplitudes of any two successive peaks is:

$$\delta = \frac{1}{n}\ln\left(\frac{x_0}{x_n}\right). \tag{3.10}$$

Where x_0 is the greater of the two amplitudes and x_n is the amplitude of a peak n periods away. Using the logarithmic decrement the damping ratio can be found by:

$$\varsigma = \frac{1}{\sqrt{1+\left(\frac{2\pi}{\delta}\right)^2}}. \tag{3.11}$$

The damped natural frequency is then found by the following equation, where T, the period of the waveform, is the time between two successive peaks.

$$\omega_d = \frac{2\pi}{T}. \tag{3.12}$$

Finally, the undamped natural frequency of the device can be found:

$$\omega_n = \frac{\omega_d}{\sqrt{1-\varsigma^2}}. \tag{3.13}$$

The above was done for the reverse pendulum harvester at increasing amounts of centrifugal force and compared to predictions made about what should happen. The predictions included physical measurements of the device, including the clamped length L of the music wire from Section 3.3.1, the mass of the device, and the diameter of the wire. The wire diameter was 0.012 inches (0.305 mm) with a tolerance of 0.0003 inches (0.0076 mm). Shown below is a plot of natural frequency vs. centrifugal force for both the experiment and what was predicted to happen.

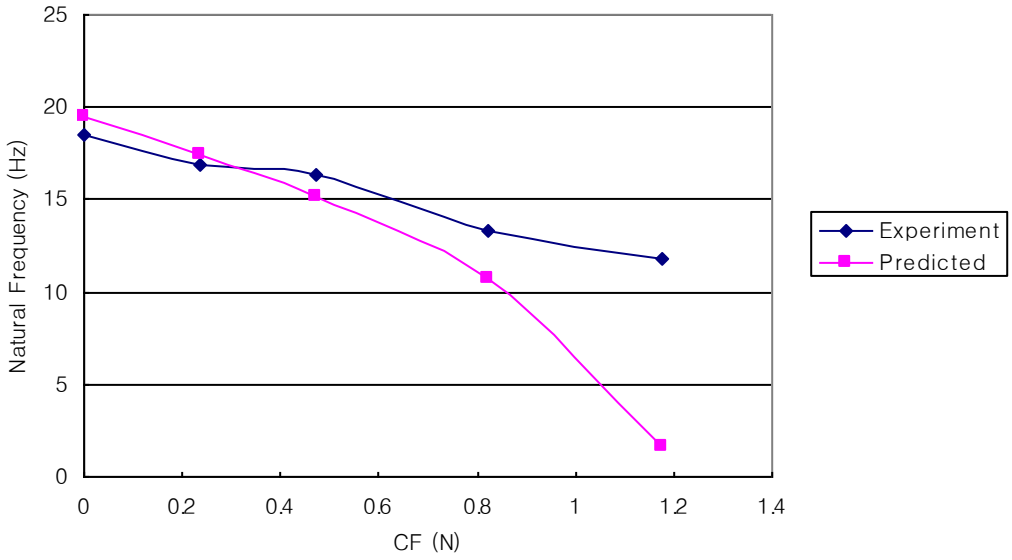

Figure **3-23**: Natural Frequency vs. Centrifugal Force. The predicted natural frequency of the device matched the experiment for four out of five points and the data shows that increasing the centrifugal force lowered the natural frequency of the harvester.

The natural frequency of the device found experimentally closely matched the model for 4 out of 5 data points up to 0.8 N of force, which is 68% of the full CF. The equation for natural frequency as a function of centrifugal force can be found in the spring term of Equation 2.8. The

natural frequency will be the square root of that spring term because mass has already been divided through the equation. The differences arose due to difficulties in accurately placing the centrifugal force onto the mass of the harvester as seen in Figure 3-24. The two lines indicate the direction of the centrifugal force. Whenever the force was not ideally placed on the mass, the harvester did not respond like was predicted. When great care was taken to make the force act linearly on the proof mass, the harvester responded as predicted. In order for the data to be completely accurate a better method of simulating the centrifugal force would be needed. However, the above data does prove the trend that the natural frequency is dropping with increasing centrifugal force.

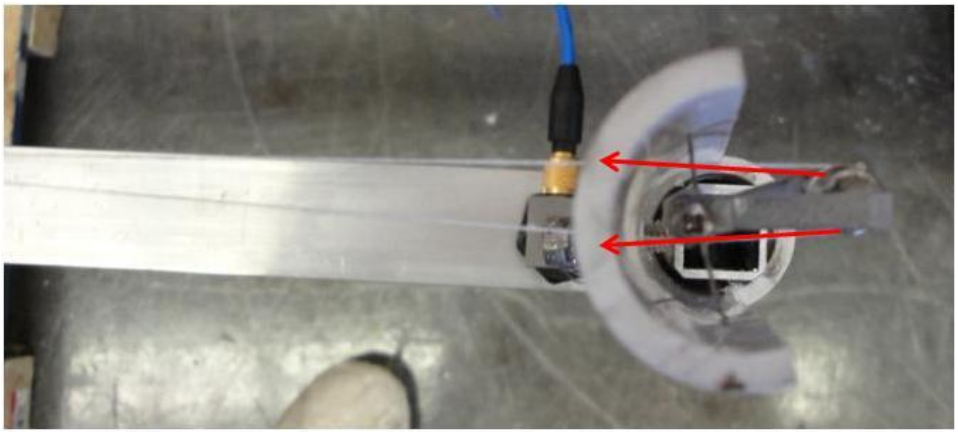

Figure **3-24**: Simulated Centrifugal Force on Proof Mass. Difficulties in pointing the CF linearly on the proof mass contributed to the differences in experimental natural frequency vs. predicted.

3.5.2 Mechanical and Electrical Damping

The initial displacement test and log decrement method described above can be used to find the mechanical damping of the device. Because there is no coil on the device during these

tests, all of the damping will be mechanical. Once the coil is placed into the device, there will be additional damping due to the magnet and coil interaction that will be part of the electrical damping of the device and is essential to producing voltage and ultimately power. Table 3-7 shows the results for mechanical damping values at different centrifugal forces.

Table **3-7**: Mechanical Damping Values.

CF (N)	ω_n	ζ
0	18.46	0.013
0.24	16.87	0.014
0.47	16.31	0.022
0.82	13.35	0.024
1.18	11.82	0.036

As expected, the mechanical damping ratio increases with increasing centrifugal force due to increased material losses in the spring and the clamped ends of the spring. These values represent pure mechanical loss in the system and ideally would be minimized in order to harvest more power.

To find the electrical damping of the system, a resistor was placed across the ends of the coil and the log decrement method was used to find total system damping. Then, knowing the mechanical damping of the system, the remaining damping had to be electrical. From Equation 1.15, the electrical damping will be a function of resistance. Section 2.2.3 showed that the most power is harvested when the electrical and mechanical dampings are matched. Figure 3-25 shows the results of the experiment for five different resistor values. The dot on the graph indicates the mechanical damping value of 0.0134. The 1000 ohm resistor provided the closest value to match electrical damping to mechanical. For simplicity and accuracy, this was only done for the harvester with no centrifugal force.

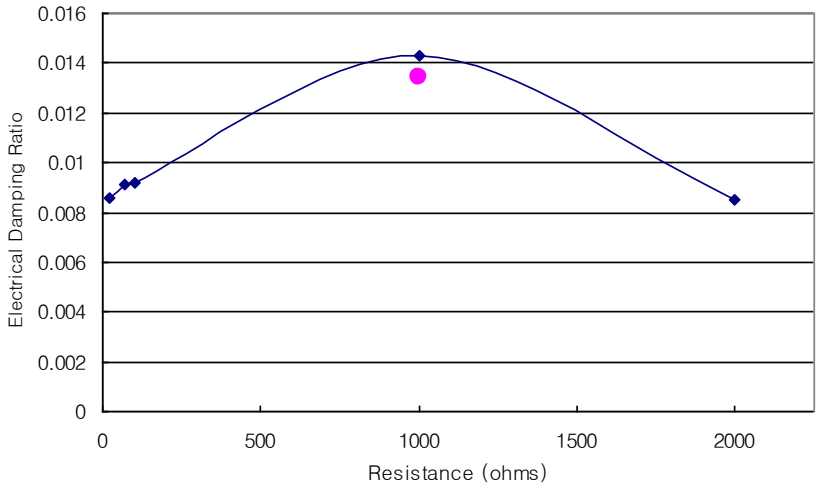

Figure **3-25**: Electrical Damping vs. Load Resistance. A resistor value of 1000 ohms closely matches electrical to mechanical damping which is ideal for energy harvesting. The dot on the graph indicates the mechanical damping value of 0.0134.

To find the value of resistor that matches the electrical damping to mechanical without having to experimentally determine it, Equation 1.15 can be utilized. Solving for R:

$$R = \frac{(NLB)^2}{2m\varsigma\omega_n} \tag{3.14}$$

Where ζ will be the mechanical damping value that is trying to be matched, ω_n is the natural frequency of the device, *m* is the mass of the system, and N, L, and B are properties of the coil and magnet. Table 3-8 gives the value of resistors that match electrical damping to mechanical at different values of centrifugal force. This is necessary because mechanical damping is a function of centrifugal force.

Table **3-8**: Load Resistance as a Function of Centrifugal Force.

CF	ζ_e	R (Ω)
0	0.013	1171
0.24	0.015	1060
0.47	0.022	700
0.82	0.024	646
1.18	0.036	433

The calculated value of R that would match electrical to mechanical damping was found to be 1170 ohms as compared to 1000 ohms experimentally.

3.5.3 Mass Motion Prediction and Validation

The mechanical damping and natural frequencies from Table 3-7 can now be used with the analytical model developed in Matlab and Simulink to predict the response of the device to different inputs. The laser vibrometer was once again used to measure the velocity of the device at the different flight conditions described in Section 2.1. The base motion system described in Section 3.2 was used to test the response at different flight conditions. This was first done for no centrifugal force and then for increasing amounts of centrifugal force as was previously done. The absolute velocity of the device was captured but it is the relative velocity of the proof mass with respect to the base motion that is necessary to generate power. This was found by subtracting the base velocity from the absolute velocity of the proof mass. Figure 3-26 is the absolute measured velocity of the device from 1^{o} cyclic to 10^{o} cyclic inputs versus the predicted velocity from the model. Very good agreement is seen showing that the model can indeed predict the response of the device.

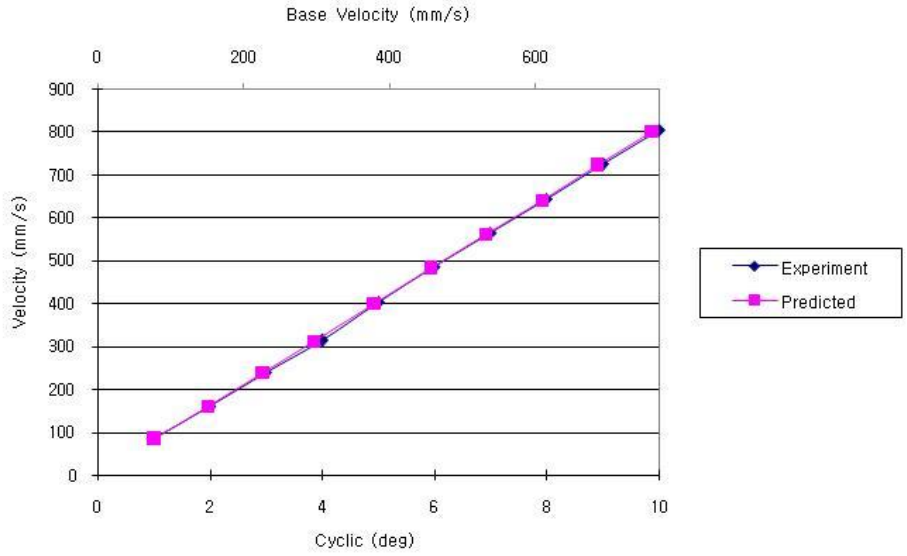

Figure **3-26**: Absolute Velocity of Proof Mass Experiment vs. Predicted with No Force. The experimental data closely agrees with what was predicted.

Subtracting the base velocity from the absolute velocity gives the relative velocity of the proof mass. This is seen in Figure 3-27. Once again, the predicted velocities match closely with what was found experimentally.

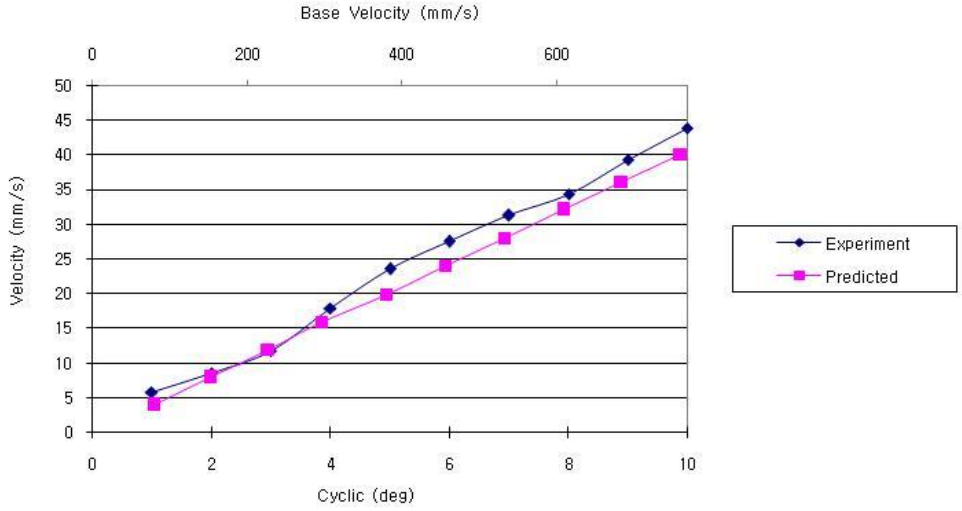

Figure **3-27**: Relative Velocity of Proof Mass Experiment vs. Predicted with No Force. Good agreement is seen between what was predicted and what was found experimentally.

Using these relative velocities, the voltage generated can be predicted. This will be done in the next section. The absolute and relative velocities were also found with centrifugal force being applied to the device. It was found earlier that the natural frequency dropped with applied force but differences arose due to difficulties in correctly applying the force. Therefore, we would expect that differences would arise in velocity prediction versus what was observed experimentally. Figure 3-27 shows the absolute velocity versus what was predicted for 0.47 N of centrifugal force. Experimentally the natural frequency with this force was found to be 16.3 Hz while the prediction was 15.12 Hz. There appears to be good agreement with this data.

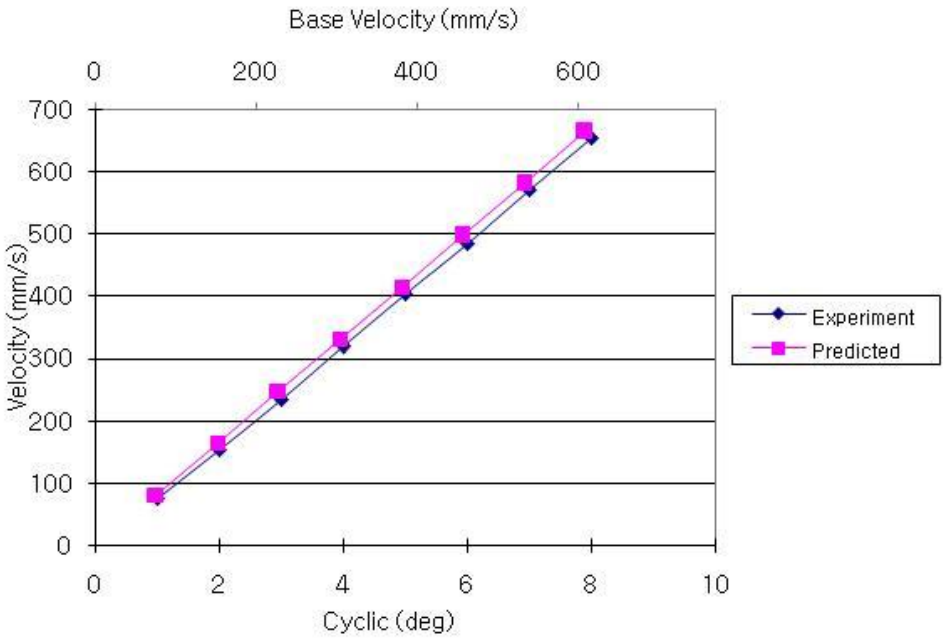

Figure **3-28**: Absolute Velocity of Proof Mass Experiment vs. Predicted for 0.47 N of Force. This data also shows good agreement between prediction and experiment

Figure 3-29 is the relative velocity of the proof mass with respect to the base motion. The differences in predicted versus experiment are more apparent here and are expected due to the differences in natural frequency.

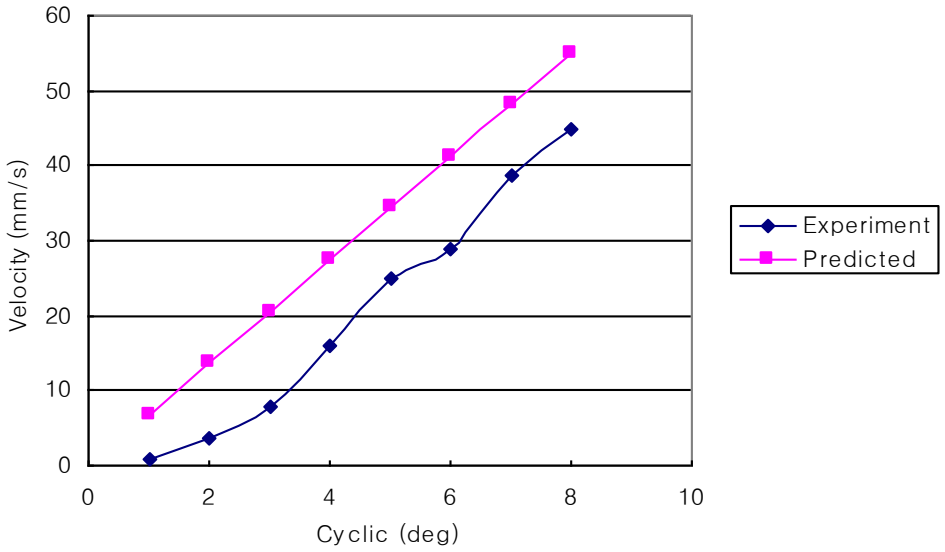

Figure **3-29**: Relative Velocity of Proof Mass Experiment vs. Predicted for 0.47 N of Force. Differences between the experiment and prediction are apparent.

Figures 3-26 through 3-29 show that the mass – spring harvester system motion is able to be predicted and experimentally verified. This means that, although differences do arise, any changes made to the device should be able to be predicted beforehand and also that the system can be optimized analytically. Absolute and relative velocities were found for other values of centrifugal force and as expected the differences became greater as the force increased. This was mainly due to the way that the force was applied to the proof mass as discussed in Section 3.5.1. Since the natural frequency of the device did not lower to 4.3 Hz as predicted, the rest of the testing will be done at the natural frequency of the device with no centrifugal force, 19 Hz.

3.5.4 Voltage Prediction and Validation

The relative velocities found above can now be used to predict what voltages should be produced when adding a coil to the system. A tightly wound coil was attached to the system and placed next to the magnet so that relative motion occurred between the two. A picture of the coil

is in Figure 3-30. The equation for generated voltage is $v(t) = NLB\dot{z}(t)$ where N is the number of turns in the coil, L is the length of an average turn, B is the magnetic flux density of the magnet, and $\dot{z}(t)$ is the relative velocity of the magnet with respect to the coil. First it is necessary to determine the number of turns in the coil. The length of the coil is 0.625 inches (15.88 mm). It has an inside diameter of 0.125 inches (3.175 mm) and an outside diameter of 0.25 inches (6.35 mm), making its thickness 0.25 inches. The coil uses AWG # 30 wire that has a diameter of 0.01 inches (0.254 mm). The coil will then have about 63 turns per layer and about 13 layers. This makes the total number of turns in the coil about 820. The average turn length, L, for the coil will be πd, were d is the average diameter of the coil. L is calculated to be 15 mm. The magnet provides a flux density of about 0.72 Teslas.

Figure **3-30**: Coil used in Experiment. The number of turns in the coil was determined to be 820.

Experiments were done to determine a correction factor for the equation that assumes that the magnet is in the center of the coil rather than next to it as is the case with the harvester. In this case the magnetic field lines that permeate from the magnet are not being "captured" by the entire coil. Rather, it is some percentage of the flux density that is producing the voltage. A picture illustrating this point can be seen in Figure 3-31. To verify this, an experiment was done

that vibrated a magnet next to the coil at known velocities. The results from the experiment along with some results from the harvester show that the actual voltage produced is 1/4 of what is predicted. Therefore, we can say that for this configuration, the harvester is only producing one quarter of the voltage that it could be. This is not very efficient but can still be useful.

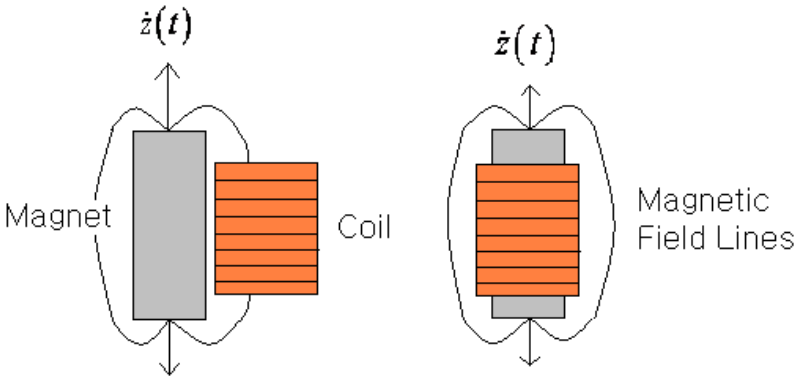

Figure **3-31**: Magnet Next to Coil vs. Magnet in a Coil. The magnet next to the coil was found experimentally to generate 1/4 of the voltage that a magnet in a coil will generate.

The natural frequency of the harvester without any centrifugal force is 19 Hz. When driven at this frequency with no force, Figure 3-32 is the voltage signal that is produced. According to the experiments described above, this only 1/4 of the voltage that can be produced at these vibration levels.

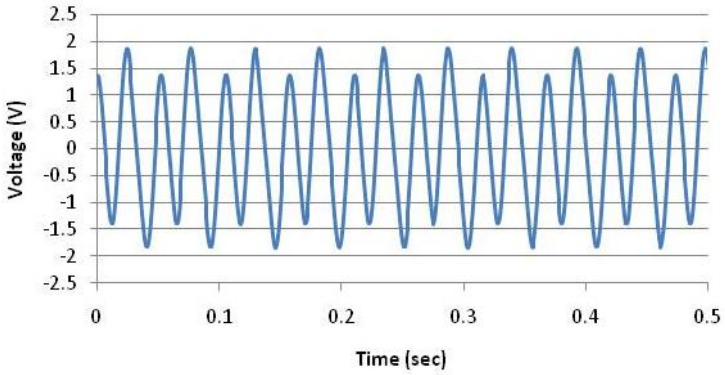

Figure **3-32**: Voltage Generated at 19 Hz. The voltage generated at 19 Hz with the device natural frequency at 19 Hz is almost two volts.

The peak AC voltage produced at 19 Hz is almost 2 volts. Going back to the predictions made about the voltage that would be produced, Figure 3-33 shows the voltage generated versus the predicted voltage with no centrifugal force driven at 4.3 Hz. The predictions here include the 1/4 correction factor that was found. The results from the experiment now match up with the prediction.

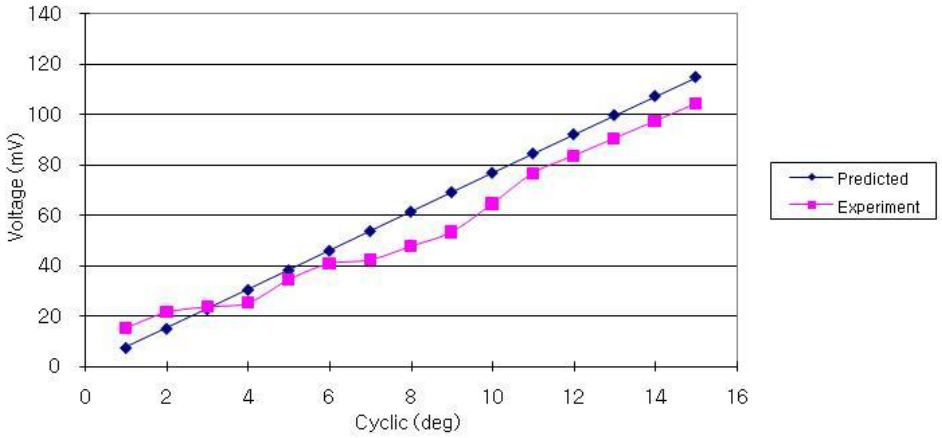

Figure **3-33**: Voltage Generated at 4.3 Hz with no Centrifugal Force. The empirically corrected prediction compares favorably with the experimental data.

Figure 3-34 below shows the voltage generated versus frequency ratio for the harvester with no force and the frequency ratio ranging from 0.89 to 1.1. As expected, the peak voltage generated occurs when the driving frequency matches the natural frequency of the device.

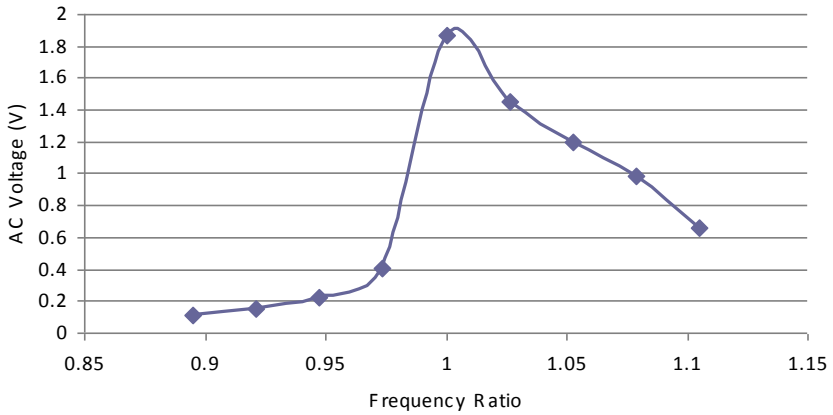

Figure **3-34**: Voltage vs. Frequency Ratio. The peak voltage occurs when the frequency ratio is equal to 1.

The results of the above tests show that the harvester is not generating as much voltage as it could be and there is room for improvement. As stated earlier, the voltage generated could be as much as four times of what is currently being produced. Figure 3-34 also illustrates the importance of matching the natural frequency of the harvester to the source vibrations. Being off by 0.5 Hz on the low end dropped the voltage from almost 2 volts to 0.4 volts, a loss of 80%. One improvement in the device would be to have the magnet in the center of the coil much like the linear harvester device described in Section 3.3.

3.6 Energy Harvesting Performance

The final performance parameter that needs to be tested is the power the harvester can deliver to a load. For the purposes of these tests, a simple resistor was placed in the circuit and the voltage across the resistor was measured. Power was then calculated with $P = V^2 / R$. The value of *R* needs to be chosen carefully. Section 2.2.3 discusses the affect that damping has on

the system. One of the conclusions was that mechanical damping and electrical damping should be matched to harvest the most power but it is better to have a system that is more electrically damped than a system that has a lot of mechanical damping. Mechanical damping values were found in Section 3.5.2. The electrical damping will be a function of the load resistance from Equation 1.15. Values for electrical damping as a function of load resistance were also found in Section 3.5.2. The conclusion was that a 1000 ohm resistor provided the value of electrical damping that most closely matched values for mechanical damping.

To determine if experimentally the resistor that should be used to maximize power was in fact a 1000 ohm resistor, a test was done with no centrifugal force at 19 Hz. The test included 8 different resistor values ranging from 2 ohms to 2000 ohms. The harvester was excited at the same acceleration levels in all 8 tests to determine the resistor value that gave the most power. The results are shown in Figure 3-35. The resistor that maximized power at 19 Hz with no centrifugal force was indeed the 1000 ohm resistor.

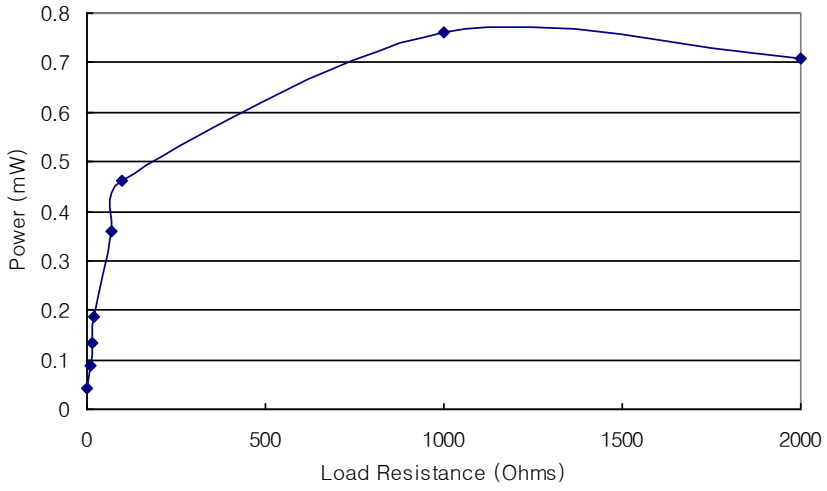

Figure **3-35**: Power vs. Load Resistance at 19 Hz Excitation. The power is maximized when electrical damping matches mechanical damping. The 1000 ohm resistor accomplishes that goal and provides the max power generated.

For the rest of the tests the 1000 ohm resistor will be used to test power output. The harvester was then tested for base acceleration values from 1^o – 10^o cyclic flight conditions at 19 Hz excitation to find the power the device can generate without any centrifugal force on it. Under these conditions the maximum power generated was 2 mW. The results from the test are in Figure 3-36.

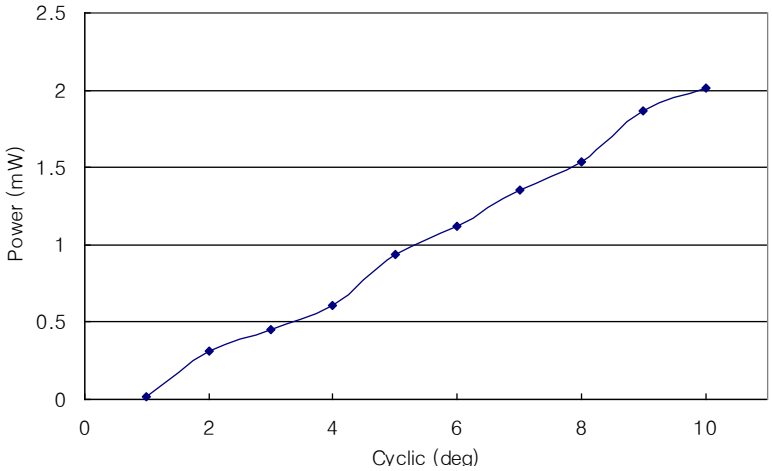

Figure **3-36**: Power vs Flight Condition at 19 Hz. The max power generated was 2 mW.

Values for power were only found up to 10^o cyclic but since the plot is fairly linear we can assume that almost 3 mW would be generated at 15^o cyclic, the most extreme flight condition. The previous values for power were found under ideal conditions at 19 Hz and little mechanical damping. Realistically, however, the device should operate at 4.3 Hz under centrifugal force which increases the mechanical damping but the lowers the frequency. Lowering the natural frequency will mean more response from the device but less power is available to harvest. Section 3.5.1 describes some of the difficulties associated with simulating the centrifugal force in lab conditions. Adding 1.17 N of centrifugal force should theoretically lower the natural frequency of the device to almost 4 Hz but experimentally it was only lowered to 11 Hz. Since the device is so far off resonance, we would not expect to generate much power.

Tests were done to determine exactly how much power could be generated, and the results were on the order of microwatts. These results are not presented here.

Power to a load of 1000 ohms was achieved under ideal conditions at a higher frequency than the frequency of the pitch link in flight. However, it does show that this configuration and dimensions are capable of producing power on the order of milliwatts. If a more consistent way to simulate centrifugal force could be achieved, then more power could be simulated at 4.3 Hz. The main reason why power closer to milliwatts was not achieved at 4.3 Hz excitation was the fact that the natural frequency of the device was almost three times that of the driving frequency. Figure 2-12 shows how power drops off with frequency ratio. The frequency ratio here was approximately 2.65, which is well off the best case scenario of a frequency ratio of 1 that was achieved to produce Figure 3-36.

Chapter 4

Conclusion

The final chapter draws conclusions on the performance of the energy harvester and makes recommendations on what aspects need to be improved and how the improvement can be accomplished. One application of the energy harvester is to power a strain sensor and use the data to predict retirement times. This application is detailed with some simulations using strain data taken from a lead-lag damper in Appendix B. Finally, recommendations for future work on the project are given.

4.1 Conclusions on Energy Harvester

The energy harvester developed and tested was based on pendulum configuration that utilized a combination of a mechanical torsion spring made from music wire and the centrifugal force from the rotation of the pitch link around the rotor as an effective spring constant. The proof mass of the harvester was an NdFeB cylindrical magnet with a mass of 3.02 grams. The coil used had 820 turns and was placed next to the vibrating magnet. The maximum power generated at 19 Hz was 2 mW and was delivered to a load of 1 kilo-ohm. Simulations showed that power ranging from a few milliwatts to 120 milliwatts were available to be harvested from the environment. The 3 mW harvested indicates a very low efficiency of around 3% conversion.

The final energy harvester did not produce enough power at 4.3 Hz due to reasons discussed in Section 3.6. However, there are many aspects of the design that can be improved. The most obvious is developing a way to increase the voltage produced. One way this can be done is through the use of a transformer with a turn ratio of at least 10:1. This would increase the

voltage ten times and allow it to be put through a bridge rectifier to produce DC voltage. One problem that was already found with transformers is the frequency. Most commercial transformers operate at 50 – 60 Hz or higher. No off-the-shelf transformers able to operate as low as 4.3 Hz were found.

Another way of increasing the voltage that was already discussed is to design the harvester in such a way that the magnet passes through the center of the coil instead of vibrating beside it. One way this could be achieved is with the linear reverse pendulum harvester discussed in Section 3.3 and shown in Figures 3-10 and 3-11. This device was built but not tested due to time limitations. A device like this will have more mechanical damping because it requires three hinges to operate but the voltage that can be generated may be as much as four times the amount currently being generated. Another way to increase voltage is to use a coil with more turns. The number of turns in the coil is directly proportional to the amount of voltage generated. A coil with twice the number of turns would be able to produce twice the voltage, theoretically. The limiting factor in sizing the coil, however, is the size of the hollow in the rod end. The coil that was used was 0.25 inches (6.35 mm) in diameter and was close to being the biggest allowable coil for the design space.

Voltage multiplier circuits were also looked at. Voltage multiplier circuits use diodes and capacitors to either double, triple, or quadruple the voltage from an AC source to produce DC voltage. A schematic of a voltage tripler circuit can be seen in Figure 4-1.

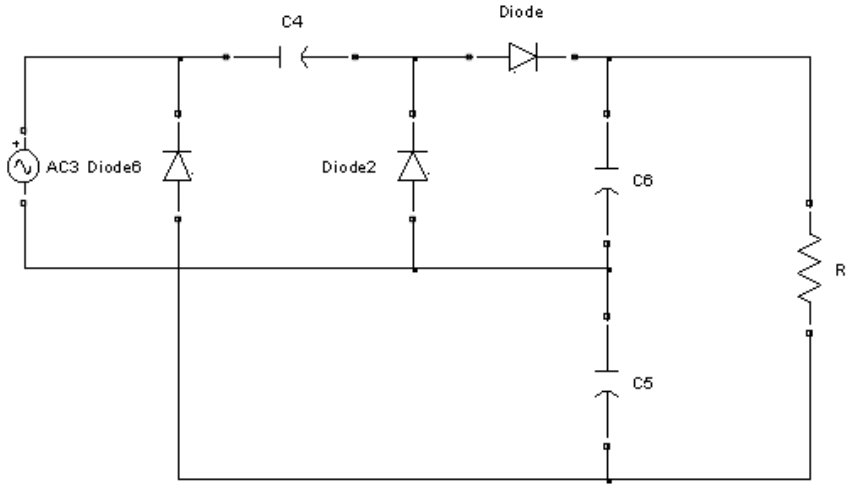

Figure **4-1**: Voltage Tripler Circuit. A circuit like this would be able to triple the voltage produced using diodes and capacitors.

The drawback of voltage multiplier circuits is the voltage loss across the diodes. Silicon diodes experience a voltage drop of 0.7 volts. Germanium diodes, which are more expensive and harder to find, only have a voltage drop of 0.2 volts. Considering the low voltage already produced by the harvester, large voltage drops are not ideal and should be minimized. Using a voltage drop of 0.2 volts, some simulations were run with voltage doubler, tripler, and quadrupler circuits. Figure 4-2 displays the results.

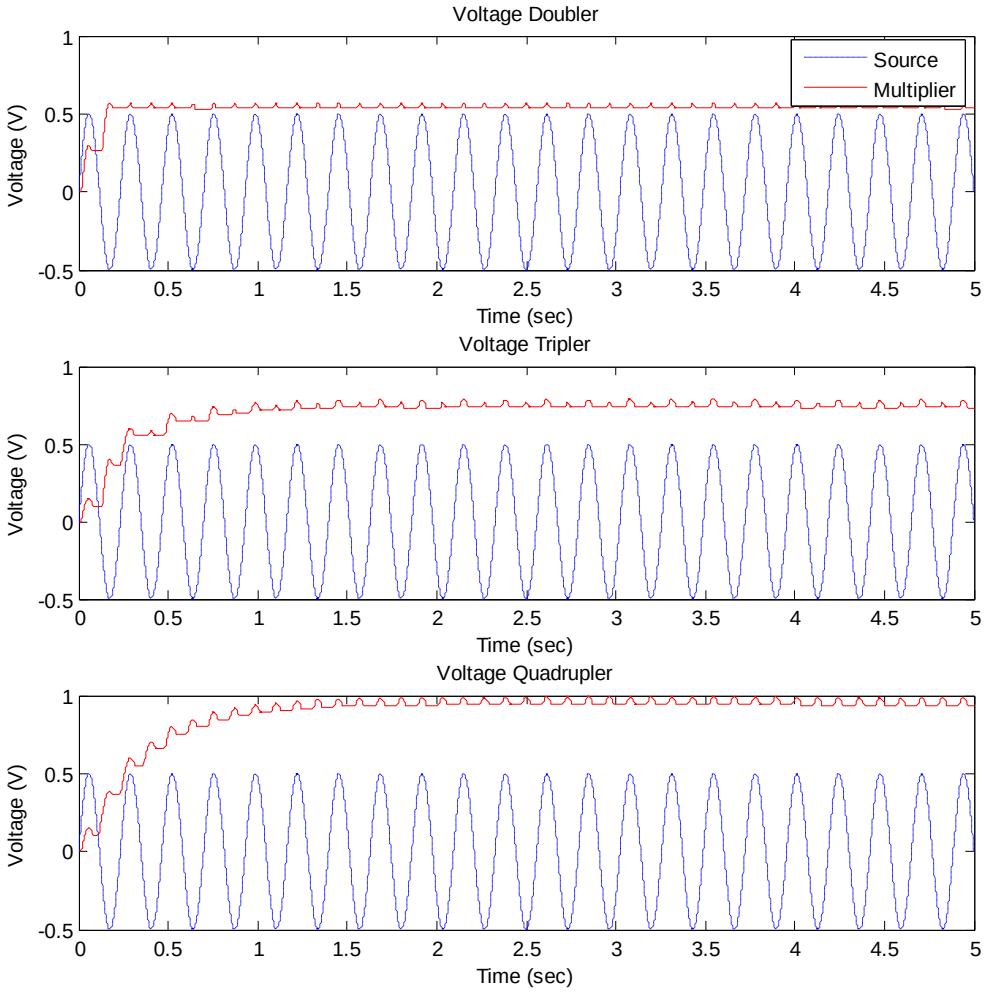

Figure **4-2**: Results of Voltage Multiplier Circuit Simulations. Voltage multiplier circuits can be used to double, triple, or quadruple the voltage, however voltage drops across diodes make them less effective in low voltage applications.

The voltage drops across the diodes are apparent. Another drawback to these circuits is the current loss through them. A voltage doubler can cut the current by roughly half. These are only a few ways that circuitry can be used to gain more power from the system. Other, more complicated, ways of producing more power can be done with clever circuits and research is currently being done on this. However, from a mechanical point of view, increasing mass,

quality factor, and coil size, or decreasing mechanical losses in the system are ways to generate more power.

4.2 Future Work

Electromagnetic energy harvesting is not a new concept; however, applications to rotorcraft and wireless sensors are still being explored. The next step in testing an electromagnetic device would be to put it on a test stand that mimics the motion of a pitch link but also spins, so that centrifugal force is created instead of simulated with a mass – pulley system. If the device works under these conditions then the final step would be to implement any circuit electronics and sensors. Ultimately, the final test would be a flight test, in which the harvester powers a sensor, obtains data, and wirelessly transmits the data to a remote station.

Improvements for the energy harvester have been discussed in Section 4.1 and include ways to boost the voltage through changes in the mechanical device and through added circuitry and other electronic elements. Some of these changes should be implemented in order to improve the power output of the device.

Only electromagnetic harvesting was thoroughly discussed here, however piezoelectric harvesting should also be looked at. Piezoelectric devices are known to produce more voltage then electromagnetic harvesters and have a greater power density, meaning more power can be harvested from a smaller volume device. A piezoelectric device could be designed to work as a resonant system similar to the electromagnetic device, or strains in rotorcraft components could be used to produce power. This is similar to the MicroStrain© pitch link energy harvesting system discussed in Section 1.3 [20].

References

[1] Lougee, Hoyt., 2002. "HUMS – Certification and Considerations for Current and Emerging Technology," *IEEE* 0-7803-7367-7

[2] Gill, John J., "Lessons Learned from Rotary and Fixed Wing HUMS Applications," BFGoodrich Aerospace, Bedford, Massachusetts

[3] Land, James E., 2001. "HUMS – The Benefits – Past, Present, and Future." *IEEE* 0-7803-6599-2

[4] Sodano, H., Inman, D., "A Review of Power Harvesting from Vibration using Piezoelectric Materials," *The Shock and Vibration Digest*, 36(3), pp. 197-205, 2004

[5] Roundy, S., Wright, P., Rabaey, J., *Energy Scavenging for Wireless Sensor Networks with Special Focus on Vibrations*, Kluwer Academic Publishers, 2004

[6] Mitcheson, P.D., Green, T.C., Yeatman, E.M. and Holmes, A.S. 2004. "Architectures for Vibration-Driven Micropower Generators," *Journal of Microelectromechanical Systems*, 13(3):429 – 440

[7] Gilbert, James M., Balouchi, Farooq. 2008. "Comparison of Energy Harvesting Systems for Wireless Sensor Networks," *International Journal of Automation and Computing*, 5(4):334-347

[8] Thomson, W.T., *Theory of Vibration with Applications*, 2nd Edition, Englewood Cliffs, NJ: Prentice Hall, 1981

[9] Priya, S., Inman, D. (eds.), *Energy Harvesting Technologies*, Springer Science+Business Media, LLC 2009

[10] Amirtharajah, Rajeevan, Chandrakasan, Anantha P., "Self Powered Signal Processing Using Vibration Based Power Generation." May 1998., *IEEE Journal of Solid State Circuits*., vol. 33, No. 5.

[11] El-Hami, M., Glynne-Jones, P., White, N.M., Hill, M., Beeby, S., James, E., Brown, A.D., Ross, J.N., "Design and Fabrication of a New Vibration-based Electromechanical Power Generator," *Sensors and Actuators*, A 92, pp. 335-342, 2001

[12] Glynne- Jones, P., Tudor, M.J., Beeby, S.P., White, N.M., "An Electromagnetic, Vibration-Powered Generator for Intelligent Sensor Systems," *Sensors and Actuators*, A 110, pp. 344-349, 2004

[13] Beeby, S., Torah, R., Tudor, M., Glynne-Jones, P., O'Donnell, T., Saha, C., Roy, S., "A Micro Electromagnetic Generator for Vibration Energy Harvesting," *Journal of Micromechanics and Microengineering*, 17: 1257-1265, 2007

[14] Beeby, S., Tudor, M., White, N., "Energy Harvesting Vibration Sources for Microsystem Applications," *Measurement Science and Technology,* 17: R175-R195, 2006

[15] Saha, C., O'Donnell, T., Loder, H., Beeby, S., and Tudor, J., "Optimization of an Electromagnetic Energy Harvesting Device," *IEEE Transactions on Magnetics,* vol. 42, no. 10, October 2006

[16] Beeby, S., Tudor, M., Torah, R., Roberts, S., O'Donnell, T., Roy, S., "Experimental Comparison of Macro and Micro Scale Electromagnetic Vibration Powered Generators," *Microsyst Technol,* 13: 1647-1653, 2007

[17] Yuen, Steve C.L., Lee, Johnny M.H., Li, Wen J., Leung, Philip, H.W., "An AA-Sized Vibration-Based Microgenerator for Wireless Sensors." *Pervasive Computing,* January – March 2007.

[18] Hadas, Z., Kluge, M., Singule, V., Ondrusek, C., "Electromagnetic Vibration Power Generator," *IEEE International Symposium on Diagnostics for Electric Machines, Power Electronics and Drives, SDEMPED,* pp. 451-455, 2007.

[19] von Buren, T., Mitcheson, P., Green, T., Yeatman, E., Holmes, A., Troster, G., "Optimization of Inertial Micropower Generators for Human Walking Motion," *IEEE Sensors Journal,* vol. 6, no. 1, February 2006

[20] Arms, S., Townsend, C., Churchill, D., Augustin, M., Yeary, D., Darden, P., Phan, N., "Tracking Pitch Link Dynamic Loads with Energy Harvesting Wireless Sensors," Presented at the American Helicopter Society 63rd Annual Forum, Virginia Beach, VA, May 1-3, 2007

[21] Arms, S., Townsend, C., Churchill, D., Moon, S., Phan, N., "Energy Harvesting Wireless Sensors for Helicopter Damage Tracking," Presented at the American Helicopter Society 62nd Annual Forum, Phoenix, AZ, May 9-11, 2006

[22] Churchill, D., Hamel, M., Townsend, C., Arms, S., "Strain Energy Harvesting for Wireless Sensor Networks," *Smart Structures and Materials,* Proceedings of SPIE vol. 5055, 2003

[23] S.W. Arms et al., Energy Harvesting, Wireless Structural Health Monitoring System, *US Patent Appl. Publ. US 2008/0036617A1, filed Sept 2006*

[24] Fuhrer, Zach, "Rod End Drawing." Email to author. 16 June 2009

[25] Corl, Jonas. "A Comparison of Helicopter Active Rotor Gust Rejection and Vibration Alleviation Methods." Master's Thesis, The Pennsylvania State University, 2009

[26] Amzallag, C., Gerey, J.P., Robert, J.L., and Bahuard, J., "Standardization of the Rainflow Counting Method for Fatigue Analysis," *Fatigue,* 1994, Vol, 16, June, pp. 287-293

[27] Clothiaux, John D., Dowling, Norman E., "Verification of Rain-Flow Reconstructions of a Variable Amplitude Load History," Oct. 1992, NASA Contractor Report 189670, Langley Research Center, Hampton, Virginia

[28] Thang, Bui Quoc, Dubec, Julien, Bazergui, Andre, and Biron, Andre, "Cumulative Fatigue Damage Under Strain Controlled Conditions" *Journal of Materials*, JMLSA, Vol 6, No. 3, Sept. 1971, pp 718-737

[29] Dubuc, Julien, Thang, Bui Quoc, Bazergui, Andre, and Biron, Andre, "Unified Theory of Cumulative Damage in Metal Fatigue," *WRC Bulletin*, Issue 162, 1971, pp. 1-20

[30] Yang, L., Fatemi, A., "Cumulative Fatigue Damage Assessment and Life Predictions of as-forged vs. QT V-based MA Steels using Two Step Loading Experiments," *Journal of Materials: Design and Applications*, Part L, Vol. 217, 2003, pp. 145-155

Appendix A

Test Procedure

The steps to using the base motion system described in Section 3.2 are given here for the benefit of future researchers. The system was shown in Figure 3-2 and includes an amplification lever attached to an electromagnetic shaker driven by a signal generator and amplifier. The system is monitored by a tri-axial accelerometer and an oscilloscope. The following steps can be used to set the system to mimic whatever flight condition is needed.

1. Turn the power supply on located in the rear of the power panel.
2. Turn on the individual components: Oscilloscope, Signal Generator, and Amplifier. Make sure that the cooling fan is on as well. Also, make sure that the amplifier control knob is turned all the way down (Counterclockwise).
3. Set the signal generator frequency to 4.3 Hz and the amplitude to 1 volt.
4. Slowly turn the amplifier control knob 1/4 turn clockwise. The electromagnetic shaker should now begin to move the amplification lever.
5. On the oscilloscope, press auto focus and adjust the incoming signal from the accelerometer so that entire signal can be seen and monitored.
6. The output of the accelerometer to the oscilloscope should be coming out of the power supply BNC connection marked 10x. This means that the signal to the oscilloscope is 10 times the actual signal. The sensitivity of the accelerometer is 10.34 mV/(m/s^2). Use Table A-1 to determine what the signal on the oscilloscope should look like to correspond to the pitch link acceleration that you are trying to simulate.

7. Adjust the amplifier control knob or the amplitude on the signal generator to match the acceleration of the end of the amplification lever to the value desired as monitored on the oscilloscope.
8. To shut down the system, turn the control knob on the amplifier all the way counterclockwise. Turn off the amplifier, signal generator, and oscilloscope. Turn off the power supply in the rear of the power panel.

Table **A-1**: Oscilloscope Signal Outputs for Simulating Pitch Link Accelerations.

Flight Condition Cyclic (deg)	Pitch Link Acceleration (m/s^2)	Oscilloscope Reading (V)
1	2.04	0.423
2	4.09	0.845
3	6.13	1.27
4	8.25	1.71
5	10.29	2.13
6	12.34	2.55
7	14.38	2.97
8	16.43	3.40
9	18.54	3.83
10	20.59	4.26
11	22.63	4.68
12	24.68	5.10
13	26.72	5.53
14	28.77	5.95
15	30.81	6.37

Appendix B

Application of Energy Harvester

The final application of the energy harvester would be to power a sensor, most likely a strain gauge that could monitor the loads that the part has seen. The sensor would have to continuously take data and then process it into something useful to be wirelessly transmitted for further processing and interpretation. This way, the actual loads the part experiences would be used to determine component retirement times. The first step in processing the data is to use a method called rainflow counting to reduce seemingly random data into something that is useful and can be interpreted. Once the data has been rainflow counted, the fatigue damage can then be calculated. A demonstration done at LORD Corporation by KCF Technologies obtained 53 sets of 30 second strain data off of a lead-lag damper that was put into a quality test stand and put through different flight conditions that ranged from mild to severe.

A.1 Rainflow Counting

Rainflow counting takes a random set of time history data, like stress or strain data, and places it into histograms that express the amplitude and frequency of the cycles. It is the most popular form of cycle counting today and the first necessary step in computing the fatigue damage incurred by a part [26]. Before the data can be rainflow counted, the maxima and minima must first be extracted. The strain data taken from the lead-lag damper and the extracted maxima and minima are shown in Figure A-1.

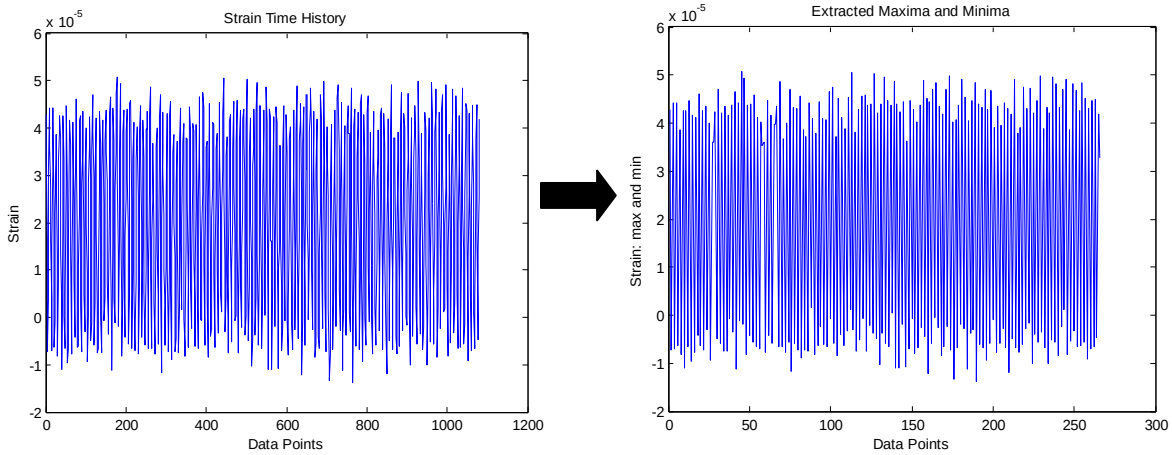

Figure **A-1**: Strain Data from Lead-Lag Damper and the Extracted Maxima and Minima. The second graph contains the maximum and minimum extracted data points from the strain time history. This data can now be rainflow counted and put into a histogram that is useful for computing fatigue damage.

The extracted maxima and minima are then put through the rainflow cycle counting algorithm that puts the data into histograms of number of cycles of strain at their amplitudes.

Figure A-2 is a 3-D histogram that plots number of cycles versus amplitude versus mean value.

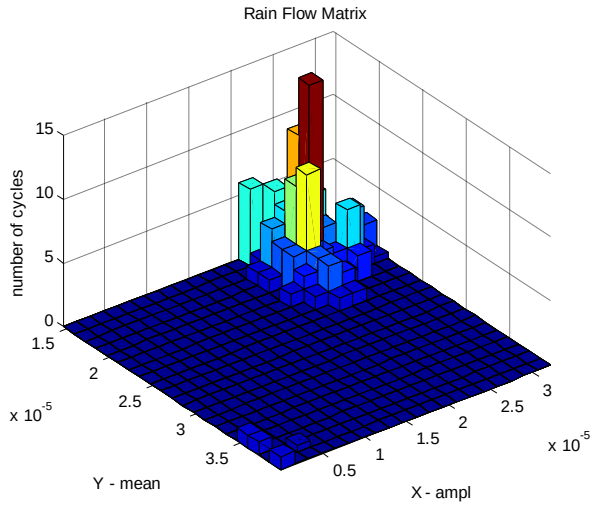

Figure **A-2**: Three Dimensional Histogram of Rainflow Counted Strain Data. The three dimensional histogram contains data broken into amplitude of the cycle, mean value of the cycle, and the number of cycles in each bin.

The second histogram shown below in Figure A-3 is a 2-D histogram that shows number of cycles and the frequency of the amplitudes of strain.

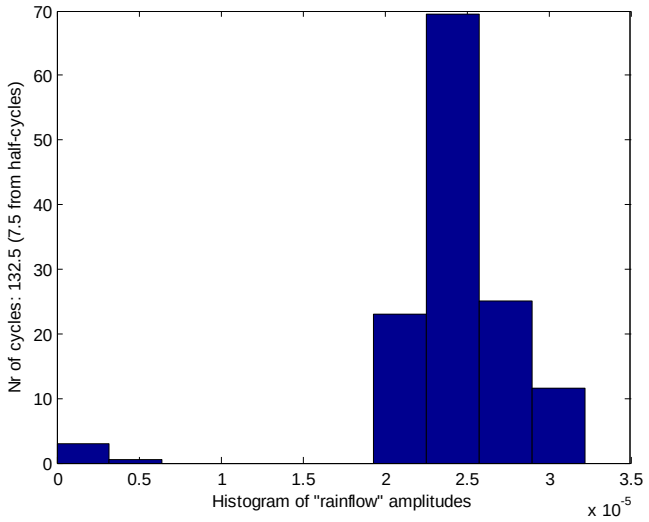

Figure A-**3**: Two Dimensional Histogram of Rainflow Counted Strain Data. This histogram contains information on the amplitude of applied strains and the number of times that amplitude has occurred. This data will be used to compute the fatigue damage accumulation of the part and update the retirement time of the component.

The second histogram is more useful for calculating fatigue damage and remaining life and will be used in the next section to do so.

A.2 Fatigue Damage Accumulation

In order to more accurately assess the damage incurred by each cycle, a hybrid fatigue theory proposed by Bui-Quoc *et al* was used. This theory was developed from the hybridization of earlier models and gives an improved life prediction from that of Miner's rule [28]. It is based on the fact that damaged materials exhibit a reduction in endurance limit and ultimate tensile strength. There are two versions, a stress controlled and a strain controlled, with an easy conversion between the two. The strain version is given by the following equation:

$$D_i = \frac{\ln(\varepsilon_e / \varepsilon_{eo})}{\ln(\varepsilon_{ec} / \varepsilon_{eo})} = \frac{r}{r + (1-r)\left[\dfrac{\lambda - (\lambda / \lambda_f)^m}{\lambda - 1}\right]} \quad . \qquad \text{(A.1)}$$

where,

$\lambda = 1 + \ln(\varepsilon / \varepsilon_{eo})$

$\lambda_f = 1 + \ln(\varepsilon_f / \varepsilon_{eo})$

ε : applied maximum cyclic strain

ε_f : fracture ductility or true strain at fracture

ε_e : instantaneous strain endurance limit

ε_{eo} : initial strain endurance limit

ε_{ec} : critical strain endurance limit

m : material constant

$r = N / N_f$: cycle ratio

N : Applied Cycles

N_f : Cycles to failure

This equation gives a nonlinear, load level dependant damage assessment that is able to account for reduction in the strain endurance limit which results from prior strain cycling. In order to use this equation as a damage assessment it will be necessary to establish the endurance limit of the material and some material constants. This can be either be done experimentally or taken from published values already available. The parameter λ is used to transform the conventional log-log ε-N strain fatigue diagram into a semi-log λ-N diagram. From experimental results the constant *m* has been determined to be 8. In order to assess the cycle ratio we are using a counting technique known as the rainflow method. The purpose of the rainflow method is to

reduce the time history of strain data into a histogram of cycles experienced by the component. This makes it possible to calculate the damage done by each cycle using the equation from above. The total damage can then be accumulated using the following equation:

$$D = \sum_{i=1}^{k-1} D_i \, . \qquad \text{(A.2)}$$

This gives the damage accumulated up to the *k-1* strain levels. To assess the useful remaining life of the component, the cycle ratio (r_k) for the k^{th} strain level is evaluated from equation 4.2. The remaining useful life for the last strain level is then given by:

$$n_k / N_k = 1 - r_k \, . \qquad \text{(A.3)}$$

This can be used to determine if the component needs to be replaced or if it can satisfactorily fulfill additional flight responsibilities. A modified version of the hybrid theory which accounts for load interaction effects also exists. This modification adds an exponent to the cycle ratio called the load interaction parameter *v* and can be used for multi-step fatigue.

Once the data was stored it was run through the fatigue algorithm described above. After each set of thirty (30) second data was rainflow counted, the algorithm computed the damage done by each "bin" in the histogram. It then determined the overall damage done by the strain set simply by adding all the damages. This is shown in Figure A-4.

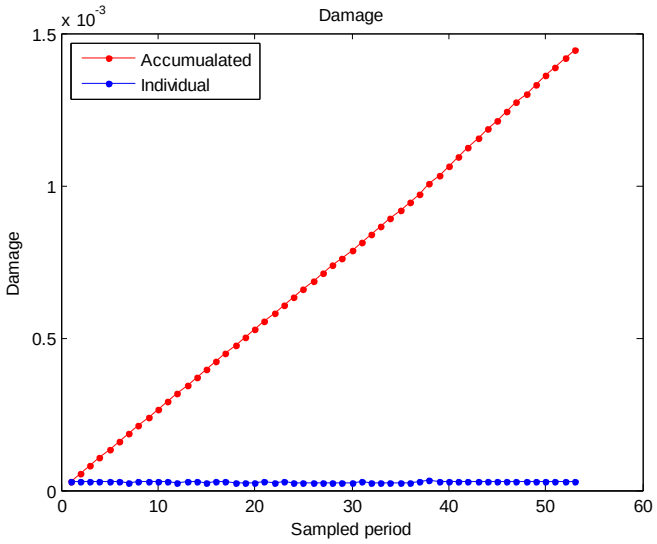

Figure **A-4**: Individual and Accumulated Damage from Hybrid Theory Fatigue Algorithm. This is the fatigue damage the part has accumulated according to the Hybrid fatigue theory.

After each set of data, a remaining life was calculated that showed how much longer the part would last given the previous loading history. This is given as a percentage of life remaining and is shown in Figure A-5.

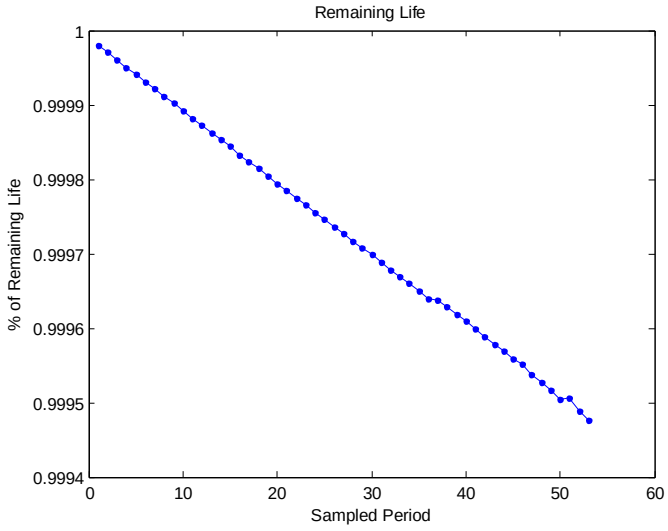

Figure **A-5**: Remaining Life from Hybrid Theory Fatigue Algorithm. This is the remaining life the part has left after each set of strain data is rainflow counted and put through the fatigue algorithm.

The hybrid fatigue theory proposed by Bui Quoc *et al* is one of many fatigue damage accumulation methods that has been proposed over many years. The original is Miner's Rule and although it is a linear rule that is not very accurate, it still has widespread acceptance due to no other theory gaining popularity. Along with data taken experimentally in a lab, data taken from a wireless, autonomous sensor placed on the aircraft could be used to make fatigue damage accumulation theories such as Miners Rule or the Hybrid Theory more accurate.